Modeling, Analysis and Design of Renewable Energy Nanogrid Systems

Igor Cvetkovic

Thesis submitted to the Faculty of the Virginia Polytechnic Institute and State University in partial fulfillment of the requirements for the degree of

MASTER OF SCIENCE

In

Electrical Engineering

Dushan Boroyevich, Chair

Fred C. Lee

Fei (Fred) Wang

July 22nd, 2010
Blacksburg, Virginia

Keywords: electric power distribution systems, power converter modeling, terminal behavioral identification, system integration, nanogrid, microgrid.

Modeling, Analysis and Design of Renewable Energy Nanogrid Systems

Igor Cvetkovic

ABSTRACT

The thesis addresses electronic power distribution systems for the residential applications. Presented are both, renewable energy ac-nanogrid system along with the vehicle-to-grid technology implementation, and envisioned structure and operation of dc-nanogrid addressing all system components chosen as an inherent part of the future electrical architecture. The large-scale model is built and tested in the laboratory environment covering a few operational modes of the ac-nanogrid, while later in the thesis is shown how dc bus signaling technique could be contemplated for the energy management of the renewable energy sources and their maximal utilization.

Thesis however puts more focus on the dc-nanogrid system to explore its benefits and advantages for the electrical systems of the future homes that can easily impact not only residential, but also microgrid, grid and intergrid levels. Thus, presented is low frequency terminal behavioral modeling of the system components in dc-nanogrid motivated by the fact that system engineers working on the system-level design rarely have access to all the information required to model converters and system components, other than specification and data given in the datasheets. Using terminal behavioral modeling, converters are measured on-line and their low frequency dynamics is identified by the means of the four transfer functions characteristically used in two port network models. This approach could significantly improve system-level design and simulations.

In addition to previously mentioned, thesis addresses terminal behavioral modeling of dc-dc converters with non-linear static behavior showing hybrid behavioral models based on the Hammerstein approach.

ACKNOWLEDGEMENTS

I am very happy to have a great opportunity to express my gratitude to all people that helped, influenced and supported my work directly or indirectly.

I owe my deepest gratitude to my advisor, Dr. Dushan Boroyevich for all of his guidance, support and endless encouragement during my graduate studies at the Center for Power Electronics Systems (CPES) - Virginia Tech. Although highly passionate about power electronics, his very broad knowledge and enthusiasm has greatly influenced my perception of engineering in general. In the same time, his intelligence, sense of humor and positive attitude, changed my perception of life.

It was an honor for me to have Dr. Fred C. Lee and Dr. Fei (Fred) Wang as my committee members. I am very thankful to them for all technical discussions, opinions and suggestions as well as for the shared knowledge in the different areas of power electronics.

I would also like to thank Dr. Paolo Mattavelli for all contribution, support and help with this thesis as well as with my research in general.

Thanks to Dr. Rolando Burgos, Dr. Khai Ngo, Dr. G.Q. Lu, Dr. Ming Xu and Dr. Shuo Wang for the technical discussions and valuable suggestions especially in the early stage of my thesis.

Although not directly involved in my research, I am thankful to the wonderful CPES' people whose unselfish help greatly influenced my work and research - thanks to Marianne Hawthorne, Teresa Shaw, Linda Long, Linda Gallagher, Trish Rose, Doug Sterk, David Gilham, Dr. Pengju Kong, Shu Ji, Alex Goodman, Phil McElmurray, and to the former CPES' employees Bob Martin, Jamie Evans and Dan Huff.

I am indebted to my colleagues and friends for the big contribution in this thesis and my research in general. Many thanks to Dr. Tim Thacker, Dr. Glenn Skutt, Dr. Jack Lesko, Dr. Gerald Francis, Dr. Luis Arnedo, Dong Dong, Li Jiang, Dr. Yuling Li, Dr. Hui Zhang, Dr. Yue Chang, Dr. Carson Baisden, Vladimir Podosinov, Marko Jaksic, Milisav Danilovic, Dr. Fang Luo, Sara Ahmed, Bo Wen, Zhiyi Shen, Zheng Chen, Wei Zhang, Ruxi Wang, David Reusch, Dr. Di Zhang, Dr.Rixin Lai, Dong Jiang, Jeremy Webb, Ying Lu, Kuang-Yao Cheng, Feng Yu, Hemant Bishnoi, Xiao Cao, Weiyi Feng, Krishnakumar Gopalakrishnan, Daocheng Huang, Qiang Li, Qian Li, Mingkai Mu, Chanwit Prasantanakorn, Jayashree Seshadri, Yipeng Su, Shuilin Tian, Zijian Wang, Haoran Wu, Yingyi Yan, Yiying Yao and Xuning Zhang.

I would like to show my deep gratitude to Dr. Slobodan Vukosavic for the unselfish support, encouragement and given theoretical and practical knowledge. Thanks to him I got my first job in industry, a lot of practical experience and an opportunity to continue my education in the USA.

I am also very indebted and thankful to Dr. Victor R. Stefanovic for encouragement, advices and an immense help toward my graduate degree. Also, thanks to Mr. Bosko Buha for all the support and help during my professional career and later, during my graduate studies.

This thesis would not have been possible without an enormous support, love and understanding I am constantly receiving from my beloved wife and a son. Their constant encouragement and care are inspiring me to overcome the most difficult moments on the road of my professional development. To my parents, sister and grandparents I am deeply thankful for the endless love, support and care.

As very fortunate to have a big family, family-in-law and a lot of friends, I would like to thank to all of them for encouragement and help I received during my graduate studies at Virginia Tech.

TABLE OF CONTENTS

LIST OF FIGURES

LIST OF TABLES

Chapter 1. INTRODUCTION

The constantly growing need for more electric power as a result of a global technological development on one side, but vulnerable environment on the other, definitely influences the way how the electricity will be produced, transmitted, distributed and utilized in the future. This will inevitably put the existing electric power system under a serious revision in order to increase efficiency, reliability and response to the end user, but in the same time offer more controllability, higher safety and user-friendly access. Power electronics, along with an advanced energy management provides an excellent solution to this problem, and it may not be unusual if "tomorrow" our complete power system operates in the same fashion our laptop power supply operates today.

1.1. Motivation and Objectives

1.1.1. Electrical System Architecture

The top of the Figure 1.1 shows the simplified structure of the power system in the way it is presently organized. The generation is conventionally accomplished by the base-load power plants (nuclear and coal-fired) and peaking power plants (gas turbines and hydroelectric plants), while the transmission already includes high-voltage dc (HVDC) systems as the good-established power electronics-interfaced solution [1-3].

The so-called microgrid illustrated in the Figure 1.1 is widely known and accepted concept that comprises energy storage and a larger number of generating units in order to get the most from the naturally available renewable energy sources while minimizing infrastructural changes of the existing power grid [4,5]. As a smaller part of the microgrid, the residential level system (up to 25kW) can be recognized and defined as ac-nanogrid. Ac-nanogrid is thus an electrical system backbone of the power electronics–based contemporary homes as the one illustrated in the Figure 1.2, envisioned to be energy sustainable and powered by different types of renewable energy sources, together with utility grid. The sources would mainly include photovoltaic solar cells (PV), wind generators, micro-turbines, fuel cells, local energy storage and Plug-in Hybrid Electric Vehicles (PHEV) that are highly expected to become an inherent part of the future home [6,7]. Figure 1.2 provides a high-level schematic illustrating the interconnections and functions of a variety of home electric energy components that together comprise a sustainable home with the ac-nanogrid system. Various functional coupling mechanisms among the various devices are

evident in this figure. Combined with the smart power net-metering, monitoring and control, ac-nanogrid offers high controllability and smart optimization of the system sources and loads to achieve zero-net annual energy requirement and cost.

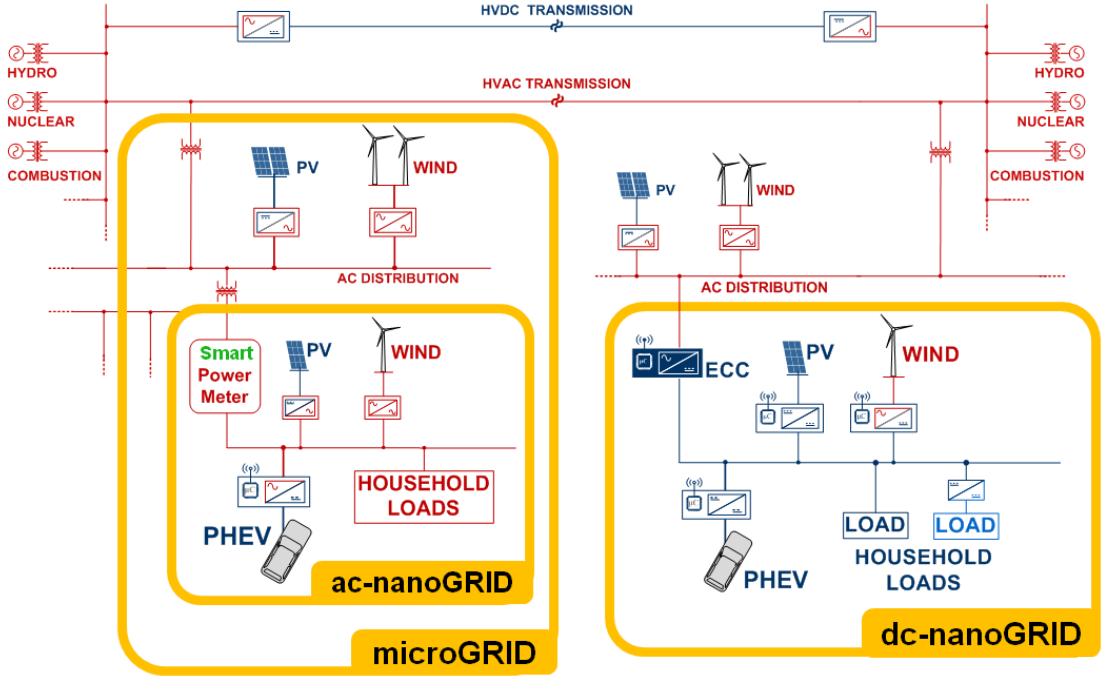

Figure 1.1: An illustration of the electric power system with defined subsystems

It is envisioned that through appropriate design of these devices and by operating them in a coordinated fashion, net residential fuel-based energy use can be reduced dramatically, while simultaneously increasing the perceived comfort levels in terms of lighting, temperature, water and air quality.

Major features that distinguish the operation of the contemporary, in comparison to conventional, home energy system, include the following:

- Renewable energy generation (e.g., solar systems, wind)
- Local fuel-based energy generation (e.g., micro-Combined Heat and Power (CHP) systems)
- EV/Plug-in hybrid generation/charging/storage
- Ability to continue operating in islanded mode and thus ride-through most of the grid outages
- Responsive illumination control (e.g., LEDs, CFLs)
- Process-optimized appliance operation control (air, water, HVAC)
- Sensor, monitoring, and control network (wired or wireless) for energy sources, appliance, lighting, and process energy management; wired or wireless.

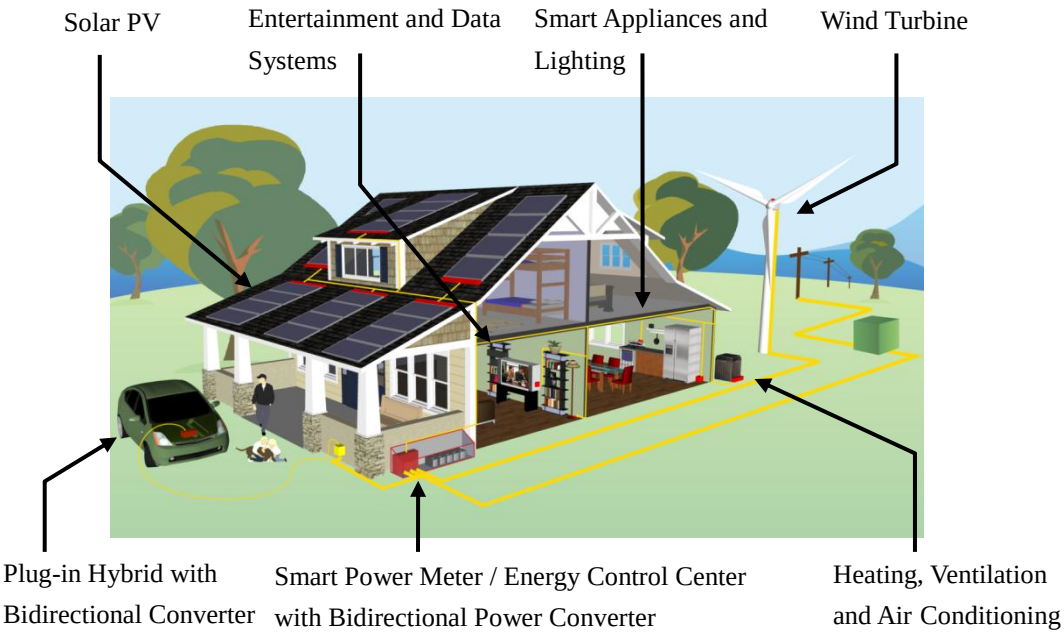

Figure 1.2: Conceptual sketch of power electronics-based future house (Illustration by CPES, 2010)

However, in conventional electrical power systems, the dynamics of generation, distribution, and consumption are fully coupled, and the system stability is in the ac systems achieved with the constant frequency electromechanical sources (synchronous generators), while in dc systems with constant voltage electrochemical sources (batteries) [8]. Rerouting of energy is only ensured through high redundancy, over-design, and electromechanically controlled devices considered to be dynamically slow and unreliable [9]. By looking at the Figure 1.1, it can be seen that some of the components in the ac-nanogrid system such as PV, Wind and PHEV are actually interfaced to the grid through the power converters because of their different dynamic characteristics, and thus dynamically completely decoupled from it [10-14].

The growing need for a highly reliable supply of electrical energy for critical applications, such as hospitals, data centers, semiconductor, auto and industry in general, have extended the use of power electronics converters in their electrical systems. These systems include multiple energy sources and redundant energy storage for back-ups, in addition to the numerous active loads [15,16]. Similarly, there has been an increased utilization of power electronics converters in hybrid electric vehicles, ships and airplanes to replace thermo-mechanical, mechanical, hydraulic, and pneumatic systems [17-20]. In these applications, majority of energy sources are interfaced to the power system through power electronics converters because of their very different dynamic characteristics.

Based on the examples above, it could be envisioned that in the future electronic power distribution systems, the dynamics of electric energy generation, distribution,

and consumption will be fully dynamically decoupled through the power electronics converters. To reach these goals, future research in power electronics area has to go beyond the converters, and address their integration, design, optimization, energy management, power quality on one side, and system-level modeling, analysis and stability on the other.

Ac-nanogrid for example, can be actually interfaced to the utility grid (or more precisely - microgrid) through the bidirectional ac/ac converter placed at the point where smart power meter is placed on the Figure 1.1, and could, in addition to the power conversion functions, feature Energy Control Center (ECC) operation such as real time pricing, source and load management, smart metering and many others.

Although interfacing ac-nanogrid to the microgrid through bidirectional power converter would assure immunity to the most of the grid disturbances and voltage and frequency deviations, such a system would, on the other side, add more complexity to the electrical architecture. As a possible solution to this problem Figure 1.1 shows dc-nanogrid system interfaced to the grid through the bidirectional ac/dc power converter which, contrary to the ac case, actually reduces complexity and installation costs while at the same time increases efficiency and controllability, as it will be shown later in this thesis.

1.1.2. DC Systems

Historically, direct current (dc) systems were in the practical use before the alternating current (ac) systems [21]. Not only the very first cars were powered by the batteries, but in early 1880s, the American inventor Thomas Edison designed and built the first low-voltage dc distribution system around Pearl Street, downtown Manhattan, New York, that served the area of about one square mile. The system however had a drawback in high losses related to the low voltage at the generation point and long transmission lines (feeders), and it could not compete with advantages alternating current systems offered in the sense of power losses, transmission and voltage level transformation. Nikola Tesla's poly-phase ac power systems made a breakthrough in the use of ac power which definitely ended the "war of currents" between him and Westinghouse on one and Edison on the other side [22]. However, dc system was never completely expelled from the use, and, in fact, was for years the only way to power the electric motors where speed had to be regulated, such as in industry and traction. Also, telephone system had been always powered by dc.

An emergence and technological development of power electronics definitely brought back dc system on the power scene. Today, dc power systems are highly developed and present in the special applications as telecommunications systems [23], electric vehicles [24], zonal power distribution system for future ships [25,26],

traction [27], and power-electronics-interfaced high-voltage dc (HVDC) transmission that gained significant interest in the recent years [28-30].

Dc voltage levels are very well established and standardized for some of above mentioned systems. For example, telecom and datacom systems use 48V dc, trams and metros 600-750 V dc, airplanes ±270 V dc, etc. There is a potential advantage of dc- over the ac- architecture that allows development of less copper more silicon systems with the higher reliability, lower installation cost, higher controllability and definitely easier interconnection.

Beside the dc distribution systems already proposed for commercial and residential applications [31-36] similar dc power distribution systems are currently being considered for datacom centers in Japan, Europe, and USA [37-39] as well as for PHEVs and aircraft power systems [40,41].

1.1.3. Terminal Behavioral Modeling

An extensive work has been done up to now on modeling and capturing the low frequency dynamic behavior of the system components in order to address system interactions between converter modules and passive filters for dc distributed power systems [42-44], study effects of converter-generated switching harmonics on system resonances, and power quality in ac and dc systems [45,46]. However, system-level design is significantly held back by the fact that system engineers rarely have access to all the information required to model converters and/or system components, other than specification and data given in the datasheets. This problem is even more alleviated in a complex distribution systems built of power converters, active and passive filters and loads, all manufactured by different companies. Design of such systems then entirely relies on the experience of engineers, information provided in the specifications and ability to test the system under different operating conditions.

As a possible solution to previously described problems, terminal-behavioral modeling of converters became a widely accepted way of addressing not only low-frequency dynamic behavior of the converters [47-49], but also the high frequency EMI [50,51], as well as efficiency, system stability, inrush current, protections, start-up and remote on-off control [52]. This modeling dominantly exploits generic model of the power electronics components with the single, two wire input and output, un-terminated two-port network using inverse hybrid g-parameters [53-55].

1.2. Thesis Outline

In Chapter 2, renewable energy ac-nanogrid system along with the vehicle-to-grid technology for the future PHEV implementation is presented. The large-scale model is built and tested in the laboratory environment covering a few modes of operation that are supported with both, theoretical explanations and experimental results.

Chapter 3 of this thesis shows structure and operation of the dc-nanogrid system addressing all system components chosen as an inherent part of the proposed architecture. This chapter shows how dc bus signaling technique is contemplated for the energy management of the renewable energy sources and their maximal utilization.

Modeling and analysis of the simplified dc-nanogrid system is performed in the Chapter 4 by using full average models of the system components. Analysis covers operational behavior, load shedding and addresses small-signal stability.

Chapter 5 presents terminal behavioral identification and modeling of the dc-dc converters. As it will be shown, converters are measured on-line, during operation at the desired operating point, and their low frequency dynamics is identified by the means of the four transfer function characteristically used in two port network models. Transformation that gives un-terminated transfer functions from the terminated (measured) ones is also developed and explained in this section. Verification and validation of this modeling approach are also presented in this Chapter.

In the Chapter 6, terminal behavioral modeling addresses the non-linear static behavior of the dc-dc converters, assuming that the converter dynamic doesn’t change in the different operating points. Developed and shown are so-called hybrid terminal behavioral models and their verification and validation with the use of average models and real converters respectively.

Chapter 7 gives some conclusions and directions for the future work on the future electronic power distribution systems for the residential application as well as future steps in the terminal behavioral modeling.

Chapter 2. AC-BASED RENEWABLE ENERGY NANOGRID

Increasing environmental and economic problems on one side, and lower cost and higher availability of smaller generating systems (i.e. solar cells, wind turbines) on the other, have opened new opportunities for electricity users to generate power on-site. Along these lines, the so-called *microgrid* is a widely known and accepted concept that comprises energy storage and a larger number of generating units in order to get the most from the naturally available renewable energy sources [56]. Although its structure is more complex, and for the meantime a more expensive one, it provides unparalleled flexibility for the residential house applications. On the other hand, Plug-in Hybrid Electrical Vehicles (PHEV) present a promising, emerging technology for the future home since in general, the average personal vehicle is parked at the house for approximately 15 hours per day, which makes them potentially available for Vehicle-to-Grid (V2G) operation more than 60% of the time. An intelligent synergy of these two concepts combined with an advanced system control can provide a great platform for developing a residential house renewable energy solution at the lower power level.

2.1. AC Nanogrid

Utilizing PHEV, nanogrid has the ability to isolate a house from the utility grid (or microgrid), intentionally due to a fault or other abnormal grid conditions, work in the stand-alone mode, synchronize and reconnect to the utility grid, without load power interruptions. PHEV, with a built-in bidirectional power converter, presents the opportunity for demand-response operation in the grid connected mode, whereas in the islanded mode, it can perform frequency and voltage regulation of the power bus. The basic idea behind the V2G technology is that electric vehicles can provide power to the grid when parked and plugged in [57], and in order to function in V2G mode, PHEV must be equipped with a bidirectional power converter and additional battery pack. Having this, a two way energy flow is possible – when the power demand is low, PHEV's batteries can be charged and when high, batteries can be discharged and thus perform voltage and frequency regulation by matching generation with the load demand [58].

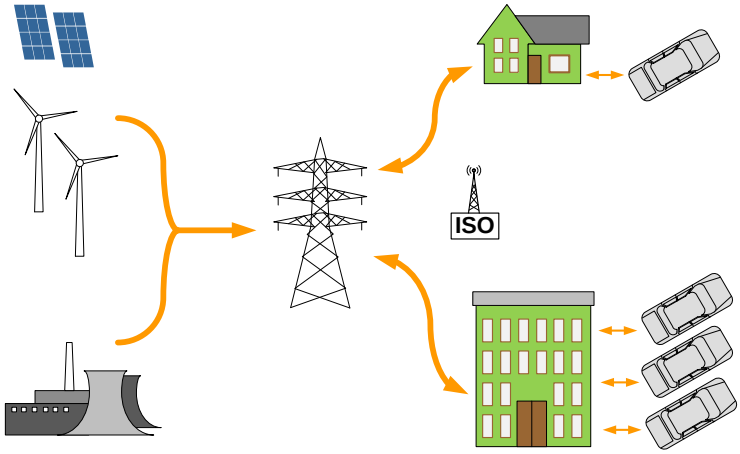

Figure 2.1: An illustrative schematic of the V2G implementation [57]

Figure 2.1 shows the basic concept of the V2G technology. As depicted, electric vehicles can be connected either to the house (one or more vehicles) or to the facility (fleet of vehicles) and perform the V2G operation. Charging and discharging of the vehicle's battery can be performed according to the remote commands from the grid operator or Independent System Operator (ISO). The ISO must continuously tune the balance between the production and consumption of power in specific control areas since the mismatch might cause the grid frequency to deviate from the nominal operating point of 60Hz. Also, by getting demands for reactive power from the ISO, vehicles can perform the voltage regulation at certain points and even maintain the unity power factor at the house or other facility power terminals [59].

The most significant electric service markets include base load, peak power, spinning reserve and regulation. V2G appears unsuitable for the first two, since they are accomplished by base-load power plants (nuclear and coal-fired) and peaking power plants (gas turbines and hydroelectric plants) respectively. But in the fast response power service markets, like spinning reserve and regulation, V2G could be a very promising technology [59].

2.1.1. System Description

The proposed home uninterruptible renewable energy system is shown in Figure 2.2, with the essential components. The house can have a photovoltaic and/or small wind turbine interconnected into the Integrated Power Hub (IPH) - an integrated solution with all of the equipment enclosed in a single cabinet. The IPH can comprise an internal single or three phase bus-bar for interconnection of available renewable sources, PHEV, power meter, synchronization contactor, circuit breakers and system controller. The basic idea of introducing the IPH is to develop a system that can be easily installed in the house, without any substantial modifications and rewiring. As shown in Figure 2.2,

the IPH can be installed in the residential house at the point between the house power terminals and existing load breaker box.

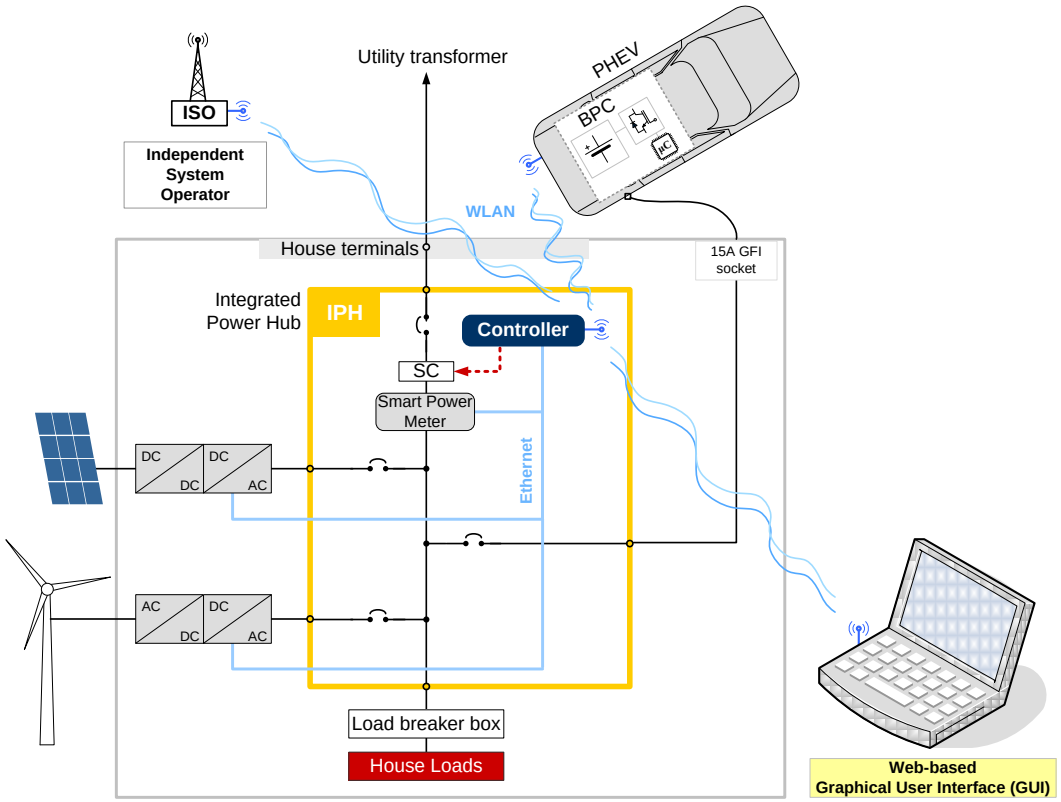

Figure 2.2: Home uninterruptible renewable energy system

The PHEV comprises the Bidirectional Power Converter (BPC) interconnected to the additional vehicle's battery. The BPC can perform a full, four-quadrant demand-response service according to the commands received from the power system operator as routed to the BPC from the Power Hub Controller (PHC). The BPC can perform an advanced active algorithm for islanding detection, and island the house when a grid outage occurs. In islanded operation, the BPC can supply power to keep all high priority loads and renewable sources to continue functioning in the stand-alone mode [60,61].

The proposed system also includes a supervisory control and data acquisition unit called the Power Hub Controller (PHC) as a main part of the IPH. One of the PHC's most important functions is the monitoring of system components by gathering data (current, voltage, THD and other) over communication lines. The collected data is fed to the web-based graphical user interface and used for additional control algorithms. The PHC also captures data and commands from the power system operator for the V2G service, and transmits them to the vehicle.

In order to avoid using many current and voltage sensors or power meters to collect

data into the controller, the PHC uses a 10/100 Mb/s Ethernet IEEE 802.3 communication protocol. The PHC establishes communication with all control boards in the converters that are part of the system, as well as with the smart power meter (usually connected to the utility grid side). Figure 2.2, shows a wired Ethernet communication with all converters and with the smart power meter; the communication with the bidirectional converter can be wireless LAN IEEE 802.11 or power line communication. The data fed to the controller are for the internal algorithms, data logging, and/or graphical user interface.

The Power Hub Controller can play an important role in the demand-response function implementation. It is envisioned that the ISO will be sending commands for demanded active and reactive power every few seconds in order to ensure frequency and voltage stabilization. The PHC can read data from the ISO and transmit the requirements to the vehicle over the wireless or power line communication channel. Having a controller installed in the house/facility for monitoring of the house can substantially improve V2G technology. As shown in the following section, an improved power factor correction, power management, synchronization and many other assets can be achieved.

2.1.2. Modes of Operation

The future home uninterruptible renewable energy system has the capability to work in two main modes of operation: grid-connected mode and stand-alone mode. The system is capable of making a smooth, uninterrupted transition between these modes by performing an advanced islanding detection and resynchronization algorithm.

The mode transition power cycle is shown on the Figure 2.3. The following discussion provides brief explanation of these modes.

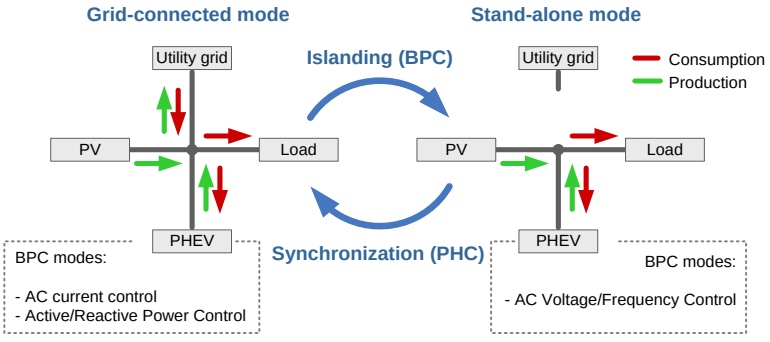

Figure 2.3: Main and transition modes of the future home uninterruptible renewable energy system

A. Grid-connected mode

In this mode of operation, the power hub controller sets commands for charging or discharging of the PHEV's battery, either through locally determined set-points or

through V2G operation in conjunction with utility regulation or demand-response requests. The BPC then regulates AC current/power by working in all four quadrants of the P-Q plane. The utility grid is connected and acts as the regulated voltage source. All local renewable sources are interconnected and operate as current sources. When the renewable energy production overweighs consumption, the house sources energy back to the utility grid.

Depending on the State of Charge (SOC) of the PHEV's battery, the vehicle will respond to ISO demands with the power vector within the S-circle as shown on the Figure 2.4, where the $S_{BPC(max)}$ is the maximal apparent power limited by power converter and/or current rating of the cable for the vehicle connection.

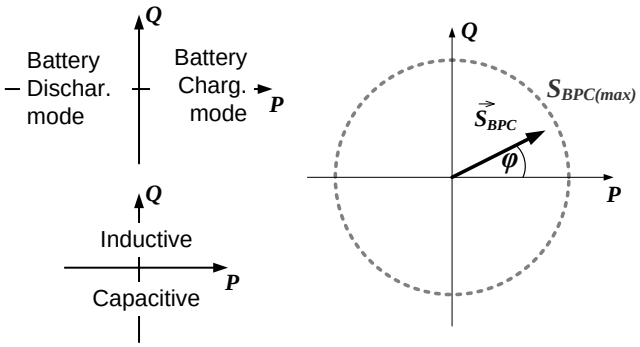

Figure 2.4: Four-quadrant power response of the electric vehicle

After the connection to the vehicle is detected, the PHC will acknowledge the ISO and communicates the capability of the vehicle (max apparent power, minimal set, maximal set and instantaneous SOC of the batteries). Afterwards, the ISO will send demands accordingly.

$$\begin{matrix} P_{ISO} \\ Q_{ISO} \end{matrix} \rightarrow \text{if} \begin{pmatrix} SOC < 40[\%] \\ \textbf{AND} \\ P_{ISO} < 0 \end{pmatrix} \textbf{OR} \text{ if} \begin{pmatrix} SOC > 90[\%] \\ \textbf{AND} \\ P_{ISO} > 0 \end{pmatrix} \rightarrow \begin{matrix} P_{dem} = 0 \\ Q_{dem} = Q_{ISO} \end{matrix} \tag{2.1}$$

If the power demands received from the ISO do not fall within the limits set according to the SOC of the vehicle's battery, the power hub controller adjusts the data according to the constraints listed in (2.1), and sends them to the PHEV. Here P_{ISO}, Q_{ISO} are the active and reactive power demanded from ISO, whereas P_{dem}, Q_{dem} are the active and reactive power transmitted to the vehicle from the power hub controller. The minimum (40%) and maximum (90%) state of charge of the vehicle's battery are arbitrary values, and depend on the type of the battery used.

One advantage of having the PHC installed in the house/facility is the ability of the PHC to control the power factor at the house/facility power terminals. When the ISO

sends demands directly to the vehicle, the vehicle will respond with the demanded power factor seen at the vehicle power terminals, but all the loads connected to the house system will change the power angle seen at the house/facility power terminals. With the PHC installed, demands coming from the ISO can be changed and the demanded power angle will be, as shown on the Figure 2.5, obtained at the house/facility terminals.

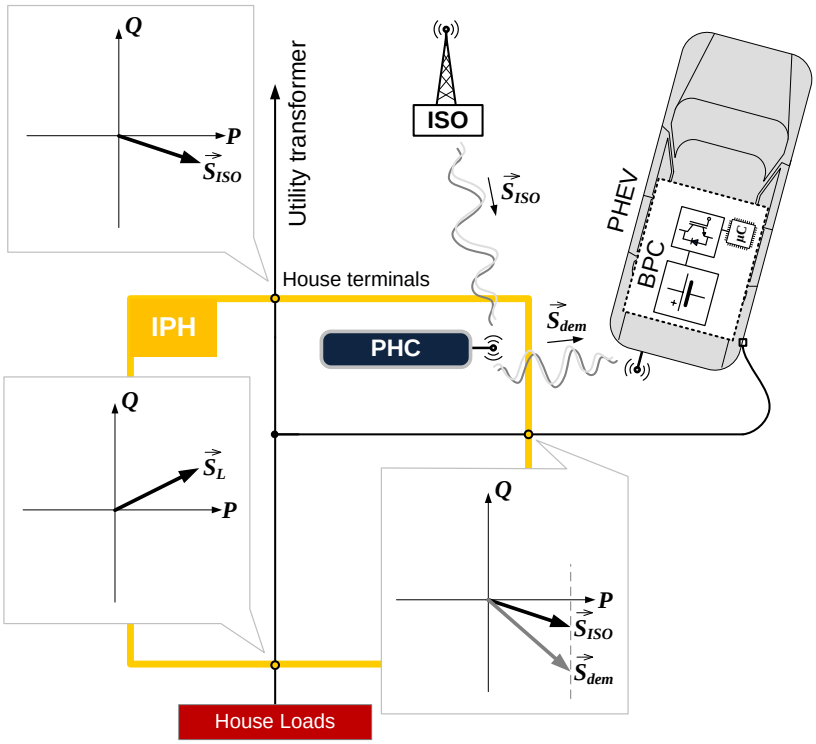

Figure 2.5: Power factor correction of the system

The system flexibility results from the fact that the PHC collects data from all renewable sources, as well as from the power meter connected to the grid side. Since the house power system is connected in a star configuration, load complex power can be obtained as a dependent variable and thus the corrected power factor can be calculated in every sampling cycle of the PHC. The BPC in the vehicle can then be commanded to respond with a different factor than requested by the ISO. The ISO demanded power factor will then result at the house/facility terminals according to (2.2).

$$\begin{matrix} P_{ISO} \\ Q_{ISO} \end{matrix} \rightarrow \left(\mathbf{PHC} \right) \rightarrow \begin{matrix} P_{dem} = P_{ISO} \\ Q_{dem} = Q_{ISO} + Q_L \end{matrix} \tag{2.2}$$

B. Grid-connected to stand-alone mode transition

The BPC of the PHEV can detect voltage and frequency deviations and/or power outages of the utility grid, and smoothly island the house. A large percentage of commercial power converters currently being installed for renewable sources are grid-tied inverters featuring Maximum Power Point Tracking (MPPT) control and simple anti-islanding detection algorithms; such inverters turn off within a few line cycles after a grid outage occurs. Some inverters are able to work in the stand-alone mode, but they do not address the seamless transition between the modes of operation [62,63]. As such, to allow the house to become autonomous from the grid due to an outage, the BPC must perform fast, active islanding detection. According to [64], for distributed energy resource systems with installed power less than 30 kW, islanding of the system after the voltage and frequency disturbances occur must be completed within the clearing time given in the Table 2.1

Table 2.1: Islanding response time [64]

Voltage Range [%]	Clearing time [s]
V < 50	0.16
50 ≤ V < 88	2.00
110 < V < 120	1.00
V ≥ 120	0.16

Frequency range [Hz]	Clearing time [s]
> 60.5	0.16
< 59.3	0.16

C. Stand-alone mode

Operation in this mode is possible as long as the vector difference between the total load apparent power and the total power produced by the renewable sources is a vector within the circle with the radius equal to the rated apparent power of the BPC, as shown in Figure 2.6. The load has a stochastic behavior that cannot be predicted. The renewable sources feature MPPT mode, and therefore cannot follow the load curve for load power lower than their power rating. Thus, the BPC must provide the difference through either the charging or discharging of its battery system, while regulating the AC voltage and frequency on the bus to ensure the power equilibrium in the system. This system can work in the stand-alone mode only if (2.3) is satisfied.

$$S_{BPC(\max)} \geq \sqrt{\left(P_L - P_{REN}\right)^2 + Q_L^2} \tag{2.3}$$

Here, $S_{BPC(max)}$ is the maximal apparent power of the BPC, P_L,Q_L are the active and reactive load power, and P_{REN} is the active power produced by the renewable energy sources. Commercial inverters generally work with unity power factor, and hence Q_{REN} is zero in (2.3).

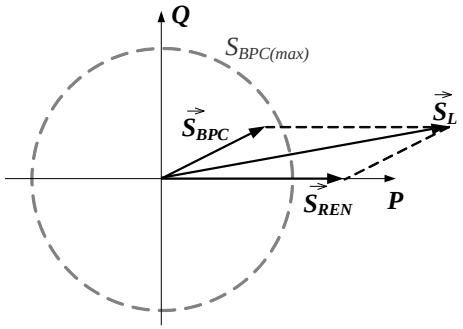

Figure 2.6: Complex power plane of the BPC with the safe operating region

D. Stand-alone to grid connected mode transition

After the utility grid re-establishes itself from an outage, the house can be reconnected to it. The challenge here is that the PHEV does not sense the grid side voltage and frequency directly as shown in Figure 2.7. The grid voltage and frequency are sensed by the PHC. The PHC compares the voltage on the grid side with the voltage on the BPC side, and sends instructions to the BPC over the wireless or power line communication to adjust the voltage and frequency to match the grid voltage.

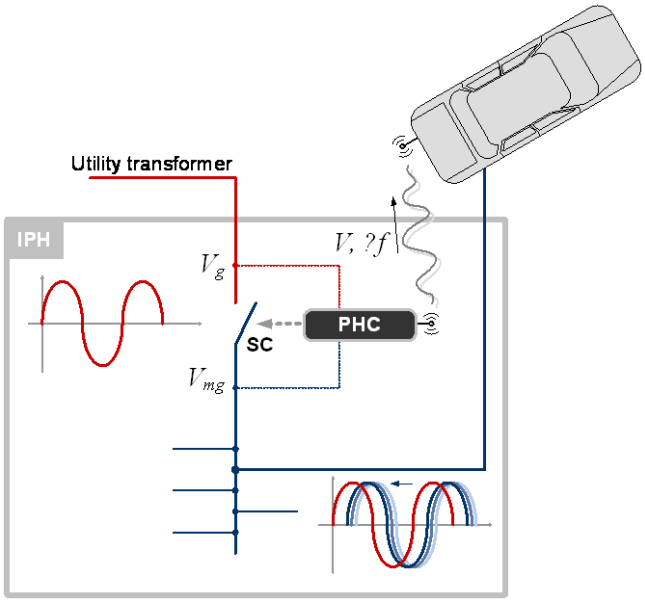

Figure 2.7: Synchronization over the WLAN

Before the resynchronization happens, BPC works in the AC voltage regulation (stand-alone) mode keeping the house voltage and frequency in the nominal range.

Once the synchronization conditions are met, the PHC closes the contactor SC, shown in the Figure 2.7. The contactor can be either mechanical contactor or solid state switch. After the PHC senses that the switch is closed, it sends a command to the BPC to switch to the current mode of operation, and resynchronization is finished. Because the loop is closed through the communication channel, the synchronization phase-locked loop (PLL) must be split between the PHC and the control system of the BPC. Communication latency issues can quickly arise and must be addressed in system software design.

2.1.3. System Realization

The proposed concept was tested using a laboratory setup that incorporates a 5.1kW PV array (Figure 2.8), and a 7kW bidirectional power converter interconnected to a 5kWh battery. The system components used in the test setup are detailed below, starting with the IPH.

A single-phase (split phase) integrated power hub was built for testing purposes and is shown in Figure 2.9. The Power Hub Controller used is a hybrid platform that incorporates a real-time processor and a reconfigurable FPGA for reliable stand-alone applications [65].

Figure 2.8: View of the CPES solar array and wind turbine mounted on the roof of Whittemore Hall, Virginia Tech, using Suntech 170W PV panels [source: www.suntech-power.com], and Cleanfield wind turbine [source: www.cleanfieldenergy.com]. Photos by CPES, 2008.

The IPH further comprises power distribution terminal blocks for the interconnection of the solar inverter, PHEV and various house loads. These loads were implemented using resistor banks; power level was adjustable in discrete steps via relays shown in the Figure 2.9. The switchable load relays emulate the stochastic behavior of the load in a real house - behavior especially important for testing the stand-alone mode of operation. Figure 2.9, also shows the wireless router for the demand-response data exchange with the PHEV and for connection to the internet. In addition, an Ethernet switch is used as the wired communication interface between the PHC and the other system components: the power meter, and solar inverter. The same

figure moreover shows two voltage sensors connected to the PHC for the system resynchronization to the utility grid (Figure 2.7, shows connection points for these sensors inside the IPH).

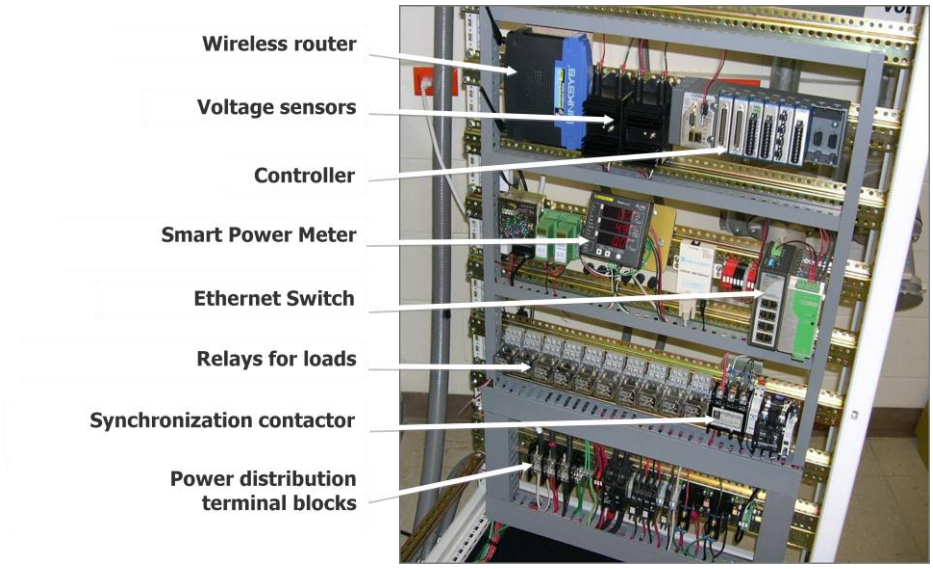

Figure 2.9: Single phase (split phase) Integrated Power Hub (photo by author, 2008)

The Bidirectional Power Converter (BPC) used in the system is a modified industrial variable speed drive with a full-bridge topology, which was selected due to its capability to work in all four quadrants of the P-Q plane. This allows any of the previously mentioned modes of operation to be implemented. The BPC and the NiMH battery pack used in the system are shown in the Figure 2.10. For testing purposes, the BPC and its battery pack were mounted on the bench and connected to the IPH via the cable as shown in Figure 2.2.

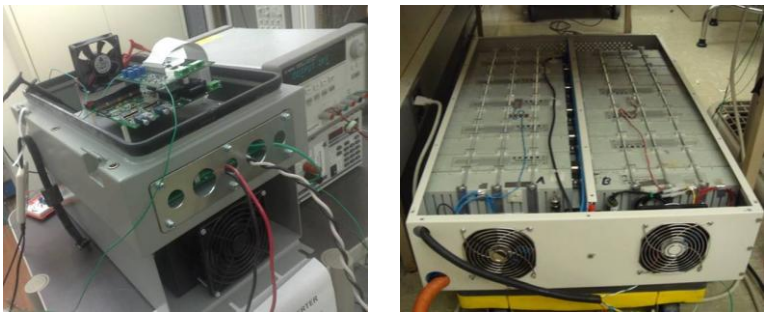

Figure 2.10: Bidirectional Converter (left) and a NiMH battery pack (right). (photos by author, 2008)

More details about the advanced control algorithms implemented in the DSP/FPGA of this converter are explained in [60,61,63,66].

The Supervisory Control system was developed using LabVIEW graphical programming tools, the LabVIEW Real-Time Module, and the LabVIEW FPGA

module. For the demand-response service in the grid-connected mode, the ISO signal was emulated with LabVIEW code running on the laptop and transmitted to the PHC via the wireless IEEE 802.11 protocol.

The system power flow was monitored via the web-based Graphical User Interface (GUI) also developed in LabVIEW. Figure 2.11, shows the main web-page that displays power flow in the system.

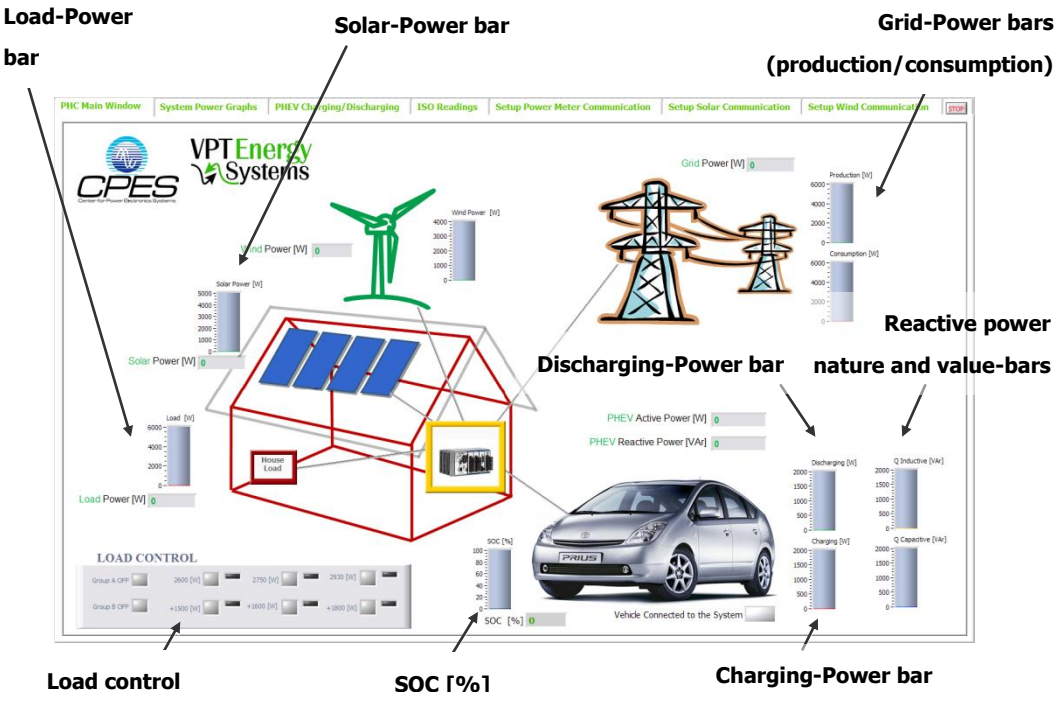

Figure 2.11: GUI main web-page displaying instantaneous power flow in the system

An application was developed for the testing purposes that allowed for the load level to be adjusted via the same web-page. Important PHEV data are shown on this page including bidirectional active power flow (charging/discharging) and reactive power (inductive and capacitive) flow as well as the state of charge of the batteries. The same GUI was developed to support the wind turbine. The wind turbine was not connected to the IPH in this stage of the project, but communication with its power converter was established and tested.

Figure 2.11, shows the graphical user interface dedicated to the PHEV commands. The user interface allows for the selection of either an automatic or manual mode of operation. In the automatic mode, the BPC responds directly to the data from the ISO, and in manual mode, setting the charging-discharging profile and power factor can be created directly using the virtual knob or keyboard entry.

2.1.4. Experimental Results

The main modes of operation of the future house, grid-connected mode with the demand-response implementation of the V2G technology and the stand-alone mode have been fully tested using the laboratory setup. This section presents steady-state test results captured on the BPC terminals for the system working in these modes. The transition from the grid-connected mode to the stand-alone mode, has been also fully implemented and tested. System synchronization, or transition from the stand-alone mode to the grid-connected mode, is still under development, but some results from this mode are shown and explained below.

Figure 2.12, shows the grid-connected mode of operation with the power demand from the ISO. The captured waveforms show results for a demanded change from *P=300* W and *Q= 0* var to *P=-420* W and *Q=-270* var. This corresponds to a power factor change from 1 to 0.84.The fast and smooth response to the requested P/Q change illustrates the value of using V2G technology with a large fleet of vehicles as spinning reserve for improvement of the power system stability. Figure 2.13, shows a stand-alone operation having the BPC in the PHEV regulate the house voltage to 120V, 60Hz with a non-linear load. In this mode of operation, ISO demands are ignored since the grid is not connected.

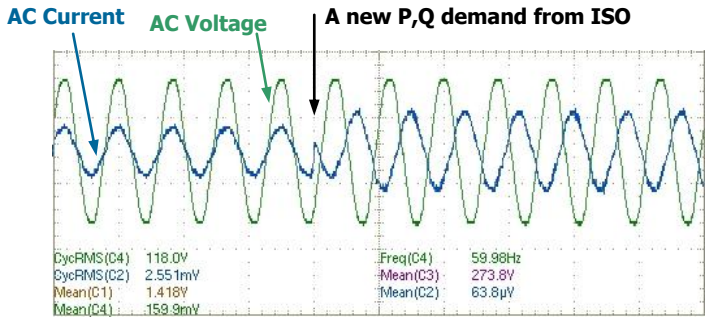

Figure 2.12: Response of the BPC to the change of the active and reactive power demand from the ISO

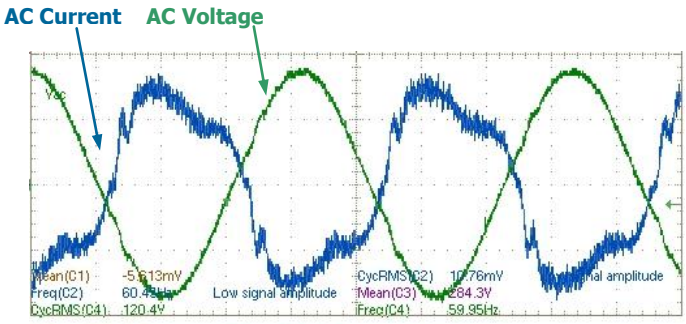

Figure 2.13: Stand-alone mode of operation of the BPC

Islanding is shown in the Figure 2.14. The moment when the grid is disconnected (forced action via a local circuit breaker) is also shown in the picture. The fast islanding algorithm [63] senses this condition and the BPC smoothly changes the mode of operation from grid-connected (current regulation) to stand-alone (voltage regulation) mode without any power interruptions or voltage sags since the BPC was discharging the battery before the grid was disconnected (load matching condition). The moment when islanding is detected and the mode of operation changed can be also clearly seen on this picture. The negligible current transient can be noticed at the time when the BPC changes the mode.

Figure 2.15, shows a snapshot of the synchronization of two voltages, grid side voltage and BPC voltage. In this test, the synchronization algorithm triggered the digital output pin of the PHC controller which in turn closed the solid state switch when the phase difference between the two voltages was 1.1°. At this time, since the synchronization testing is in the final stage, the PHEV side (or BPC) was disconnected from the solid state switch. This test illustrates the operation of the synchronization algorithm, but the real reconnection was not tested. The synchronization algorithm testing resulted in switch closure phase differences ranging from -3.4° to 1.8° for 25 repetitions.

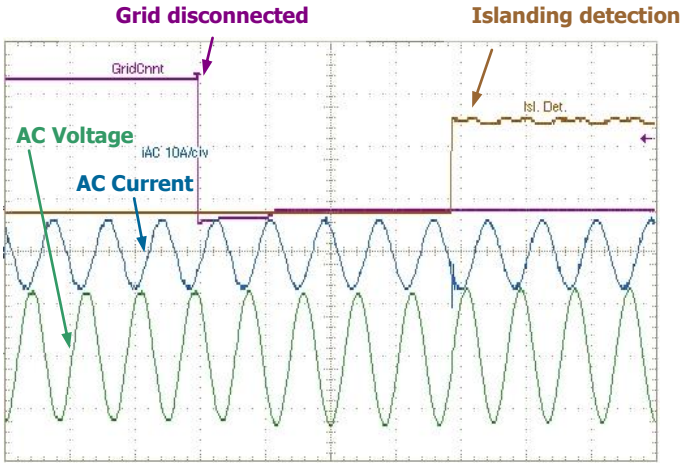

Figure 2.14: Islanding of the house from the utility grid

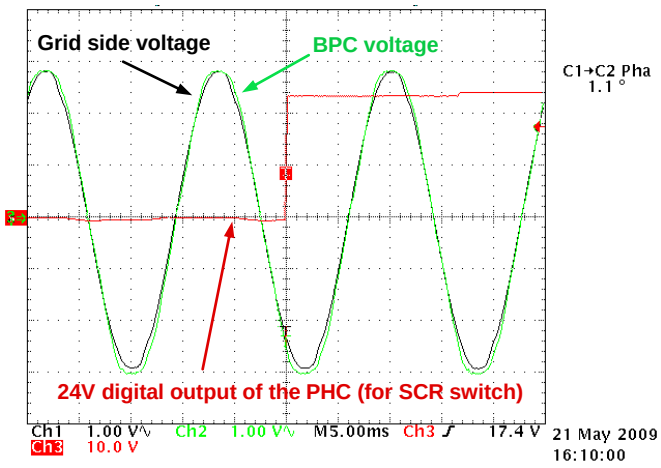

Figure 2.15: Synchronization of the utility grid and the BPC (oscilloscope snapshot)

2.1.5. Conclusion

The utilization of the Plug-in Hybrid Electric Vehicle described in this chapter shows an immense possibilities of the system comprised of dc battery and bi-directional power converter. System on the dc side is completely dynamically decoupled from the ac grid and disturbances that can occur in it, current limits of the converter provide protection on both ac and dc side, reactive power compensation on the ac side is possible without discharging the battery, and many other assets. All of this is opening the question: what if the system on the dc side is actually a house with all appliances, sources and loads, and the bidirectional converter serves as an interface to the utility grid? Then all the advantages listed above will actually hold for the house system offering better controllability, higher overall efficiency and lower system cost.

Chapter 3. DC-BASED RENEWABLE ENERGY NANOGRID

Although still under theoretical and practical debate, dc systems became widely recognizable as the best candidates for replacement of the conventional alternating current systems. A dc-based nanogrid concept will be introduced in this chapter.

3.1. Contemporary Home Electrical Architecture

Power electronics, more than ever, can play a significant role in society's transition to sustainable development. It is widely recognized that homes provide one of the largest opportunities for more efficient energy utilization as well as distributed energy generation.

Contemporary homes are envisioned to be energy sustainable and powered by different types of renewable energy sources, together with utility grid. The sources would mainly include photovoltaic solar cells (PV), wind generators, micro-turbines, fuel cells, and local energy storage [6]. Plug-in Hybrid Electric Vehicles (PHEV) are highly expected to become an inherent part of the future home [7].

Figure 3.1 shows a one line diagram of electric architecture in a contemporary home that can be seen today in the areas with the high living standard that in addition naturally offer an abundance of renewable energy sources.

Power converters often used for the PV are most commonly unidirectional two-stage converters featuring the step-up (boost) dc-dc converter stage and a single- or three-phase voltage source inverter stage for adequate interface with the single or three phase utility grid [64]. New converters for small wind turbines are also two-stage power converters, comprising the three-phase PWM rectifier and a voltage source inverter. Energy storage and PHEV typically require bidirectional dc-ac converters for the optimal battery utilization on one side, and ac-line interface at the other.

Household loads more and more contain power electronics converters that optimize their operation and boost up the efficiency, as illustrated in Figure 3.1. A modern washer, for example, features the variable speed drive that provides a maximal torque per current to the brushless motor, and thus more efficiently utilizes the energy compared with the conventional pole-changing induction motor often found in the older type of washers. Even once the biggest resistive load in a home, a stove, is being replaced with the one featuring induction heating and now becomes an electronic load to the system. Lower-power consumer electronics devices as TV, computer, audio and other portable ones, inherently comprise the power electronics circuits for operation, featuring the "power aware" function enabled by it [67].

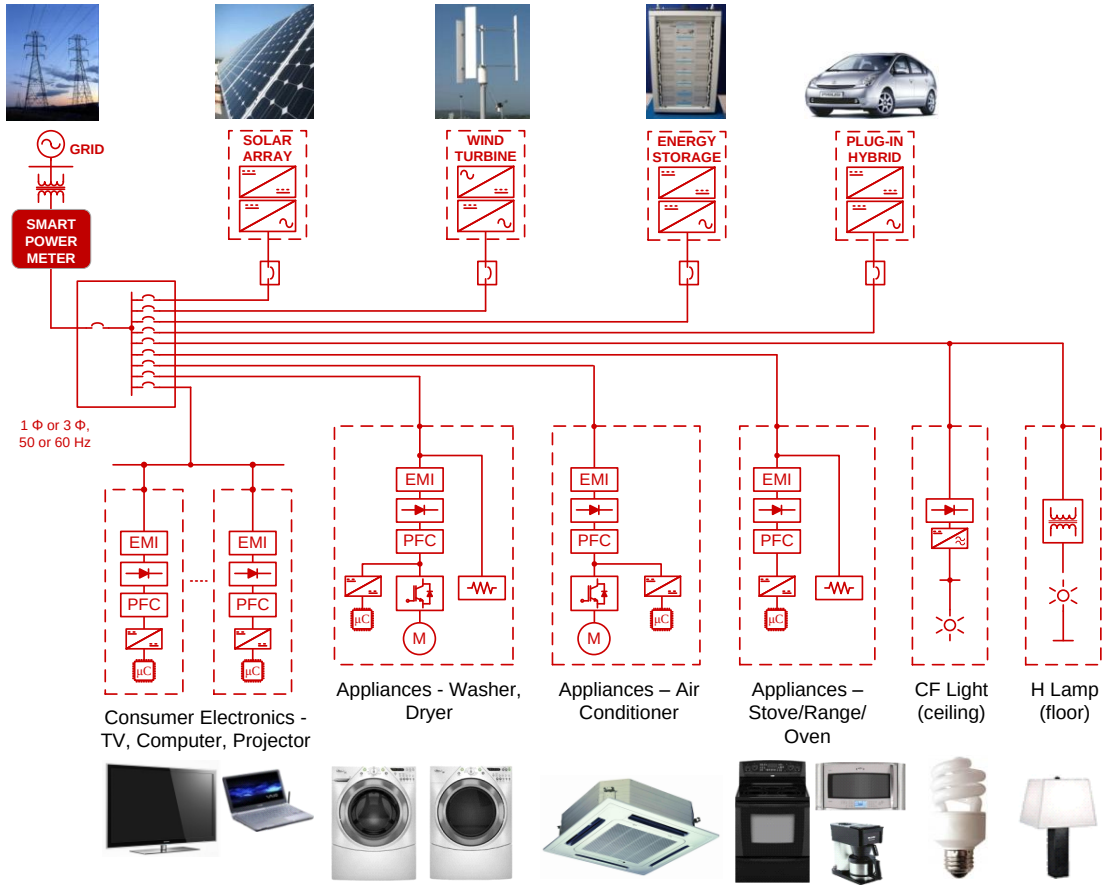

Figure 3.1: Electrical architecture of a contemporary home

Practically all electronic loads comprise a two-stage power conversion, where the front-end converter consists of a rectifier, Electro-Magnetic Interference (EMI) filter, and unless very low in power (less than 70W) they have a power factor correction (PFC) circuit, as shown in Figure 3.1.

It is envisioned that through appropriate design of these devices and by operating them in a coordinated fashion, net residential fuel-based energy use can be reduced dramatically, while simultaneously increasing the perceived comfort levels in terms of lighting, temperature, water and air quality.

Power electronics plays a major role in the successful implementation of the home energy system shown in figure 3.1. The majority of the electrical household functions identified in this figure depend on the availability of compact, high reliability, low-cost power electronics to convert electrical power into the form and amplitude required by the source or load.

As seen in the Chapter 2, above described system can work in two major modes of operation, grid connected and stand-alone mode, and perform two major transitions,

islanding and synchronization. The bidirectional power converters from the PHEV and/or energy storage are responsible to isolate the home from the utility grid in the case of a fault or other abnormal grid conditions, perform the frequency and voltage regulation of the home ac-line in the stand-alone mode, and synchronize and reconnect the home to the utility grid without load power interruptions. This also presents the opportunity for demand-response operation while in the grid connected mode.

However, in the contemporary home electrical system, as well as in the traditional electrical systems, the dynamics of generation (sources), and consumption (loads) are fully coupled. Whatever voltage and/or frequency deviations happen in the utility grid, they are automatically "seen" by all of the system components through the 50 or 60 Hz coupled electrical network. The large transients at some point in the power system directly influence stability of the whole power systems producing brownouts (voltage sags) and sometimes can lead to an inevitable system blackouts.

A possible solution to the decoupling problem may be found in the PHEV example presented in the Chapter 2. The bidirectional converter is an interface between the battery (dc side) and the utility grid (ac side), thus two systems are dynamically decoupled. Converter is a closed-loop system featuring a much higher control bandwidth than what are usually frequencies of disturbances on the utility grid side, therefore dc side's high immunity to these disturbances.

Knowing that, and following an example of PHEV, the whole nanogrid system could actually be interfaced to the utility grid via bidirectional converter, and thus dynamically decouple itself from utility. Consequently, nanogrid's internal architecture could be completely independent in a sense of the voltage level, frequency, phase and can even have its own EMI specifications as well as the other predefined standards. Internal frequency, for example, can be from 0 Hz to couple of kHz, although advantages and disadvantages of the choice have to be much deeply explored and proved through the intensive research on this, particular, aspect.

One choice however, brings advantages that can be "a priori" taken as a good solution for the future power distribution systems, and that is dc nanogrid system. Compare to the conventional or even contemporary home electrical architecture, a dc-nanogrid system is expected to bring many advantages, starting with the fact that overall system efficiency could be higher, and the renewable energy sources can be more easily interfaced to a dc system with fewer power converters [8]. There are no frequency stability and reactive power issues, and no skin effect and ac losses. What is more, the consumer electronics, LED lighting and variable speed motors can be more conveniently powered by dc.

3.2. DC Nanogrid

A conceptual dc-based nanogrid system is shown in the Figure 3.2 emphasizing its structure, interconnections and system components. For the comparison with the ac-nanogrid system from above, dc-nanogrid is shown with the same number and type of components.

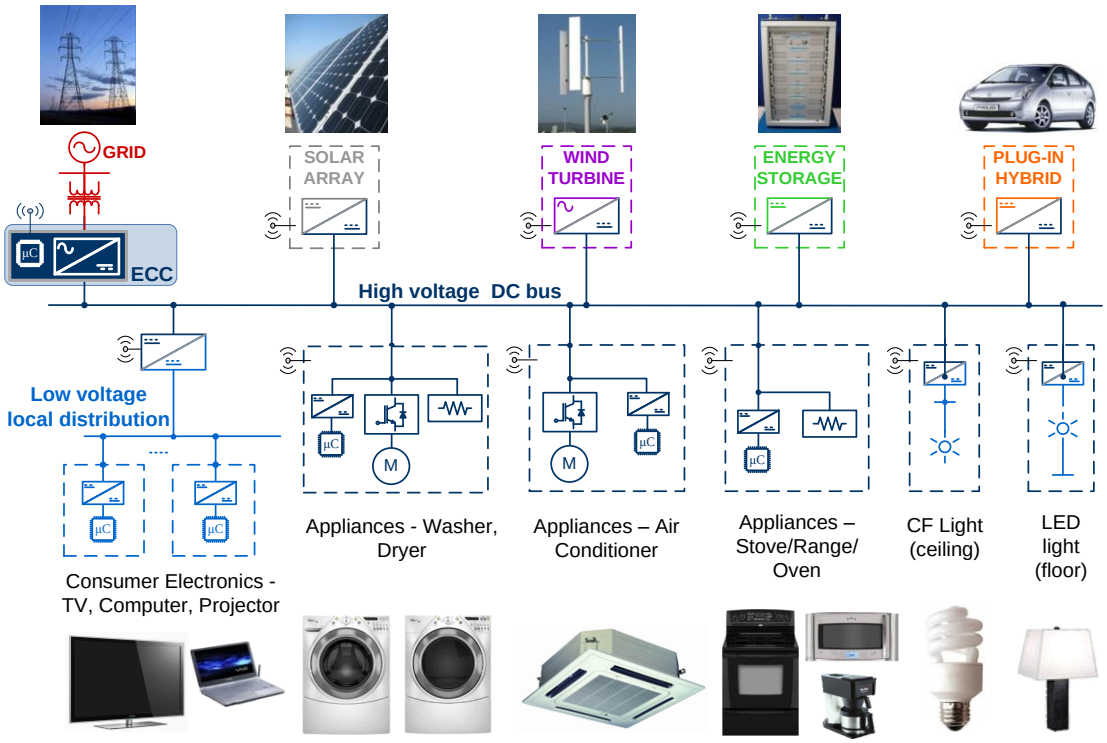

Figure 3.2: A dc-based nanogrid system in the future home

Dc-based nanogrid system is bus structured, all-converter system that just at the first look, and "by-eye" comparison with the ac-nanogrid system, brings up the conclusion that dc-nanogrid system has significantly simpler structure and lower number of components. An inverter stage of the power converters for renewable sources, battery storage and PHEV, mandatory for ac-nanogrid system (and other *ac* systems in general) in order to interface them to utility grid, here is not required. On the other hand, consumer electronics and appliances for the dc system do not need to comprise front-end rectifier, EMI filter and PFC stage and can be connected to the dc bus directly via their dc-link.

Dc-based nanogrid is interfaced to the utility grid via bidirectional power converter that can work in all four quadrants of the complex power plane as shown in the Chapter 2. It can isolate the house from utility in the case grid fault occurs, and reconnect it back

when fault is cleared. What is more, it can work with any demanded power factor at the ac side together with an active power trading which allows for demand/response operation with utility Independent System Operator (ISO).

This bidirectional converter is a high density two-stage, H-bridge in series with a bi-directional SR dc-dc PWM converter with significantly reduced dc-link capacitor value [29]. This converter is envisioned to inherently comprise System Control and Data Acquisition (SCADA), control platform that would allow communication with ISO, as well as with other converters in the system depicted in the Figure 3.2. The so-called Energy Control Center (ECC) then emerges as a single package, energy solution for residential renewable energy systems and is shown in the same figure as an interface with the utility grid. Although the focus in this thesis will be put on the dc-nanogrid systems, in general, ECC can be single or three phase, ac-dc or dc-dc converter for either ac- or dc-nanogrid applications as shown in the [8,68].

The Figure 3.3 illustrates communication between the various components in the dc-nanogrid system and the ECC itself. ECC will be communicating with the internet in order to obtain forecast data: wind speed, solar irradiation, etc, used for the optimization of the nanogrid operation, as, for instance, load shedding in the case when weather forecast anticipates no wind and no sun in a few hours from the moment when reading was made. Also, by recording the user's habits in the sense of energy use during the day/month/year, ECC can build its own estimation profile of energy usage and an adaptive optimization algorithm would take an action to prepare the system for such an event. For example, recorded energy usage around the Christmas time every year shows a peak in the late afternoons. ECC would, knowing that from its history, ahead of time consequently keep the batteries fully charged by utilizing the renewable sources and also, whenever appropriate, even shed not high priority loads for the same matter that would not have done normally.

Communication with the ISO will be in the same fashion as the one described in the Chapter 2. After a some kind of agreement is made between the ISO and the user, it is envisioned that the ISO will start sending commands to the nanogrid system in the form of demanding active and reactive power. The communication will be bidirectional, where ECC will be updating ISO every T_u [s] with the maximum active and reactive power possible for delivery, and ISO will reply with the *P*[W] and *Q*[var] demanded every T_d[s] as shown in the Figure 3.4.

Both communications channels, one with the internet and one with the ISO, ECC will realize over the IEEE 802.11 (WLAN).

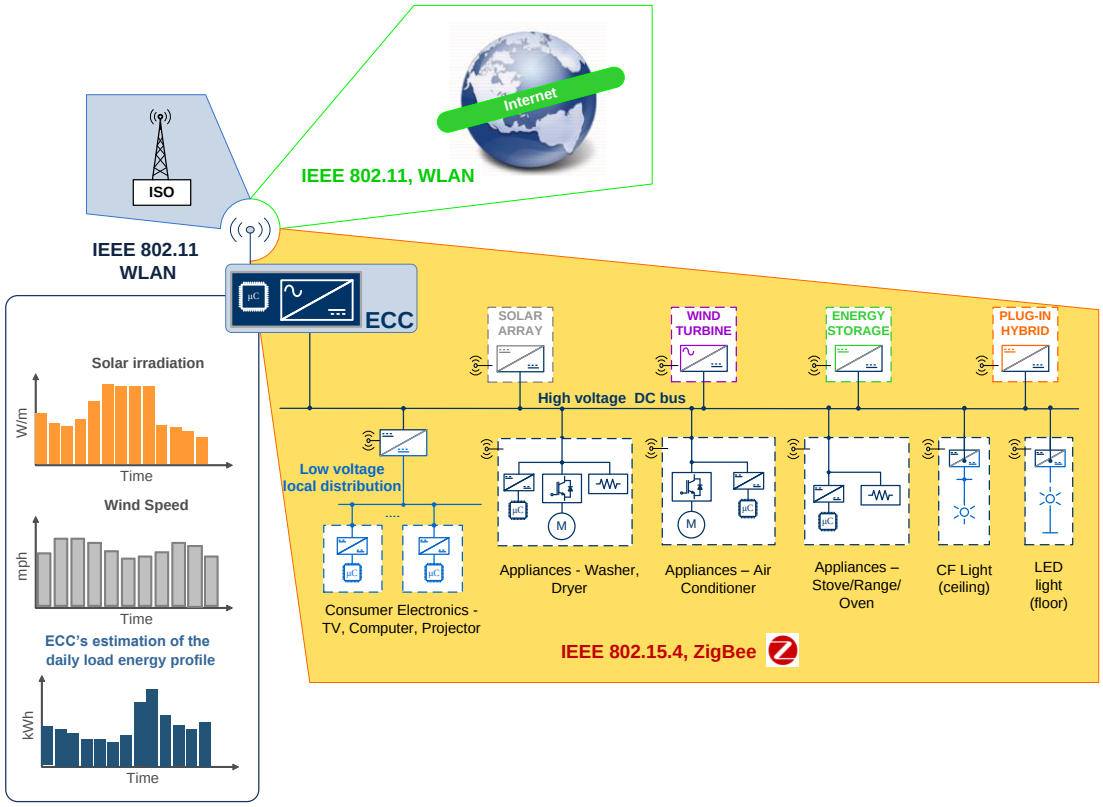

Figure 3.3: Illustration of communication within the nanogrid system

In order to perform power management operation and utilization of the nanogrid, ECC has to also communicate with all the power converters as well as with appliances in the house. Collected information will be used for Graphical User Interface (GUI), or optimization algorithm of the system components. User will be able to, at any time, access the system control webpage through the web browser, and set the priorities, limit demand/response operation values, or change set point temperature of the air-conditioner system in some part of the house. Communication channel between ECC and converters as well as with appliances will be realized over the IEEE 802.15.4 standard, known as ZigBee. Developing communication between the different components of the system significantly lowers down complexity of the system monitoring by avoiding the voltage and current sensors to be installed in every point in the system where is beneficial to obtain measurements.

Another benefit of utilizing power electronics in the architecture of the future home is the fact that converters are controllable and provide active current and voltage limiting, the electromechanical switchgear could be entirely eliminated from the system. Electrical architecture can be completely breakerless assuring that topologies comprise serial semiconductor switches which fail open in the abnormal failure mode. Therefore, dc-nanogrids may be able to provide increased energy efficiency, power

density, and reliability, with decreased installation and operational costs.

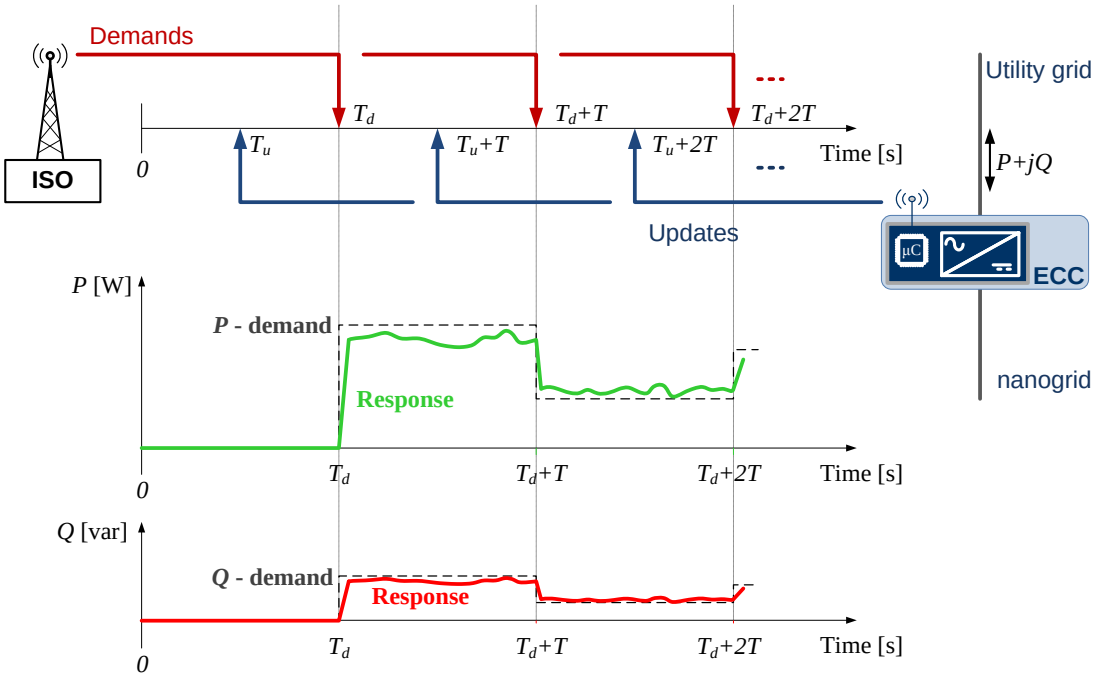

Figure 3.4: Illustration of demand/response operation between ISO and ECC

3.3. The Main Characteristics of the DC Nanogrid System

The choices for the appropriate voltage levels in residential dc systems are mostly results of engineers' subjective views and opinions, since dc system implementation is not enough mature, and an intensive research must be performed before some standards can be developed and recognized from the competent institutions. Therefore, voltage level(s) chosen for dc-nanogrid system that will be presented in this thesis should be viewed as a possibility, although some reasoning will be shown offering engineering persuasion for that matter, and the real conclusions are expected to be made after the large scale system is built and rigorous tests performed.

By looking in the Figure 3.5, it can be seen that the practically all of contemporary home appliances and consumer electronics devices above 70W feature boost PFC circuit. In order to support wide input voltage range satisfying standards in different countries of the world, from 100 V, 50 Hz to 240 V, 60Hz, output of the boost PFC circuit is mostly around 380 V, depending of the manufacturer. By having this voltage range as a choice of the dc-nanogrid bus voltage, transition from AC to DC power appliances would not require complex modifications and new topologies. In many cases, by only taking out the EMI, rectifier and PFC circuit, appliance can be connected

to the dc bus via internal dc-link as shown below in the Figure 3.5, and could be ready for fully functional DC operation.

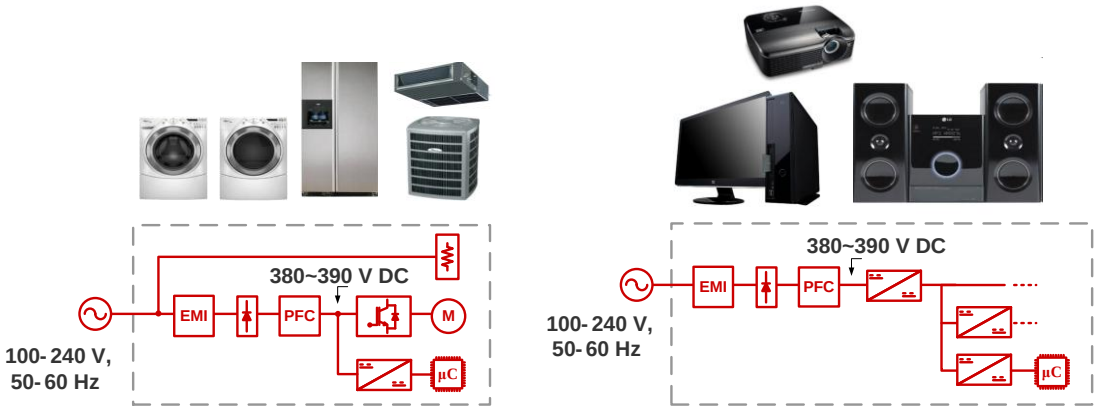

Figure 3.5: Electrical architecture of contemporary appliances

Practically, influenced by household loads and their easiest transition to future dc systems, voltage range in the dc-nanogrid is chosen to be 380 V ± 5% which gives a operating range of the nanogrid bus from 360 V to 400 V.

Figure 3.2 is also showing a low voltage local distribution dedicated to the low power consumer electronics devices as laptops, LED lights, etc. For this application 48 V was chosen to coincide with the standard telecom voltage levels where standards are fully developed and well understood, but also featuring safety and aesthetic attributes by offering possibility to be completely exposed to people with no danger of electric shock.

Depending on the application and the load requirement, this voltage can actually be lowered down to the level required by the device itself. Majority of dc-dc converters feature trim-up and trim-down voltage functions that can digitally be controlled. For this to happen, a low-voltage power plugs and sockets have to be able to communicate (ZigBee or Radio-Frequency Identification (RFID)) and exchange information just before the connection happens.

Connection of high voltage (380 V) appliances and consumer electronics, on the other hand, brings more difficulties and issues than in the low voltage case. This voltage level is dangerous for humans and must be safely enclosed for protection, but in the same time has to be functional and easily accessible. Dc outlets and plugs for residential applications are not yet commercially available and one possible solution to address this problem is shown in the Figure 3.6.

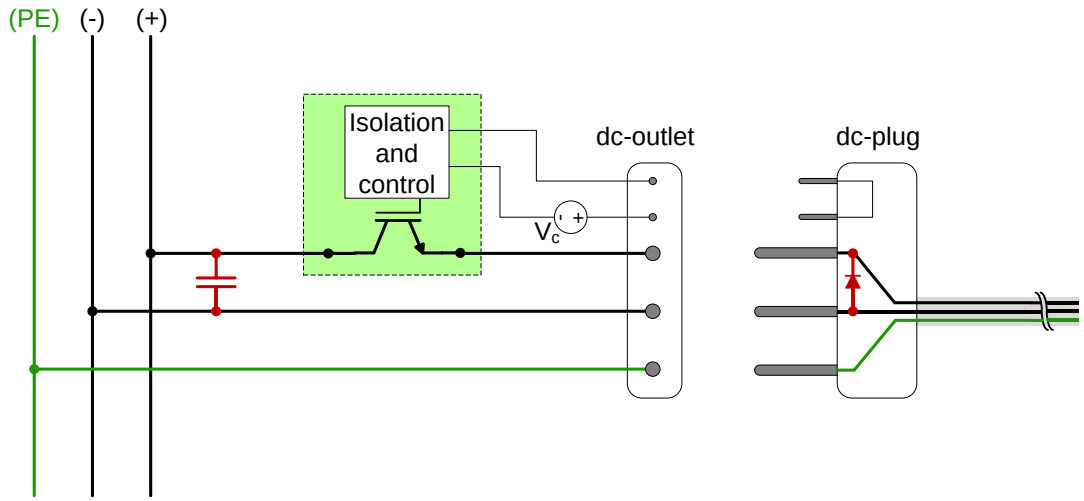

Figure 3.6: Power plug and outlet solution for dc-nanogrid

Dc outlet and plug are envisioned to be based on the 5 –pin connector. Three main, power pins are for the positive, negative and ground line while two smaller pins are control pins. The IGBT is placed in series with the positive line and is controllable through the appropriate driver. This semiconductor switch cannot be turned on unless the plug is plugged in, and the small wire-bridge in the plug itself provides the path for the control signal to the IGBT as illustrated in the Figure 3.6. When unplugging, a two shorter pins on the plug side are made shorter, which will as a consequence turn-off the IGBT before the main power pins are disconnected. The difference in the length of the power and control pins is enough to ensure turning-off time of the IGBT (nanosecond range) before the main pins are disconnected. Two goals are achieved with this configuration: an inevitable arcing inherently present when interrupting dc current, and also the outlet will remain non-energized after the plug is removed which significantly increases the people's safety. Figure 3.7 shows an equivalent electric circuit of the power outlet-plug structure from Figure 3.6.

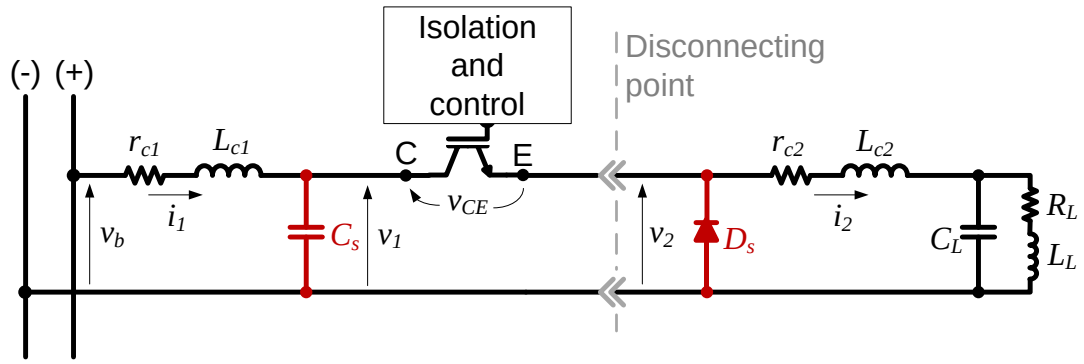

Figure 3.7: Equivalent circuit of the power outlet-plug structure from Figure 3.6

Interconnection cables between dc-bus and the outlet, as well as between the plug and the appliance, inevitable have some impedance that comprises series connection of dc-resistance and inductance. Interrupting flow of dc current has always been a challenging task due to the stored magnetic energy in the circuit reluctant to any change of current. Consequence of fast current change is a large voltage spike described by $v = L\mathrm{d}i/\mathrm{d}t$.

Figure 3.8 shows transient after disconnect of a plug shown in both, Figure 3.6 and 3.7 without added capacitor C_s and diode D_s. It is clearly seen that voltage spike reaches very large values that could potentially be very dangerous for people despite the fact that the surge does not last too long (a few hundred nanoseconds).

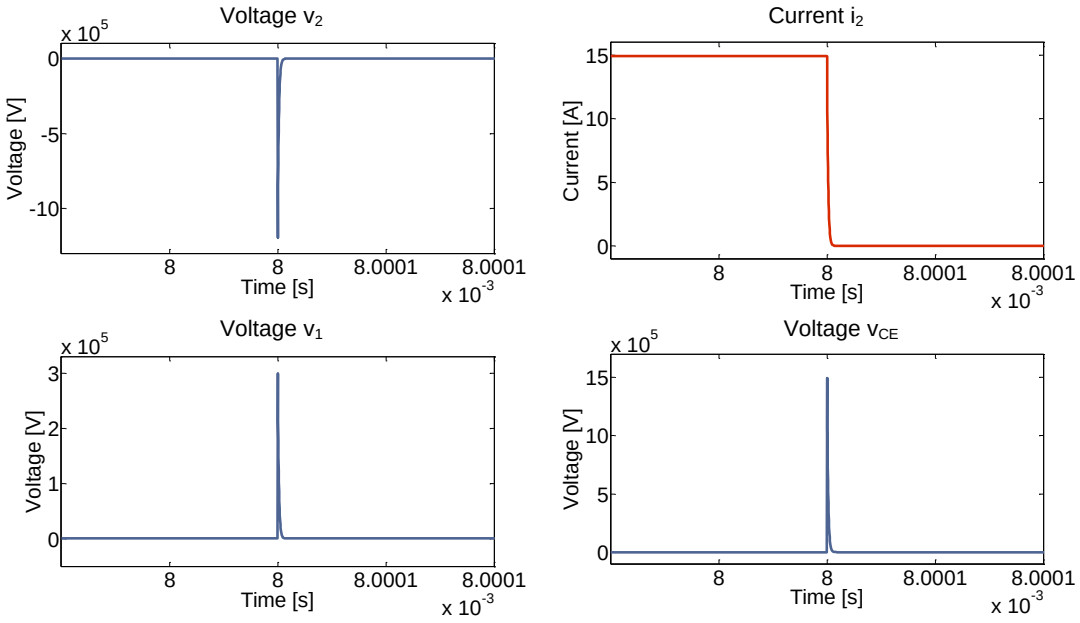

Figure 3.8: Transients as results of dc current interruption

Adding a freewheeling diode D_s inside the plug as shown in the Figure 3.6, can enable path for the current upon disconnection of the plug, and the magnetic energy stored in the cable and the load will dissipate through the internal resistance of the wire and the load. In the outlet side, between the IGBT and the wire coming from the bus, a capacitor C_s has to be added to protect the semiconductor device from the high voltage surge. Results are given in the Figure 3.10.

By looking at the Figure 3.7, the topology of the outlet-plug-cable-load system completely resembles buck converter. This gives more space for improvement of the transient behavior when disconnecting the plug (load) from the system. Figure 3.9 illustrates simplified driving scheme, when the semiconductor switch, at the moment

when control pins are disconnected, does not simply turn off, but instead linearly decreases the duty cycle until reaches zero. The switching frequency used in this example was 50 kHz with the following circuit parameters:

$$r_{c1}=50\,m\Omega,\ L_{c1}=10\,\mu H,\ C_s=40\,\mu F,\ r_2=10\,m\Omega,\ L_{c2}=10\,\mu H,\\ R_L=26\,\Omega,\ C_L=10\,\mu F,\ L_L=30\,\mu H \tag{3.1}$$

The period from disconnect to the point when duty cycle reaches zero was 1ms. It can be noticed that this approach introduces the better dynamics of the voltage and current on the dc-bus side.

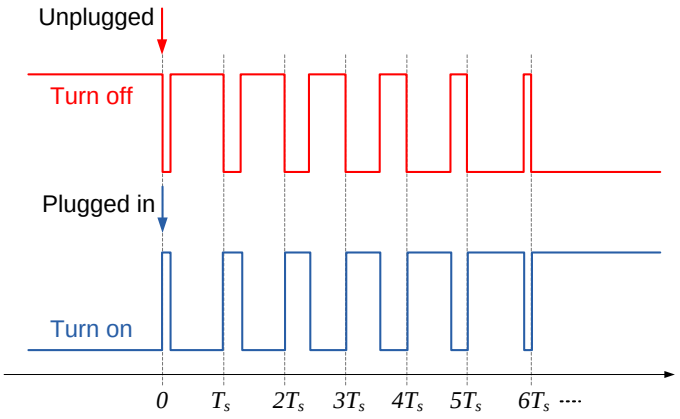

Figure 3.9: Cycled driving scheme when disconnecting and connecting the load

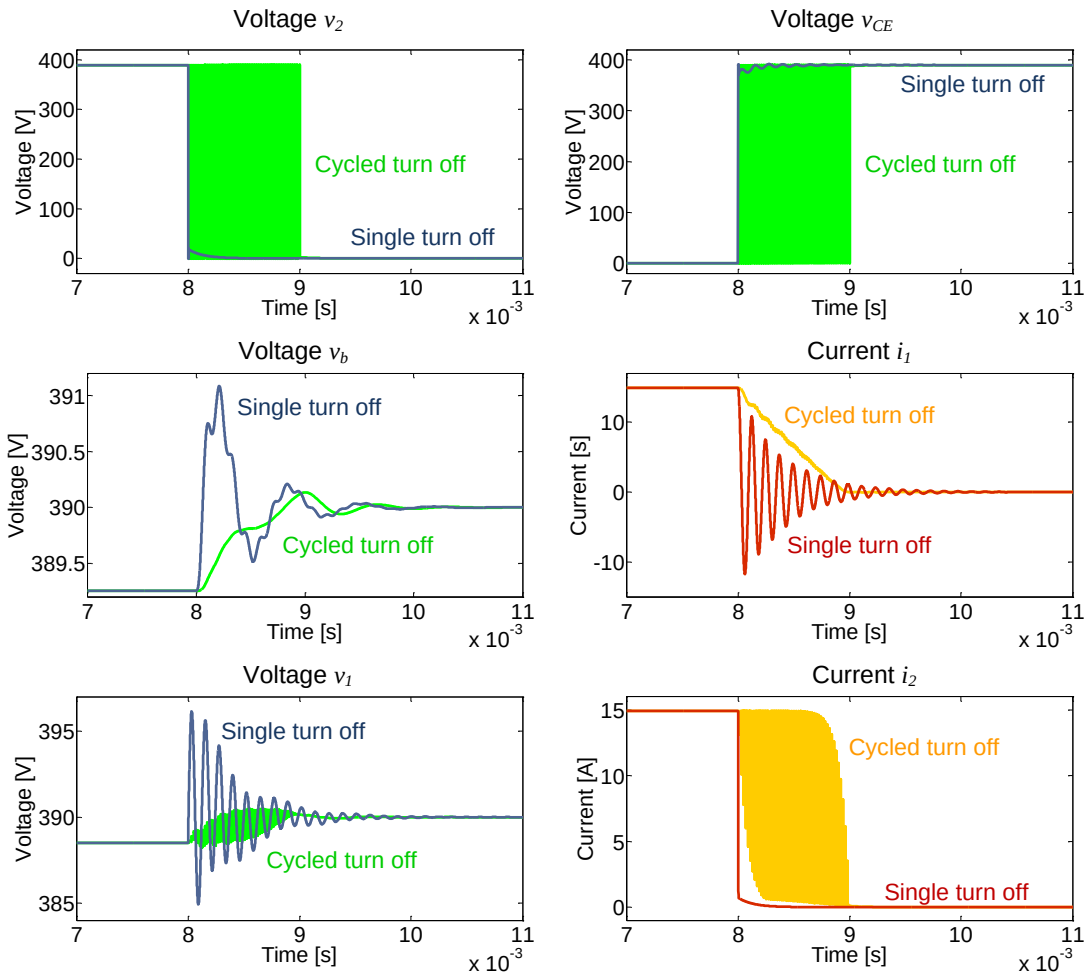

Figure 3.10: Transients as results of dc current interruption with added freewhlling diode D_s and he capacitor C_s (**blue**-voltage, **red**-current), and the transients when the cycled turn off is used (**green**-voltage and **orange**-current)

3.4. Static Operation of a DC Nanogrid

Although dc-nanogrid system features an advanced communication between the system components, desired is complete operational independence of these components. High level communication can immensely help in the system optimization and maximal utilization of the system sources in order to achieve zero-net annual energy requirements and cost, but does not force modes of operation, nor carry control feedback loop signals to the system components. Thus, each system source has a predefined V-I characteristics to follow in a wide operating range.

Figure 3.11 illustrates a dc-bus scheduling method [69-73], that will be used here for autonomous operation of each individual source.

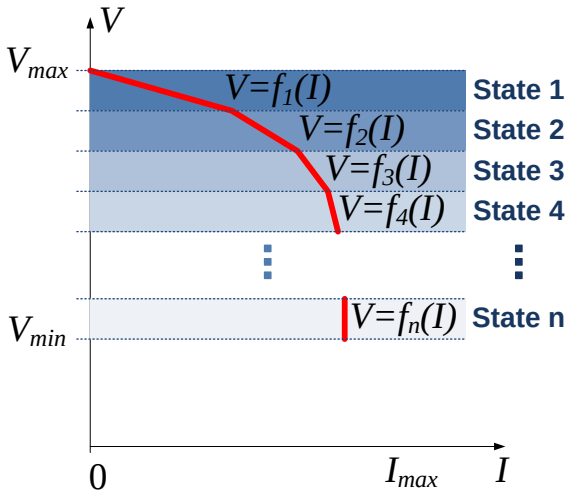

Figure 3.11: Dc-bus scheduling of the system sources

This methodology describes the static behavior of the source (any), within the safe operating range from V_{min} to V_{max} and from 0 to I_{max}. Source determines the mode of operation according to the voltage and current measured at its terminals. Thus, the system designer can assign an operating states or voltage level-ranges where the dc-nanogrid system can be under different operating conditions from V_{min} to V_{max}. Then, an individual V-I characteristics of the system sources can be designed according to desired operation, providing the full autonomy of each system source.

Although not still fully developed, dc standards for residential applications in some preliminary forms, and other, focused on the traction, telecom and industry dc distribution [74-76], suggest the maximum voltage drop on the dc line between source and the load to be not more than 2%. Dc systems, as above presented nanogrid, have distributed generation of the sources which in some modes of operation can work as a load (for example batter or PHEV converter when charging the battery), and determining the maximum voltage drop can be checked by exploring a numerous numbers of possibilities and combinations of the source/load components. As it will be shown later, maximum voltage drop can be enforced through the bus conductor's cross-section area.

The nominal voltage of the dc-nanogrid presented in this thesis is a 380 V (1 p.u.) with standard toleration of ±5%, and which gives a maximum allowable voltage drop on the dc-bus to be 2% or 7.6V between the furthest source and the load. This influences the width and the number of *states* for the dc-nanogrid scheduling shown in the Figure 3.11. For dc-nanogrid which is subject of discussion in this thesis, 2.5% of the nominal voltage is chosen as a width of each state which for the given range 380V±5% gives a total of four states in which the system can work safely. This is

shown in the following Figure 3.12.

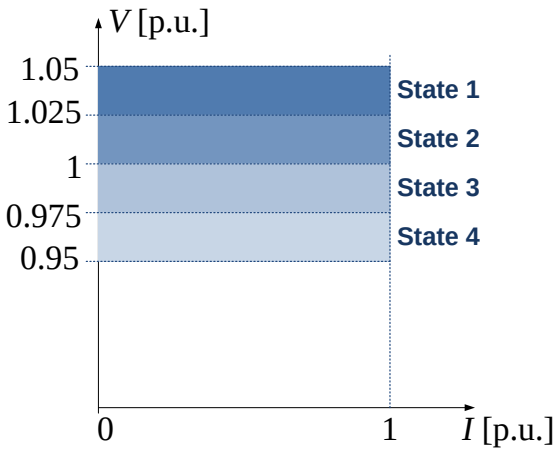

Figure 3.12: Dc-bus scheduling range for the system sources in the dc-nanogrid

The concept accepted for the voltage regulation in the nanogrid system is a droop control [77] based on the dc-bus signaling technique. Proposed droop control is non-dissipative, and the droop slope (virtual resistance) is control parameter. Individual droop characteristics, starting with the bidirectional grid interface converter will be shown below in this section.

A. Grid Interface Converter

The bidirectional droop (V-I) curve is shown in the Figure 3.13. In the first quadrant of the V-I plane this converter is taking energy from the grid while in the second is sourcing energy back to the grid according to the power system operator demands as shown in the Figure 3.4. The dotted line represents the amount of demanded current (power) for one, arbitrary chosen, demanded, value. The V axis intercept is chosen to be 1 [p.u.] which is the nominal bus voltage. From this point to the right the slope is constant up to the current limit of the converter. The "V-I knee" where the converter changes it mode of operation from DC voltage regulation mode to the DC current regulation mode is chosen to be 0.975 [p.u.] to allow for renewable sources to have the highest priority in the energy utilization sense. The parameter k_{sg} represents this converter's slope of the V-I curve.

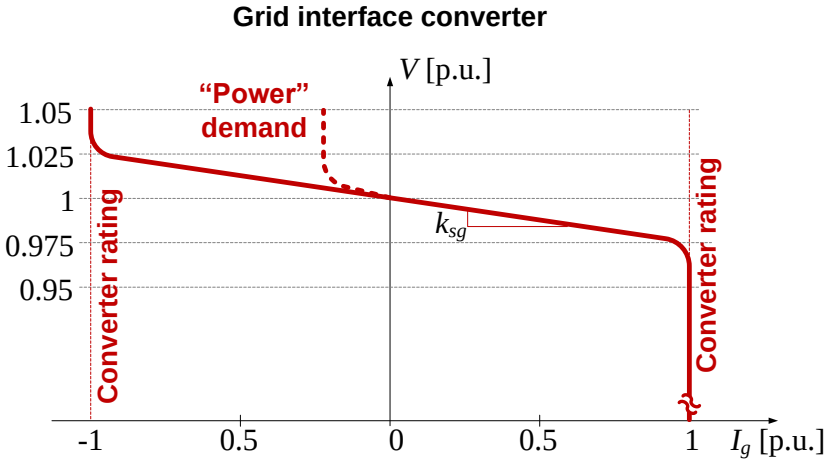

Figure 3.13: Static V-I (droop) curve of the grid interface converter

B. Solar Converter

The Solar converter's V-I characteristics is shown in the Figure 3.14, and as it can be noticed, dotted line presents the maximum converter capabilities, meaning that when the voltage at the converter terminals is in the range from 1.025 [p.u.] to 1.05 [p.u.], this converter operates in the voltage mode regulating the dc bus. Once it reaches the maximum power point, it continues to operate in the Maximum Power Point Tracking (MPPT) mode until the voltage is in the operating range. The actual MPPT curve will not always be the one shown as dotted line, but rather the solid one purely dependent on the available solar energy at the particular moment. It can be noticed that "V-I knee" in this case is not exactly at the 1.025 [p.u.] as chosen for the maximum capability curve, but slightly higher. This allows keeping the same, predefined droop slope of this converter in the higher voltage range, with parameter k_{ss} representing the slope of the V-I curve. Current limit is shown as the vertical gray line defines the converter absolute current rating.

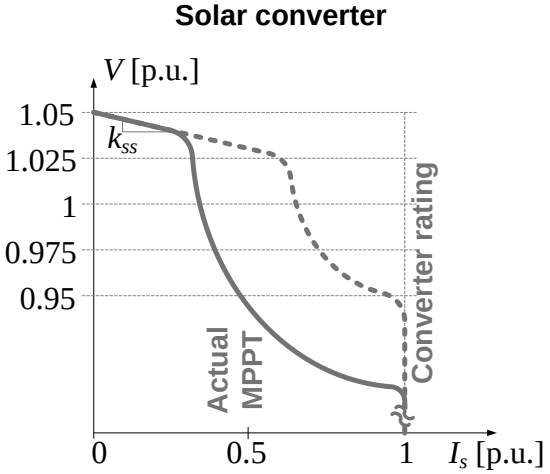

Figure 3.14: Static V-I (droop) curve of the solar converter

C. Wind Converter

The wind converter V-I curve is shown in the Figure 3.15. All that was said for the solar converter in the previous paragraph holds for this converter as well. Actual MPPT purely depends on the wind speed and can happen anywhere between the between zero converter output current and absolute current limit. The parameter k_{sw} represents this converter's slope of the V-I curve.

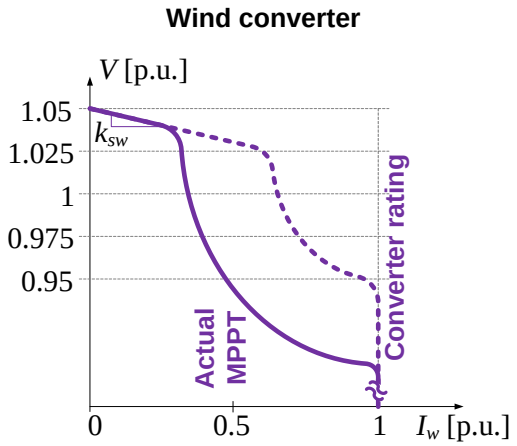

Figure 3.15: Static V-I (droop) curve of the wind converter

D. Energy Storage (battery) Converter

The converter for energy storage has slightly different properties then all previously explained converters in a sense of the droop characteristic adaptability. It is shown in the Figure 3.16. This curve can be anywhere within the shaded area called the operating range. The very right and very left vertical edge of this region represent the absolute capabilities of the converter itself. The operating region in the second quadrant of the V-I plane is purely determined with the State of Charge (SOC) of the battery. Coefficient k_{soc} represents the demand for charging if energy is available.

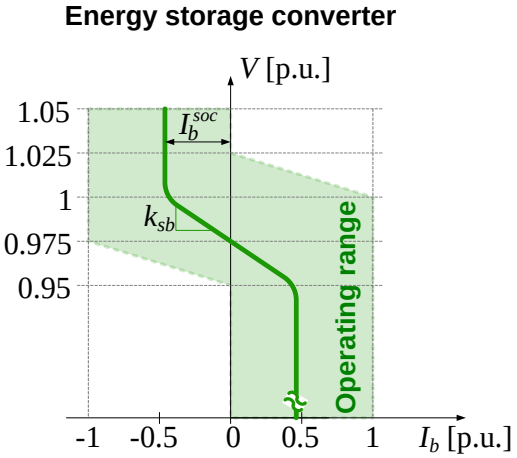

Figure 3.16: Static V-I (droop) curve of the battery converter

Battery converter receives information about the battery SOC from the battery monitoring system and sets the droop slope and the current limit accordingly in the second quadrant of the V-I plane. The droop characteristic in the first quadrant is set by the system control unit (ECC) according to the power management source utilization algorithm. This decision is made according to the instantaneous price of energy that system takes from the utility grid. The ECC has an information about the cost of the energy paid to charge the energy storage in the last charging cycle (and before), and can make a decision of the battery utilization accordingly. The converter then sets the slope of the droop characteristic in the first quadrant of the V-I plane, as well as the intercept point with the V-axis. Regardless of the cost of utilization, when the system bus voltage drops below 0.975 [p.u.], which represents the case when the demand in the system is high and all of the non-energy storage sources are exhausted (in the current limit), converter itself will move the droop characteristic lower to provide voltage regulation of the bus in the range of the 0.95 [p.u.] - 0.975 [p.u.]. If demand increases more and the bus voltage drops below the 0.95 [p.u.], system bus voltage may collapse knowing the fact that the majority of the loads in the system are Constant Power Loads (CPL). Programmable parameter k_{sb} represents the droop slope of this converter and the maximal current I_b^{soc} represents the charging current demand from the converter when energy for charging is available.

E. Plug-in Hybrid Electric Vehicle (PHEV) Converter

The PHEV converter has absolutely the same properties as previously explained static battery converter when the car is connected to the system. Its V-I curve is shown in the Figure 3.17 with the droop slope defined with the programmable parameter k_{sp}. Parameter I_p^{soc} is, similarly as above in the energy storage converter case, the maximal charging current demand when the energy is available. If charging of the battery is needed, the user can overwrite this V-I characteristics with the forced charging, by simply choosing that option in the ECC.

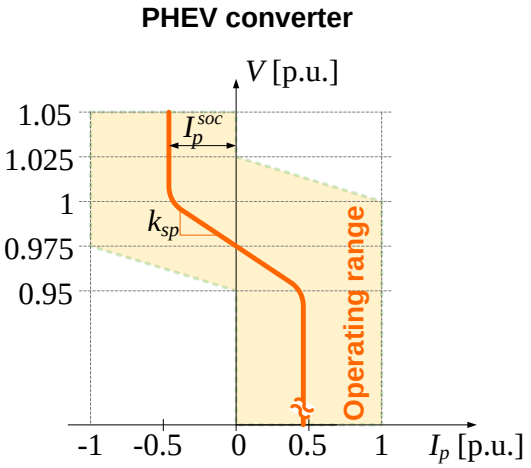

Figure 3.17: Static V-I (droop) curve of the PHEV converter

As seen above, in order to establish an autonomous nanogrid system, each component, particularly source converters, has to behave (statically) in the certain way described above from *A* to *E*.

Figure 3.18 shows a complete nanogrid system (source side) with corresponding V-I characteristic. For easier understanding and analysis of the system, two main assumptions will be made:

- All sources and loads share the same bus voltage. In other words, bus or cable impedance between the system components will be considered zero. Although here not specifically proven, this assumption is not far away from true in the practical system.
- At any operating point system has to maintain an equilibrium between energy production and consumption, and the total load current will be represented by the sum of all load currents:

$$I_l = \sum_{i=1}^{n} I_{li} = I_{l1} + I_{l2} + I_{l3} + ... + I_{\ln} \tag{3.2}$$

thus satisfying the following relationship:

$$I_l = I_g + I_s + I_w + I_b + I_p \tag{3.3}$$

Also, for better perception and easier understanding, the voltage level will be shown in volts [V] rather than *per unit* [p.u.] system.

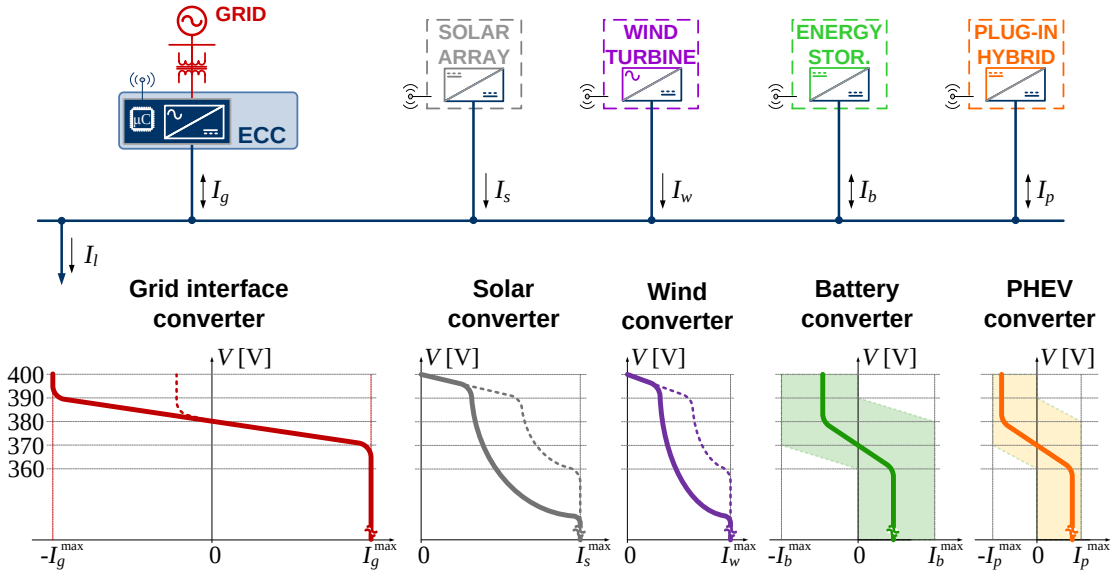

Figure 3.18: Static operation of the nanogrid system

Figure 3.18 also clearly shows the unidirectional and bidirectional nature of the sources by direction of the converter's output currents and utilization of the second quadrant of their V-I planes.

Although simple on the first look, it is very hard to perform static analysis of the whole system shown in the Figure 3.18, thus for simplicity, the two representative cases of the nanogrid operation are shown below comprising two sources and an equivalent load. First example is shown in the Figure 3.19. System comprised of the grid interface converter with the source current I_g , the solar converter with the source current I_s, and one equivalent load, I_l will be examined in this example.

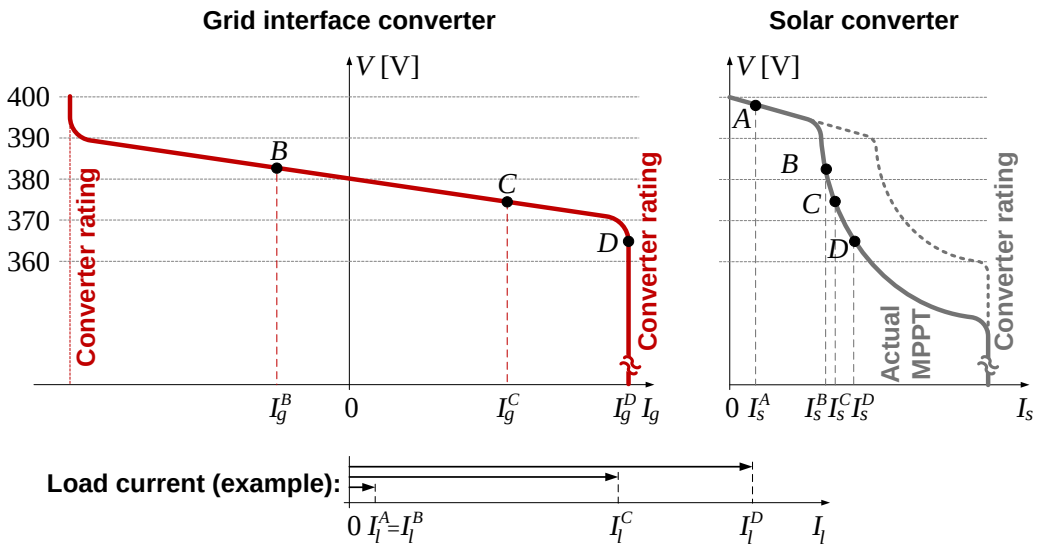

Figure 3.19: Qualitative characteristics of two sources for the nanogrid system operation example I

For the start, it will be assumed that the grid is not present, and the system comprised of only solar and the load, works in the islanded mode with negligible change in the solar irradiation. If the load demand is small, as current I_l^A in Figure 3.19 shows, the solar converter alone provides the current equilibrium, $I_l^A = I_l^B$, and regulates the bus voltage to slightly below 400 V (point *A* in Figure 3.19 – solar V-I curve).

Now, assuming that the load does not change, but the nanogrid is reconnected to the utility grid through the grid interface converter, the new equilibrium point moves to *B* in Figure 3.19 at the voltage slightly higher than 380 V, where the solar converter now operates in the MPPT mode, and the grid converter regulates the bus. Power equilibrium in this point clearly shows that the amount of energy produced by the solar converter is enough not only to fulfill the load requirement, but also to feed some energy back to the grid. Mathematically, this can be represented as:

$$I_g^B = I_l^B - I_s^B \tag{3.4}$$

Where I_g becomes negative and is fed back to the utility. When the load current is increased to a much higher level, I_l^C, and system moves to a new equilibrium at the bus voltage between 370 V and 380 V (point *C* in Figure 3.19), where the grid interface converter now takes most of the energy from utility grid. Solar converter output current changes only slightly due to the fact that it operates in the MPPT mode with the high output impedance.

If the load is eventually increased even more, the system can be forced to the point *D* in Figure 3.19, at the bus voltage below 370 V. At this point both sources operate in high output impedance modes (current limiting and MPPT), which is usually unstable because the voltage will decrease further with even a slight increase of the load current (especially when dealing with the Constant Power Load (CPL)), and consequently source converters will go offline after the bus voltage drops below 360 V level.

Another example illustrated in the Figure 3.20 shows the optimization of the nanogrid operation with the help of ECC.

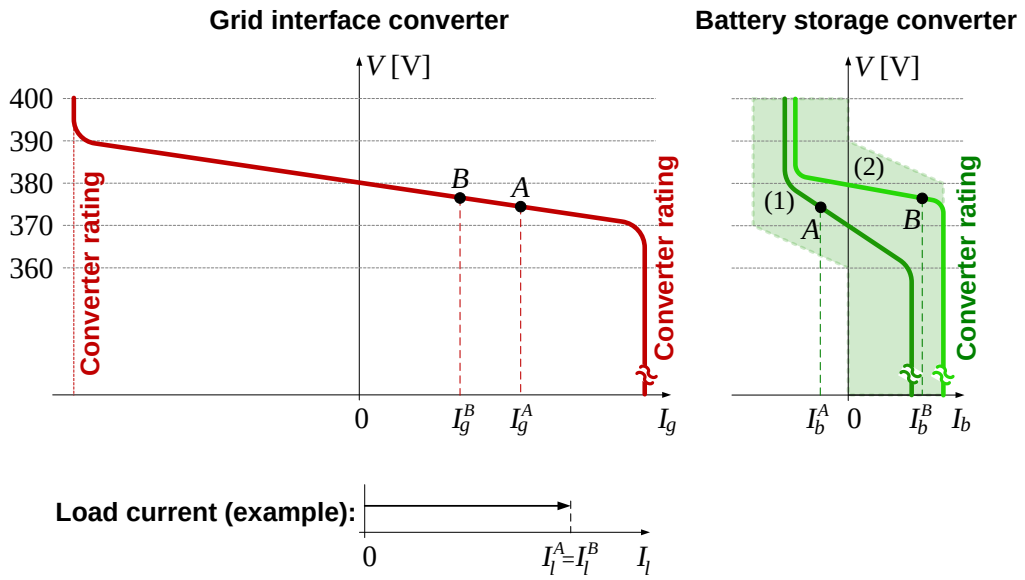

Figure 3.20: Qualitative characteristics of the two sources for the nanogrid system operation example II

System comprised of the grid interface converter with the source current I_g , the battery converter with the source current I_b, and one equivalent load I_l will be examined.

Let's assume that in this example load does not change at all during the time when optimization takes place. By having the load current I_l^A constant, an equilibrium operating point *A* is established in the system, where grid interface converter not only completely satisfies the load requirement, but also charges the energy storage battery. However, the ECC which is an inherent part of the grid interface converter, obtains an information about the energy cost at that particular hour (real time pricing) from the internet, and since the charging history of the batteries shows that in the previous charging cycle, for example, batteries were charged by using the wind energy overnight when no big load requirement was put on the system it (ECC) decides to make a cheaper utilization of the energy storage. In the other words, ECC checks the price of the energy on-line, and instead of drawing current I_g^A from the grid with the price P^A, it recalculates that the best utilization of the energy storage and the grid interface converter will be in the point *B*, it send the command to the battery converter how to set the V-I curve and established a new equilibrium point in *B*. The new equilibrium point has a slightly higher bus voltage level, but a big difference in the amount of energy taken from the grid, and as a consequence much lower cost.

The examples above showed a simple static operation of the nanogid system and one of the possible optimization schemes of the system, as the big step towards the

annual zero-net energy requirement and cost. The full static operation, as well as optimization of the nanogrid system is still in the research phase and is expected to be completed soon as the result of the future work on this, interesting topic.

Chapter 4. MODELING AND OPERATION OF A DC NANOGRID

Analysis of the whole dc-nanogrid system with all components is a very complex and difficult task. For the simpler analysis, a sample system - minimal relevant structure of the nanogrid comprising grid interface and solar converter on the source side, interconnection impedance representing wires, and two bus converters with appropriate loads, is chosen to represent nanogrid system for the purpose of exploring more deeply an operation, protection and system stability.
Sample system is shown in the figure 4.1.

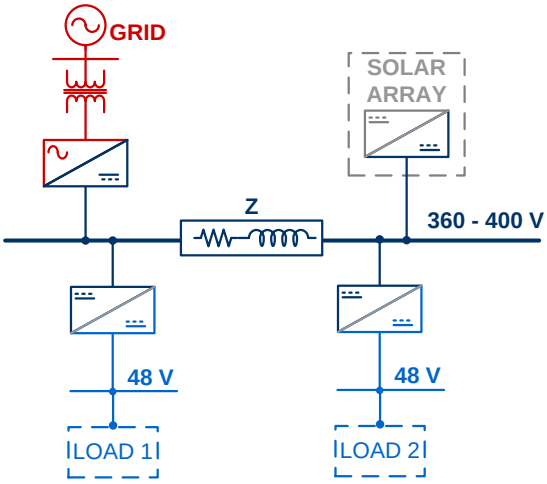

Figure 4.1: Minimal relevant structure (sample system) of the dc-nanogrid system

4.1. Average Model

The large-signal average model of the sample system made for the purpose of conducting the large-signal time domain and small-signal frequency domain simulations is illustrated in the Figure 4.2..

The source converters from the Figure 4.2 are both modeled as dc-dc buck converters with the voltage and current loop closed, and the same circuit and control parameters are used for both converters except for the non-linear part characteristic for the particular converter as defined earlier. The switching frequency was chosen to be 30 kHz for both source converters, and the bandwidths for the voltage and current loops were respectively 300Hz and 3kHz.

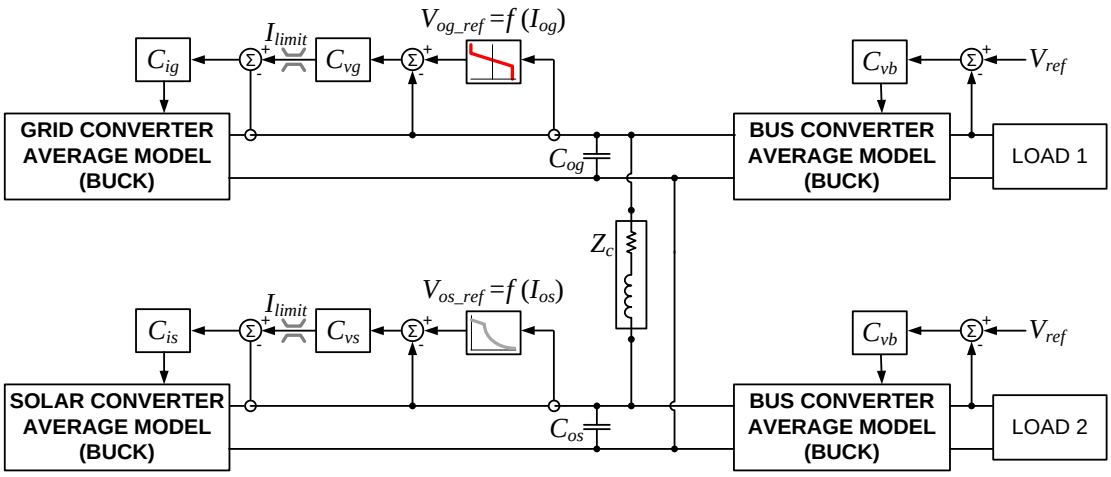

Figure 4.2: Average model used for the sample system analysis

Intermediate bus converters (380 V/48 V) were also modeled as buck converters with the switching frequency of 100 kHz and the bandwidth of the voltage loop around 8kHz. In simulations, they were loaded with resistors.

The non-linear relationships between the output currents and output voltages (4.1) are modeled as functions that describe corresponding part of the curves. As seen in the Figure 4.3, these parts are mostly linear functions with an exception of the hyperbolic function representing MPPT of the solar converter.

$$V_{og\_ref} = f(I_{og})$$
$$V_{os\_ref} = f(I_{os}) \tag{4.1}$$

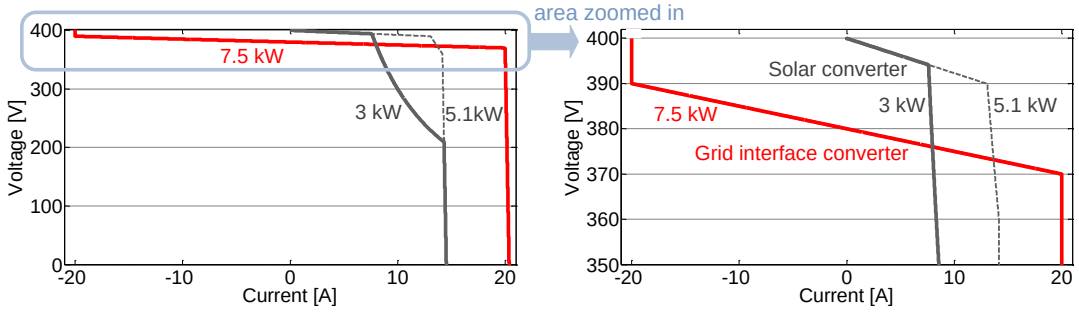

Figure 4.3: V-I characteristics of the grid interface and solar converter used in simulations

A. Load Change in the nanogrid

In this simulation, the behavior of the sources was shown when the load of the bus converters was changing in steps, and in order to avoid bus voltage collapse when source converters hit the current limit characteristic for the system loaded with CPL loads, the bus converters were simulated as an open-loop.

Figure 4.4 shows the result of that simulation showing transients in the nanogrid system.

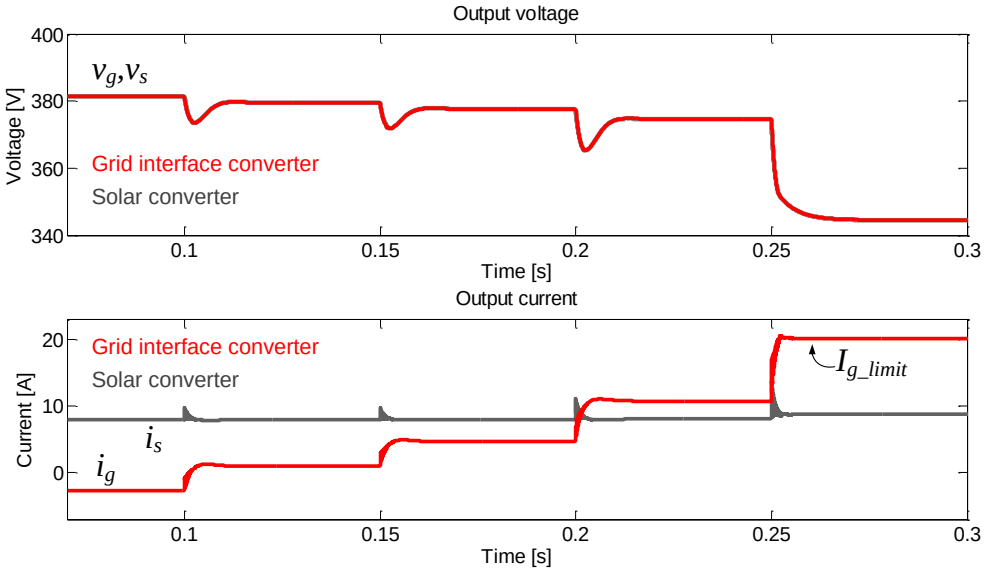

Figure 4.4: Time-domain response of the output voltages and output currents of source converters for the load change

It is clearly seen that statically values on the graph above completely agree with the values of the V-I curves plotted in 4.3. What is more, it is evident that in the period up to 0.1 [s] when the load was light, grid interface converter's current was negative, meaning that it was actually sourcing energy back to the grid. After 0.1 [s] the output current has been increasing in steps (according to the load steps) and the grid interface converter was taking energy from the grid. At the moment 0.25 [s], the grid interface converter output current hit the current limit. This as a consequence had a big voltage drop on the bus having the fact that another source, solar converter was in the current regulating mode with high output impedance that is practically considered current limit (as shown in the Figure 4.3 as a very steep slope of the solar V-I curve).

Solar converter steady-state current had a very small change in the whole operating range, which is also typical for the high output impedance current regulation mode.

As a consequence of two converters hitting the current limit, bus voltage went out of 360V-400V operating range of the nanogrid system and found a new operating point. In general, that would not have happened if the load behaved as CPL what is much more expected to be the case in the real, practical nanogrid systems. The bus voltage would then start collapsing until some of the protection in the system takes an appropriate action as it will be shown later in the thesis.

B. Stand-alone to grid-connected mode transition

This simulation simply shows the transient in the sample system when the solar converter works alone supplying the constant power load (regulated buck converters) but in the light load case when the solar converter still works in the voltage regulation mode. Stand alone operation would not be possible with the load being CPL and the solar converter working in the MPPT mode.

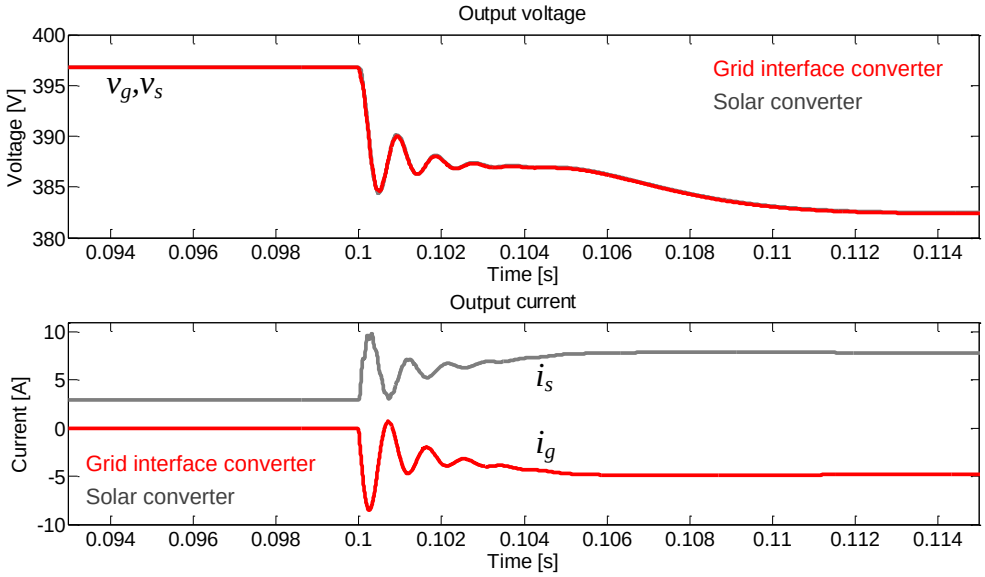

Figure 4.5: Time-domain response of the output voltages and output currents when the grid interface converter turns on

At the beginning of the simulation, as noticeable, the grid converter current was equal to zero, and the solar converter was supplying 1.2 kW load. The voltage on the bus, both points – one at the side of the grid interface connection and another at the side of solar converter connection, were around 397 V as illustrated in the Figure 4.5. Once the grid interface converter was turned on, an new equilibrium point was found at 383 V as an only solution to satisfy both V-I characteristics from the Figure 4.3. At that point, with an assumption that the load did not change during the transient, solar converter is in the MPPT mode having not only enough energy to supply the given load, but also to feed some of it back to the grid as evident in the Figure 4.5.

C. Autonomous load shedding in the dc-nanogrid system

Overload hierarchical protection in the nanogrid system can be assured by the source and the load components themselves, with no any external controller. This should prevent voltage on the bus to collapse when dealing with the CPL and all the sources are in the current regulation or current limit mode. This protection will be

disabled while the system bus voltage is in the operating range from 360 V - 400 V, and will trigger-on once the voltage starts decaying below the lower limit. For this functionality to be effective, the certain level of priority has to be assigned to the system components. Depending on the functionality and size of the nanogrid system, there can be more load priority levels. Figure 4.6 shows an autonomous load shedding feature applied on the dc-nanogrid sample system.

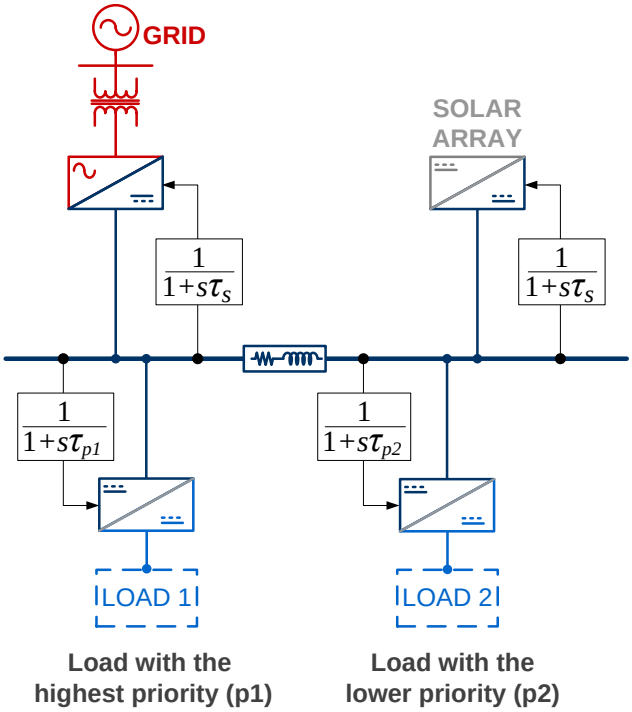

Figure 4.6: Illustration of the load shedding realization

As seen in an illustration above, every component from the system processes information about the voltage on the bus through the low-pass filter with the different time constant τ and the following relationship:

$$\tau_s > \tau_{p1} > \tau_{p2} > \ldots \tag{4.2}$$

where

τ_s is the time constant assigned to the low-pass filter for the system sources,

τ_{p1} is the time constant assigned to the low-pass filters for the highest priority loads and

τ_{p2} is the time constant assigned to the low-pass filter for the lover priority loads.

Figure 4.7 illustrates an above explained methodology. The red curve represents the reading of the bus voltage collapse when the system is overloaded with the constant power load. No filter is applied on this measurement. Then, the dark blue shows the bus voltage measurement when the filter with the smallest time constant is applied. This curve is assigned to the loads with the lowest priority, meaning that they will shut-off if the voltage crosses 360 V point, but not instantaneously when that happens, to avoid unnecessary load shedding when the transient on the bus voltage occurs and voltage undershoot goes below this point. If shedding of the lowest priority loads does not recover the system, then the next hierarchical level of loads is shed. Unsuccessful recovery would now lead to the definite source turn-off.

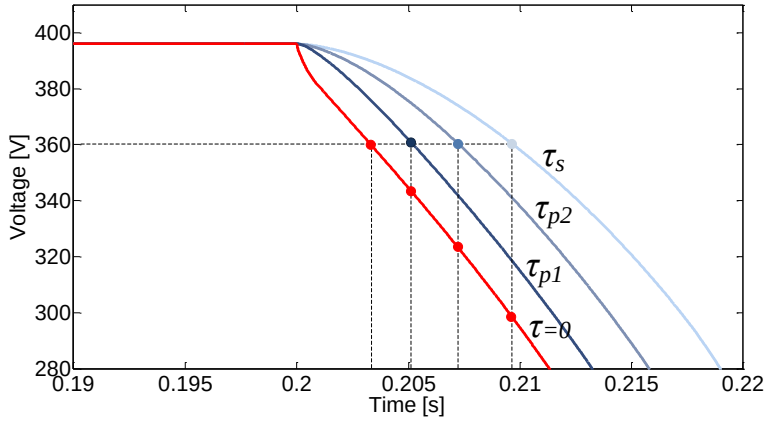

Figure 4.7: Bus voltage seen through the low-pass filters with different time constants

Figure 4.8 shows a successful system recovery of the bus voltage in the case when there is no hierarchical protection active (red colored curve) and when it is active (blue curve).

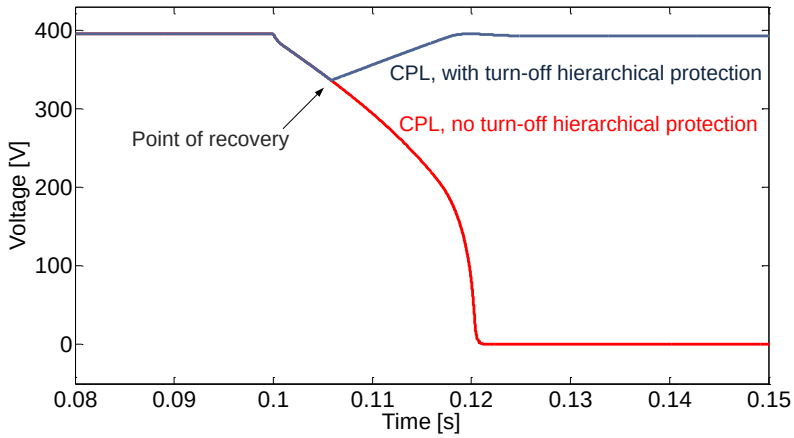

Figure 4.8: Bus voltage in the nanogrid system with and without hierarchical protection

D. Stability

This section will try to address the instability issue that could happen if the system is not designed carefully. The Figure below shows the situation when the connection of the source converters is done through the cables with non-negligible impedance (an example: 40m).

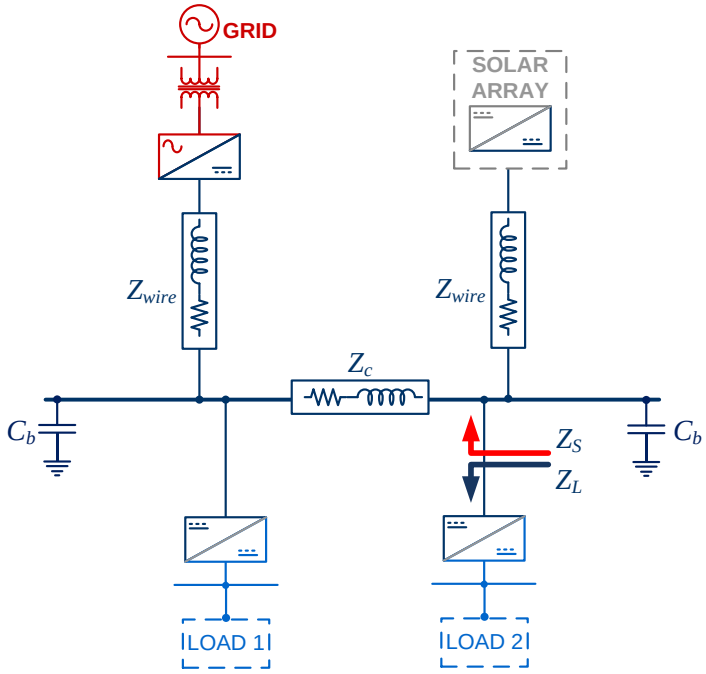

Figure 4.9: Sample system with the long wire added between the bus and the system sources

As mentioned in the Chapter 3, the distributed capacitance is envisioned to be very small to prevent big inrush current when the fault occurs on the bus, and unnecessary overdesigned system. Thus, the only capacitances on the bus were output capacitors of the two source converters 2x120μF in addition to the distributed bus capacitance C_b that was for this simulation 20 μF.

Figure 4.10 shows the time domain simulation of the system when case when the added impedance (wire) was:

$$L_{wire} = 45\mu\text{H},\ r_{wire} = 0.04\Omega \tag{4.3}$$

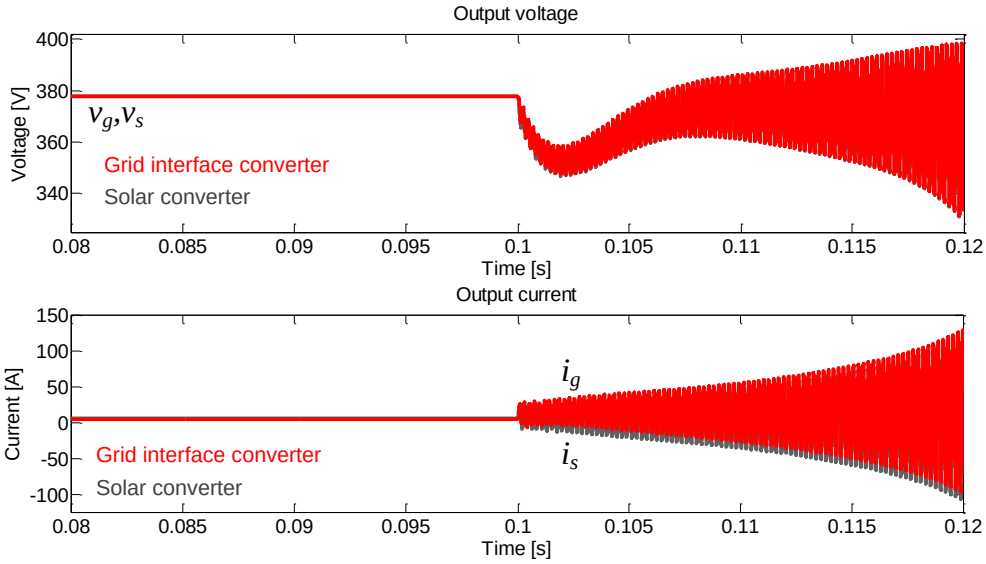

Figure 4.10: Instability when load step was applied

An evident instability occurred when the load step was applied. The Figure 4.11 shows measured output impedances in the operating point before the step was applied and oscillations occurred. It is obvious that there is an interaction between an equivalent source and the load since the source output impedance touches load output impedance at the point around 5 kHz.

The constant power nature of the load is evident by looking at the phase of the frequency response Z_L up to the 8kHz what corresponds to the voltage loop bandwidth of regulated buck converter.

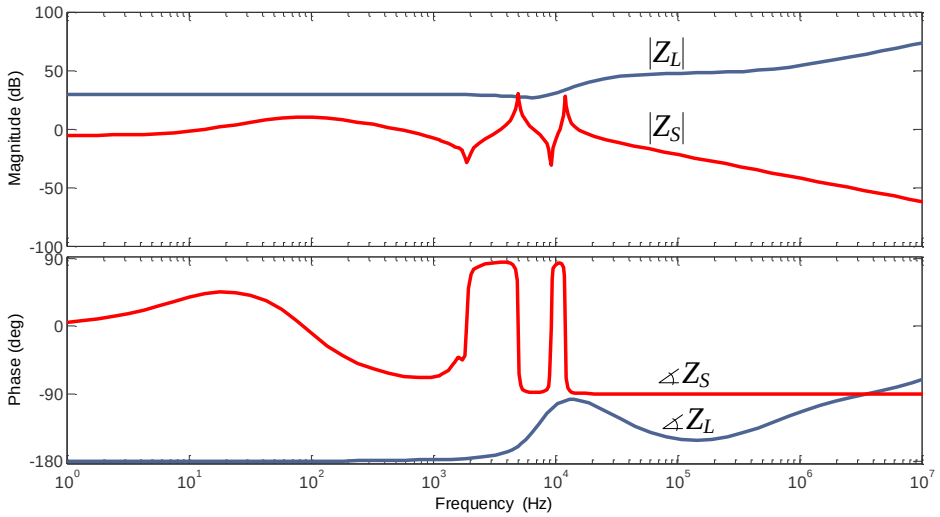

Figure 4.11: An equivalent source and load output impedance of the system measured at the point shown in the Figure 4.9.

The stability of the system in this case can be improved if distributed capacitance is increased. The following Figure 4.12 show the case when the capacitance C_b is increased from 20 μF to 100 μF.

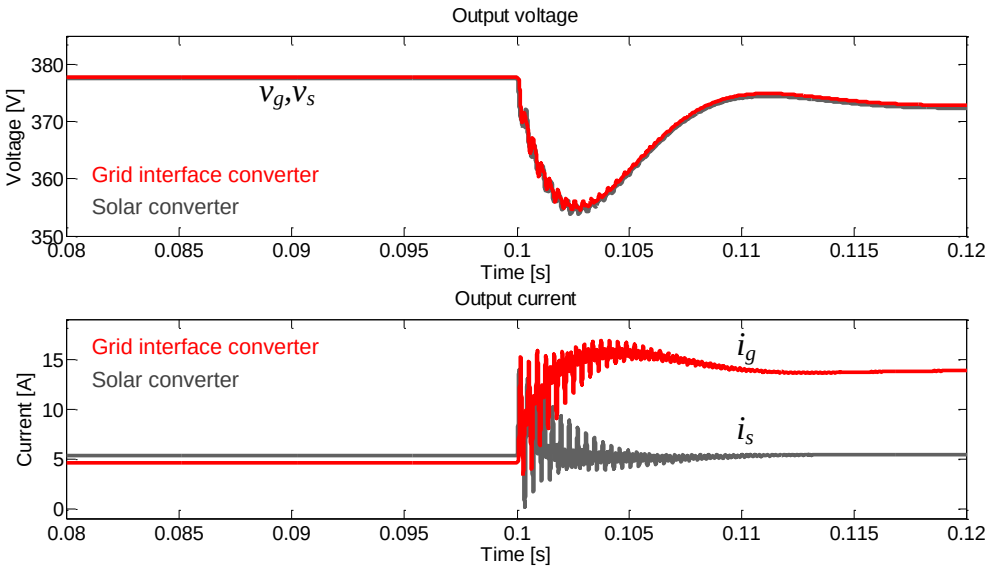

Figure 4.12: Time-domain simulation of the step response when bigger capacitance is added to the bus

Consequently, the system "anchored" with the bigger capacitors now becomes more stable as expected, and stability can also be proved by looking at the output impedances in the Figure 4.13.

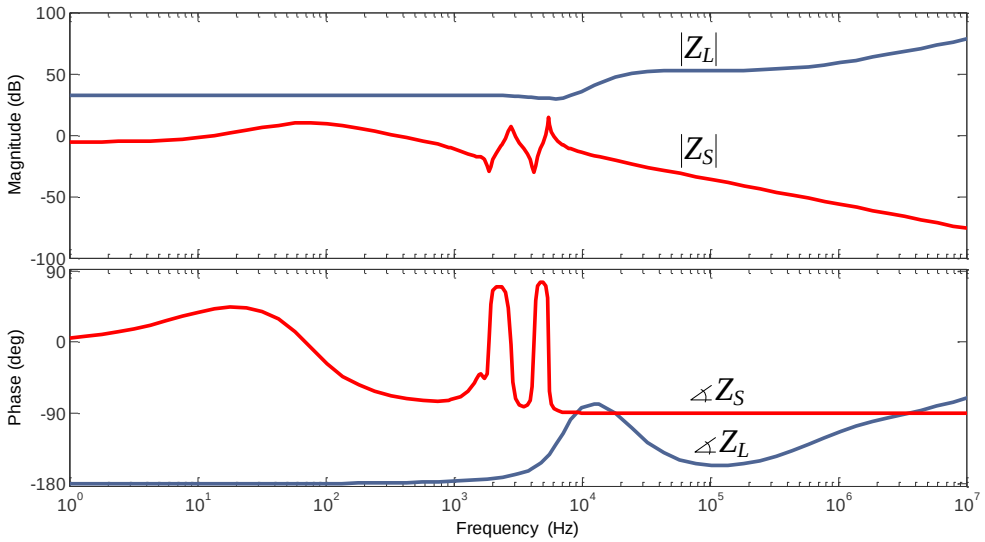

Figure 4.13: An equivalent source and load output impedance of the system measured at the point shown in the Figure 4.9.

As seen in a few examples above, the sample system offers a lot of opportunities for analysis of the system that is much more complex, as for instance, is the case with complete dc-nanogrid system. However, some of the system phenomena cannot be analyzed nor observed without inevitably increasing the model complexity as well as the number of components. These have always been an issues with the system level analysis and are still challenging.

On the other side, modeling and analyzing the system without being sure in the smallest details of control, circuit parameters and topology, interconnection impedance and others, is not meaningful at all, and could lead to completely wrong conclusions.

What is much more important, an analysis of the system that is in the design phase may be feasible, but trying to simulate and model an existing system is a big challenging task. Engineers would need to model components that they have some or none knowledge about their internal structure, control and topology.

As one of the solution that does not completely solve this problem, but address it in a practical and theoretical way is building the two-port network behavioral models presented in the next chapter.

Chapter 5. TERMINAL BEHAVIORAL MODELING

This modeling exploits the use of un-terminated two-port network model with inverse hybrid g-parameters shown in the Figure 5.1, as the generic model of the power electronics components with single, two wire input and output.

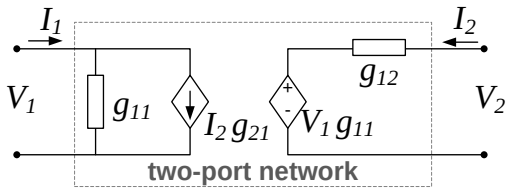

Figure 5.1: An inverse hybrid g-parameters two-port network

It can be written:

$$\begin{bmatrix} V_2 \\ I_1 \end{bmatrix} = \begin{bmatrix} g_{11} & g_{12} \\ g_{21} & g_{22} \end{bmatrix} \cdot \begin{bmatrix} V_1 \\ I_2 \end{bmatrix} \tag{5.1}$$

$$g_{11} = \left.\frac{V_2}{V_1}\right|_{I_2=0}, \; g_{12} = \left.\frac{V_2}{I_2}\right|_{V_1=0}, \; g_{21} = \left.\frac{I_1}{V_1}\right|_{I_2=0}, \; g_{22} = \left.\frac{I_1}{I_2}\right|_{V_1=0} \tag{5.2}$$

Two-port network can be directly used to build the small-signal linear model of the dc-dc converter around the particular operating point. Thus, as shown in the Figure 5.2, the four transfer functions can be defined: G_o - audio susceptibility, Z_o - output impedance, Y_i - input admittance and H_i - back current gain.

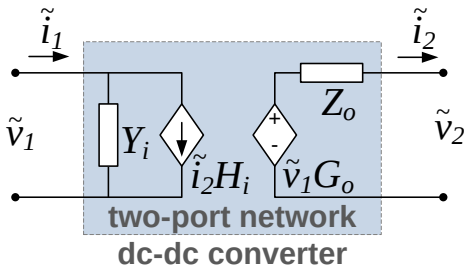

Figure 5.2: Small-signal model of the dc-dc converter in a two-port network representation

$$G_o(s)=\left.\frac{\tilde{v}_2}{\tilde{v}_1}\right|_{i_2=0},\quad Z_o(s)=\left.\frac{\tilde{v}_2}{\tilde{i}_2}\right|_{v_1=0},\quad Y_i(s)=\left.\frac{\tilde{i}_1}{\tilde{v}_1}\right|_{i_2=0},\quad H_i(s)=\left.\frac{\tilde{i}_1}{\tilde{i}_2}\right|_{v_1=0} \tag{5.3}$$

Having this, a small-signal two-port network model of the dc-dc converters becomes:

$$\begin{bmatrix}\tilde{v}_2\\ \tilde{i}_1\end{bmatrix}=\begin{bmatrix}G_o(s) & -Z_o(s)\\ Y_i(s) & H_i(s)\end{bmatrix}\cdot\begin{bmatrix}\tilde{v}_1\\ \tilde{i}_2\end{bmatrix} \tag{5.4}$$

where input small-signal components are $\tilde{v}_1$, $\tilde{i}_2$ and output $\tilde{v}_2$, $\tilde{i}_1$.

Minus sign in the (5.4) mathematically takes into an account direction of the output current as shown in the Figure 5.2, which corresponds to the natural power flow from input towards the output. Linearization of dc-dc converters around an operating point in order to capture their dynamics is widely accepted procedure when the goal is obtaining the dynamic behavior of linear or "mildly" non-linear converters as shown in the Figure 5.3 where the linearization around an arbitrary dc-operating point (*I*,*V*) is shown along with the small signal ac variations $\tilde{i}$ and $\tilde{v}$.

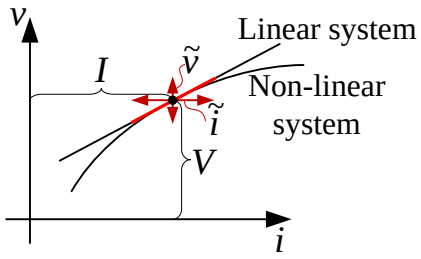

Figure 5.3: An example of linearization around an arbitrary operating point representation

Procedure unfortunately does not give a very good result when converters are highly non-linear, and cannot predict behavior in the whole operating range as it can with the linear ones. However, there is a need in practice to obtain the dynamics in the region "not too far" from an operating point in order to check small-signal stability and subsystem interaction of the cascaded converters and/or input output filters. Then,

linearized model can give meaningful results even with the non-linear converters as it will be shown later in this thesis.

To expand the system (5.4) to a model where input and output variables consist of *ac* small-signal variation and *dc* operating point, and which is, in practice, more meaningful model since these quantities can be directly measured in the time domain, it can be written:

$$\begin{bmatrix} v_2 \\ i_1 \end{bmatrix} = \begin{bmatrix} V_2 + \tilde{v}_2 \\ I_1 + \tilde{i}_1 \end{bmatrix} \text{ and } \begin{bmatrix} v_1 \\ i_2 \end{bmatrix} = \begin{bmatrix} V_1 + \tilde{v}_1 \\ I_2 + \tilde{i}_2 \end{bmatrix} \tag{5.5}$$

combining (5.4) and (5.5), it is obtained:

$$\begin{bmatrix} V_2 \\ I_1 \end{bmatrix} + \begin{bmatrix} \tilde{v}_2 \\ \tilde{i}_1 \end{bmatrix} = \begin{bmatrix} G_o(s) & -Z_o(s) \\ Y_i(s) & H_i(s) \end{bmatrix} \cdot \begin{bmatrix} \tilde{v}_1 \\ \tilde{i}_2 \end{bmatrix} + \begin{bmatrix} V_2 \\ I_1 \end{bmatrix} \tag{5.6}$$

and finally, low frequency two-port network model is:

$$\begin{bmatrix} v_2 \\ i_1 \end{bmatrix} = \begin{bmatrix} G_o(s) & -Z_o(s) \\ Y_i(s) & H_i(s) \end{bmatrix} \cdot \begin{bmatrix} v_1 - V_1 \\ i_2 - I_2 \end{bmatrix} + \begin{bmatrix} V_2 \\ I_1 \end{bmatrix} \tag{5.7}$$

The block diagram of the system from (5.7) and its equivalent circuit are respectively shown in the Figure 5.4 a) and b), representing the two-port network behavioral model of the dc-dc converter around an operating point defined with V_1,V_2, I_1 and I_2.

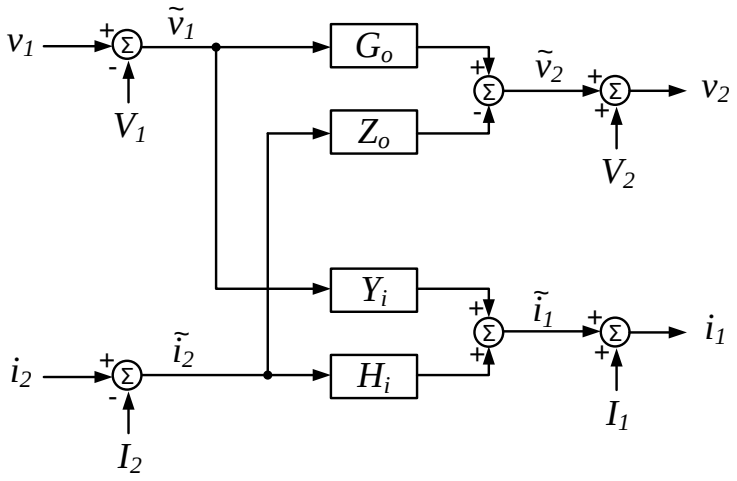

a)

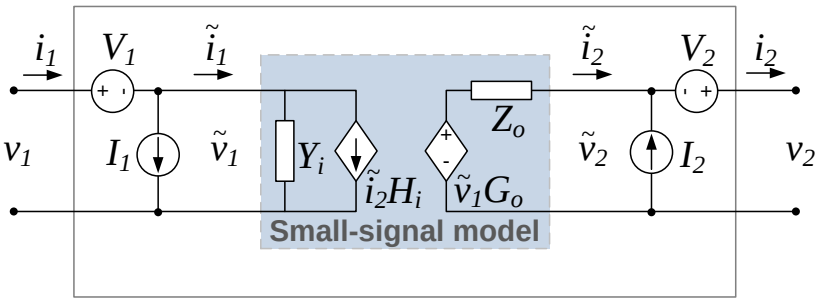

b)

Figure 5.4: a) Block diagram of a two-port network behavioral model of a dc-dc converter and b) Its equivalent circuit

5.1. Open- and Closed-loop Converter Model

As it has been shown in the past [78-80], the dynamics of a switched-mode converters, both open- and closed-loop can be represented by means of the four transfer functions shown in (5.3) and thus with the model derived and shown in the Figure 5.4. All four of the transfer functions have inherently embedded information about all the control loops closed within the converter as it will be shown in this section.

For this purpose, the model of the buck converter with the, for simplicity of analytical derivation, only voltage loop closed is shown in the Figure 5.5. Transfer functions that describe the behavior of this converter are:

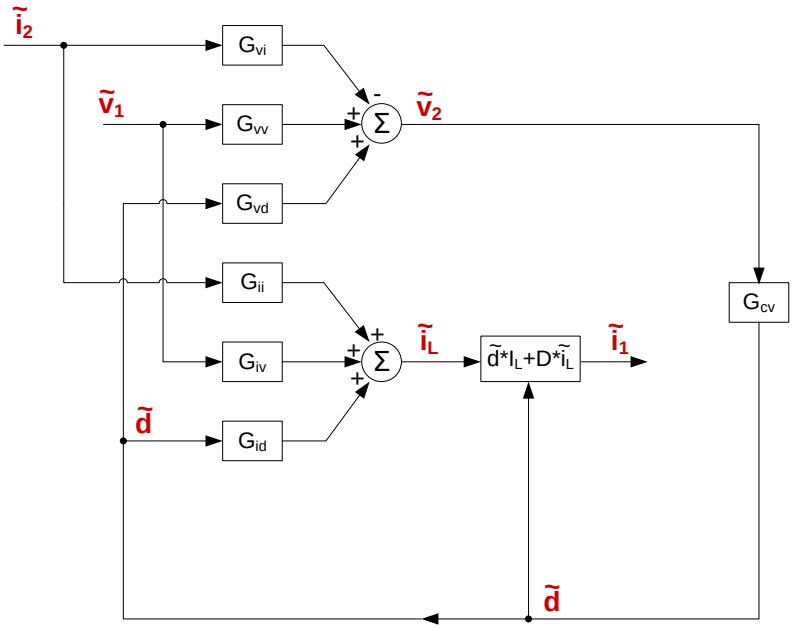

Figure 5.5: An equivalent small-signal model of the closed loop buck converter

G_{vi} – output current-to-output voltage
G_{vv} – input voltage-to-output voltage
G_{vd} – duty cycle-to-output voltage
G_{ii} – output current-to-inductor current
G_{iv} – input voltage-to-inductor current
G_{id} – duty cycle-to-inductor current
G_{cv} – voltage compensator
$T_v=G_{vd}G_{cv}$ – voltage loop gain

The small-signal expression $\tilde{i}_1 = \tilde{d}I_L + D\tilde{i}_L$, is a relationship between the averaged switch current (input current in buck converter if no input filter is placed) and the averaged inductor current at the quiescent operating point defined with D and I_L.
By analytically solving the system from Figure 5.5, open- and closed-loop transfer functions are obtained and shown in the (5.8) and (5.9) respectively.

$$\begin{bmatrix} G_{o\_OL}(s) & -Z_{o\_OL}(s) \\ Y_{i\_OL}(s) & H_{i\_OL}(s) \end{bmatrix} = \begin{bmatrix} G_{vv} & G_{vi} \\ DG_{iv} & DG_{ii} \end{bmatrix} \tag{5.8}$$

$$\begin{bmatrix} G_{o\_CL}(s) & -Z_{o\_CL}(s) \\ Y_{i\_CL}(s) & H_{i\_CL}(s) \end{bmatrix} = \begin{bmatrix} \dfrac{G_{vv}}{1+T_v} & \dfrac{G_{vi}}{1+T_v} \\ DG_{iv} - \dfrac{G_{cv}G_{vv}(DG_{id}+I_L)}{1+T_v} & DG_{ii} - \dfrac{G_{cv}G_{vi}(DG_{id}+I_L)}{1+T_v} \end{bmatrix} \tag{5.9}$$

It is clearly seen that four transfer functions from the terminal-behavioral model hold information of the voltage compensator and the loop gain, therefore the model from Figure 5.4 can be used for both open-and closed-loop converters as it will be verified and validated in some of the following sections.

5.2. Terminal identification of general behavioral model for dc-dc converters

Procedure for obtaining the terminal-behavioral model consists of two separate sets of measurements on the converter working at desired operating point, as shown in Figure 5.6. Although converter shown in this figure is regulated buck, it actually can be of any other topology, and in other words, an internal structure and parameters other than input voltage, output voltage and power rating, can be completely unknown to the user. Converter has to work in the preferred operating point and must stay at that operating point until all quantities are captured.

The goal is terminal identification of the internal dynamics represented by the four transfer functions (5.3) as shown in the previous section. These transfer functions must be “un-terminated” in order to fully characterize dynamics of the particular converter, which practically means that the source and load dynamics inherently present in any of the transfer functions when measured on-line, must be decoupled from them ensuring that converter, when put under different conditions in the simulations, will dynamically behave as expected.

Setup 1:

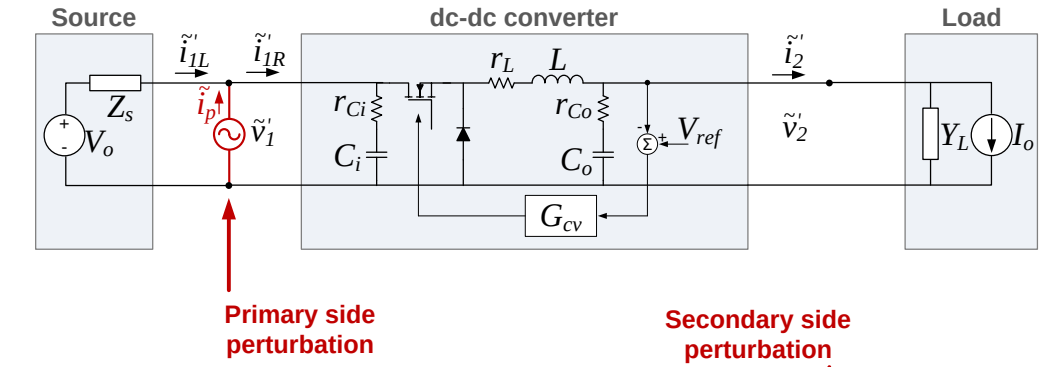

Setup 2:

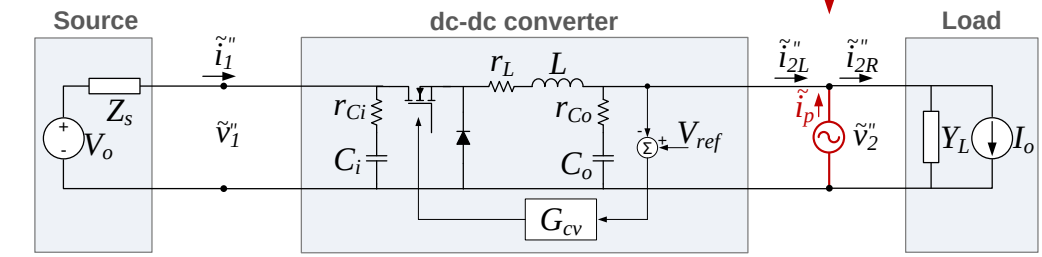

Figure 5.6: Measurement setup for terminal characterization of a dc-dc converter

The first set of transfer functions (audio-susceptibility and input admittance) can be obtained by perturbing the input side of the converter (ac sweep – setup 1 on the Figure 5.6) and is shown in the (5.10). The letter *m* in the index denotes measured quantities (terminated) and the superscript (‘)-primary denotes variables from the first setup.

$$G_{om}(s)=\frac{\tilde{v}_2'}{\tilde{v}_1'} \quad \text{and} \quad Y_{im}(s)=\frac{\tilde{i}_{1R}'}{\tilde{v}_1'} \tag{5.10}$$

The small-signal two-port network model that corresponds to the Figure 5.6 is:

$$\begin{bmatrix}\tilde{v}_2'\\ \tilde{i}_{1R}'\end{bmatrix}=\begin{bmatrix}G_o(s) & -Z_o(s)\\ Y_i(s) & H_i(s)\end{bmatrix}\cdot\begin{bmatrix}\tilde{v}_1'\\ \tilde{i}_2'\end{bmatrix} \tag{5.11}$$

Or

$$\begin{aligned}\tilde{v}_2' &= G_o(s)\cdot\tilde{v}_1' - Z_o(s)\cdot\tilde{i}_2'\\ \tilde{i}_{1R}' &= Y_i(s)\cdot\tilde{v}_1' + H_i(s)\cdot\tilde{i}_2'\end{aligned} \tag{5.12}$$

From (5.10) it can be written:

$$\begin{aligned}\tilde{v}_2' &= G_{om}(s)\cdot\tilde{v}_1'\\ \tilde{i}_{1R}' &= Y_{im}(s)\cdot\tilde{v}_1'\end{aligned} \tag{5.13}$$

Now combining (5.12) and (5.13), it is obtained:

$$\begin{aligned} G_{om}(s)\cdot\tilde{v}_1' &= G_o(s)\cdot\tilde{v}_1' - Z_o(s)\cdot\tilde{i}_2' \\ Y_{im}(s)\cdot\tilde{v}_1' &= Y_i(s)\cdot\tilde{v}_1' + H_i(s)\cdot\tilde{i}_2' \end{aligned} \tag{5.14}$$

which gives:

$$\begin{aligned} G_{om}(s) &= G_o(s) - Z_o(s)\cdot\frac{\tilde{i}_2'}{\tilde{v}_1'} \\ Y_{im}(s) &= Y_i(s) + H_i(s)\cdot\frac{\tilde{i}_2'}{\tilde{v}_1'} \end{aligned} \tag{5.15}$$

The last equations clearly shows a relationship between the terminated and un-terminated transfer functions, but also the common term $\tilde{i}_2' / \tilde{v}_1'$ that has dimension of conductance [S=1/Ω]. The new term called transconductance - $T_{gm}(s)$ can be now defined since represents the input voltage to output current transfer function so the equation (5.15) becomes:

$$\begin{aligned} G_{om}(s) &= G_o(s) - Z_o(s)\cdot T_{gm}(s) \\ Y_{im}(s) &= Y_i(s) + H_i(s)\cdot T_{gm}(s) \end{aligned} \tag{5.16}$$

The second set of transfer functions (output impedance and back-current gain) can be now obtained by perturbing the output side of the converter (ac sweep – setup 2 on the Figure 5.6) and is shown in the (5.17). Again, a letter *m* in the index denotes measured quantities, and the superscript (“)-second denotes variables from the second setup.

$$Z_{om}(s) = \frac{\tilde{v}_2''}{\tilde{i}_{2L}''} \text{ and } H_{im}(s) = \frac{\tilde{i}_1''}{\tilde{i}_{2L}''} \tag{5.17}$$

The small-signal two-port network model that corresponds to the Figure 5.6 is:

$$\begin{bmatrix} \tilde{v}_2'' \\ \tilde{i}_1'' \end{bmatrix} = \begin{bmatrix} G_o(s) & -Z_o(s) \\ Y_i(s) & H_i(s) \end{bmatrix} \cdot \begin{bmatrix} \tilde{v}_1'' \\ \tilde{i}_{2L}'' \end{bmatrix} \tag{5.18}$$

Or

$$\begin{aligned} \tilde{v}_2'' &= G_o(s)\cdot\tilde{v}_1'' - Z_o(s)\cdot\tilde{i}_{2L}'' \\ \tilde{i}_1'' &= Y_i(s)\cdot\tilde{v}_1'' + H_i(s)\cdot\tilde{i}_{2L}'' \end{aligned} \tag{5.19}$$

From (5.17) it can now be written:

$$\begin{aligned} \tilde{v}_2'' &= Z_{om}(s)\cdot \tilde{i}_{2L}'' \\ \tilde{i}_1'' &= H_{im}(s)\cdot \tilde{i}_{2L}'' \end{aligned} \tag{5.20}$$

Now combining (5.19) and (5.20), it is obtained:

$$\begin{aligned} Z_{om}(s)\cdot \tilde{i}_{2L}'' &= G_o(s)\cdot \tilde{v}_1'' - Z_o(s)\cdot \tilde{i}_{2L}'' \\ H_{im}(s)\cdot \tilde{i}_{2L}'' &= Y_i(s)\cdot \tilde{v}_1'' + H_i(s)\cdot \tilde{i}_{2L}'' \end{aligned} \tag{5.21}$$

Which gives:

$$\begin{aligned} Z_{om}(s) &= G_o(s)\cdot \frac{\tilde{v}_1''}{\tilde{i}_{2L}''} - Z_o(s) \\ H_{im}(s) &= Y_i(s)\cdot \frac{\tilde{v}_1''}{\tilde{i}_{2L}''} + H_i(s) \end{aligned} \tag{5.22}$$

The last equations again shows relationship between the terminated and un-terminated transfer functions and the common term $\tilde{v}_1'' / \tilde{i}_{2L}''$ that now has dimension of resistance [Ω]. The new term called transresistance – $T_{rm}(s)$ can be now defined and represents the output current to input voltage transfer function. The equation (5.22) becomes:

$$\begin{aligned} Z_{om}(s) &= G_o(s)\cdot T_{rm}(s) - Z_o(s) \\ H_{im}(s) &= Y_i(s)\cdot T_{rm}(s) + H_i(s) \end{aligned} \tag{5.23}$$

By representing (5.16) and (5.23) with the matrix form, it is obtained:

$$\begin{bmatrix} G_{om} \\ Y_{im} \\ Z_{om} \\ H_{im} \end{bmatrix} = \begin{bmatrix} 1 & 0 & -T_{gm} & 0 \\ 0 & 1 & 0 & T_{gm} \\ T_{rm} & 0 & -1 & 0 \\ 0 & T_{rm} & 0 & 1 \end{bmatrix} \cdot \begin{bmatrix} G_o \\ Y_i \\ Z_o \\ H_i \end{bmatrix} \tag{5.24}$$

Finally, the decoupling matrix can be defined as an inverse of the (5.24) allowing the un-terminated transfer functions to be obtained directly and linearly from the measured – terminated ones. The decoupling matrix is shown in the (5.25).

$$\begin{bmatrix} G_o \\ Y_i \\ Z_o \\ H_i \end{bmatrix} = \frac{1}{1-T_{gm}T_{rm}} \begin{bmatrix} 1 & 0 & -T_{gm} & 0 \\ 0 & 1 & 0 & -T_{gm} \\ T_{rm} & 0 & -1 & 0 \\ 0 & -T_{rm} & 0 & 1 \end{bmatrix} \cdot \begin{bmatrix} G_{om} \\ Y_{im} \\ Z_{om} \\ H_{im} \end{bmatrix} \tag{5.25}$$

In order to verify decoupling procedure and prove matrix (5.25), circuit shown in the Figure 5.7 will be used with all parameters shown in the same figure. Following the procedure previously explained at the beginning of this section, two different ac-sweeps (primary and secondary side perturbation) were performed and six transfer functions were obtained (G_{om} – audio-susceptibility, Y_{im} – input admittance, T_{gm} – transconductance, Z_{om} – output impedance, H_{im} – back-current gain and T_{rm} – transresistance). These transfer functions are shown in the Figure 5.8 colored in blue. By directly applying (5.25), un-terminated transfer functions were obtained and are shown in the same figure colored in red. It is clearly seen that the influence of the source and load dynamic is big and the measured, terminated transfer functions are strongly coupled to the source and load (their transfer functions are shown in the Figure 5.9). Also, by looking at the Figure 5.7, it is obvious that buck converter model used for verification purposes is a simple second order system and the blue, measured characteristics are definitely not describing the converter behavior correctly. In order to prove that the red characteristics describe the converter behavior well, the four un-terminated transfer functions of the converter from 5.7 are derived analytically and their expressions are shown in the (5.26).

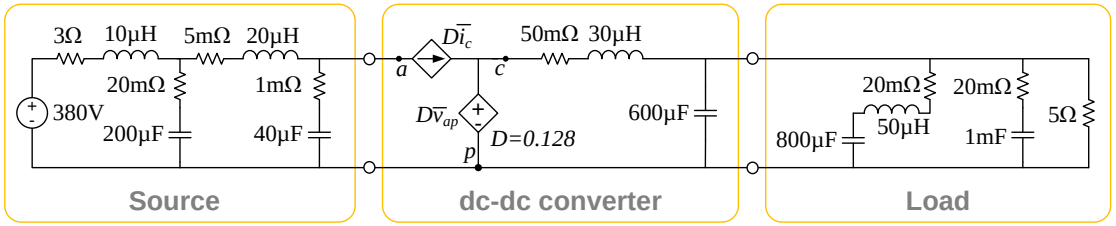

Figure 5.7: Source - dc-dc converter – load system used for verification of (5.25)

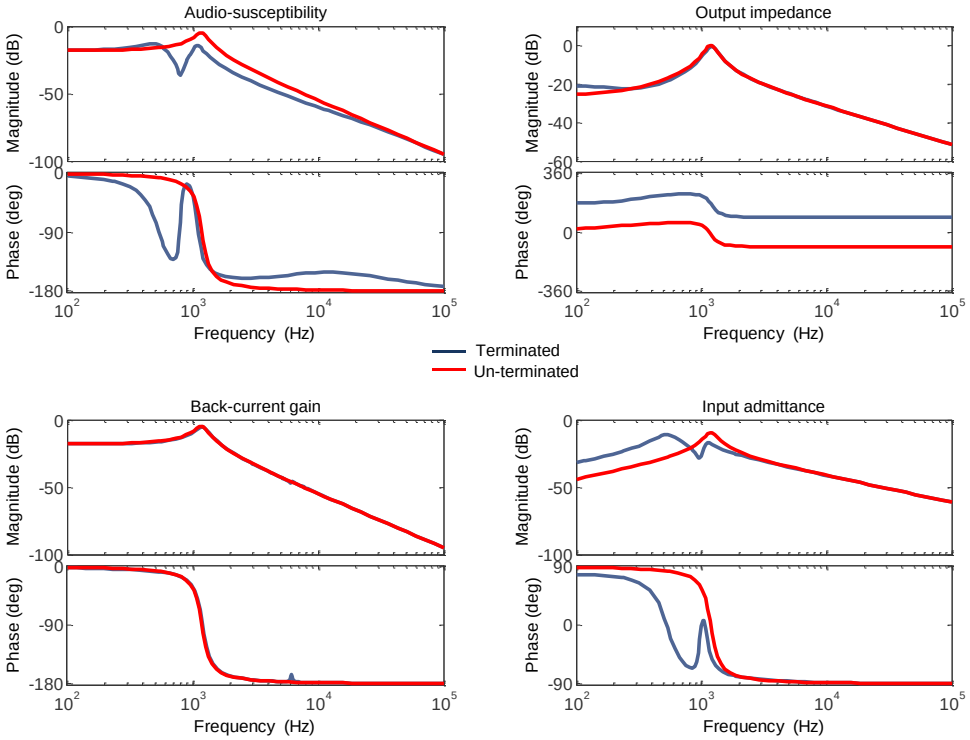

Figure 5.8: **Terminated** and **un-terminated** transfer functions of the converter from Figure 5.7

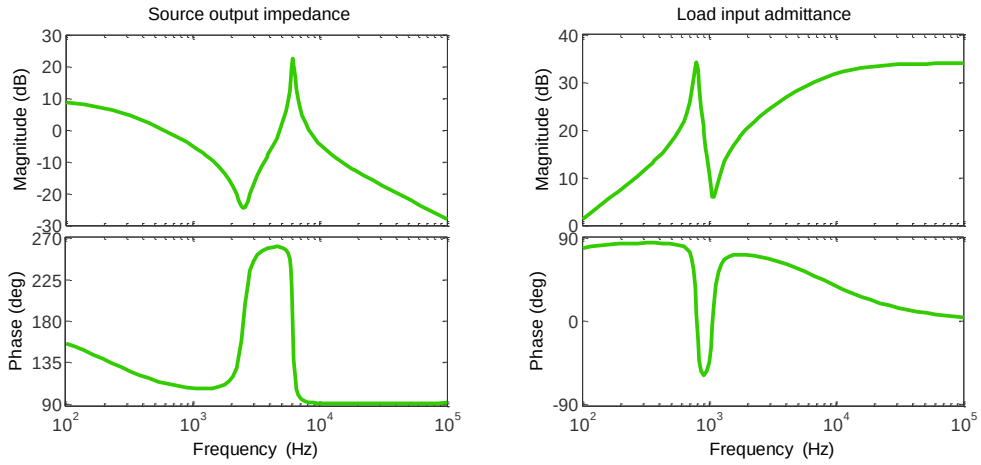

Figure 5.9: Source output impedance and load input admittance of the system shown in the Figure 5.7

$$
\begin{aligned}
G_{oa} &= \frac{D}{1+Cr_L s+CLs^2} \\
Y_{ia} &= \frac{CD^2 s}{1+Cr_L s+CLs^2} \\
Z_{oa} &= \frac{r_L+Ls}{1+Cr_L s+CLs^2} \\
H_{ia} &= \frac{D}{1+Cr_L s+CLs^2}
\end{aligned}
\tag{5.26}
$$

The figure 5.10 shows the comparison between the transfer functions analytically obtained (gray, dashed curves) and the ones obtained from decoupling procedure (colored in red). Perfect matching was achieved which proves the effectiveness of the decoupling procedure by applying the linear transformation (5.25).

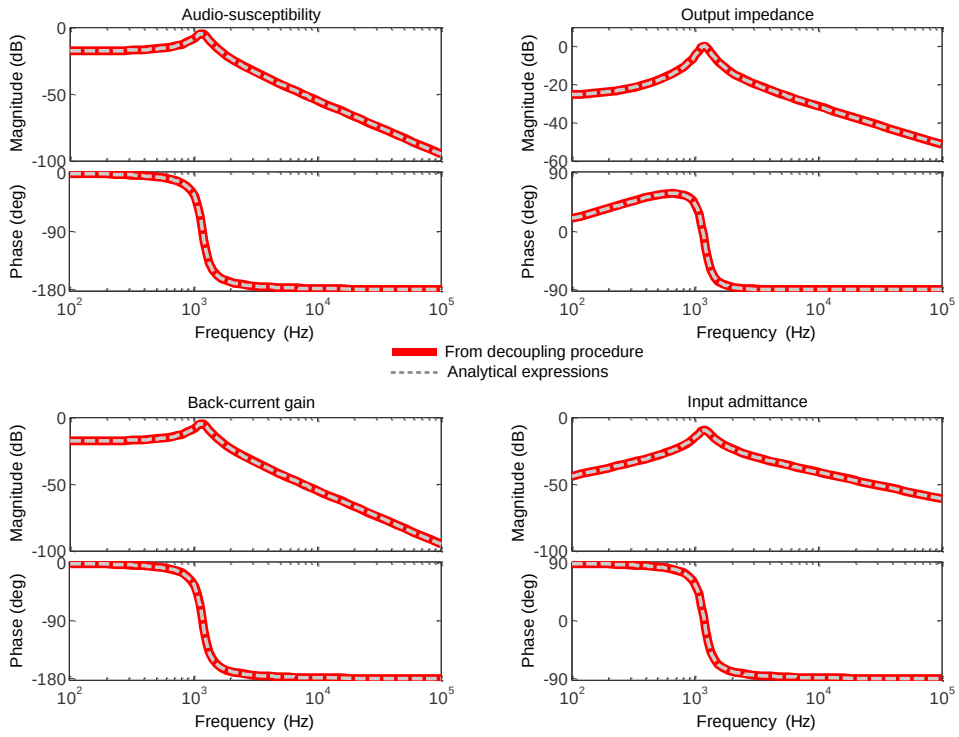

Figure 5.10: **Analytical** and **decoupled** transfer functions

5.3. Verification of the terminal behavioral modeling with the regulated buck and regulated boost converter

Terminal behavioral modeling will be verified in simulation with the regulated buck converter shown in the figure 5.11. Both current and voltage loops are closed and the compensator parameters are given in this figure along with all the other circuit parameters.

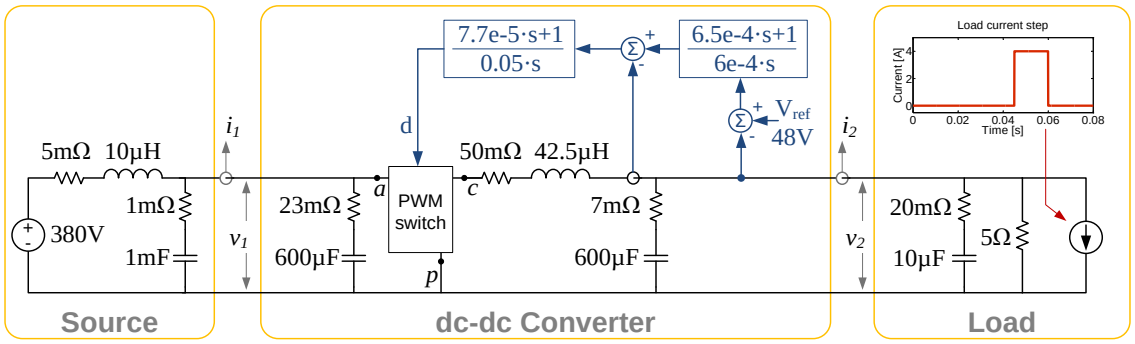

Figure 5.11: Regulated buck converter

Before the ac sweep was performed, the system from Figure 5.11 was first brought to the preferred operating point:

$$\begin{bmatrix} V_1\ [\mathrm{V}] \\ V_2\ [\mathrm{V}] \\ I_1\ [\mathrm{A}] \\ I_2\ [\mathrm{A}] \end{bmatrix} = \begin{bmatrix} 379.99 \\ 48 \\ 1.225 \\ 9.6 \end{bmatrix} \tag{5.27}$$

Then, following exactly the procedure from the section 5.2, un-terminated transfer functions were obtained and shown in the Figure 5.12 along with the measured, terminated ones.

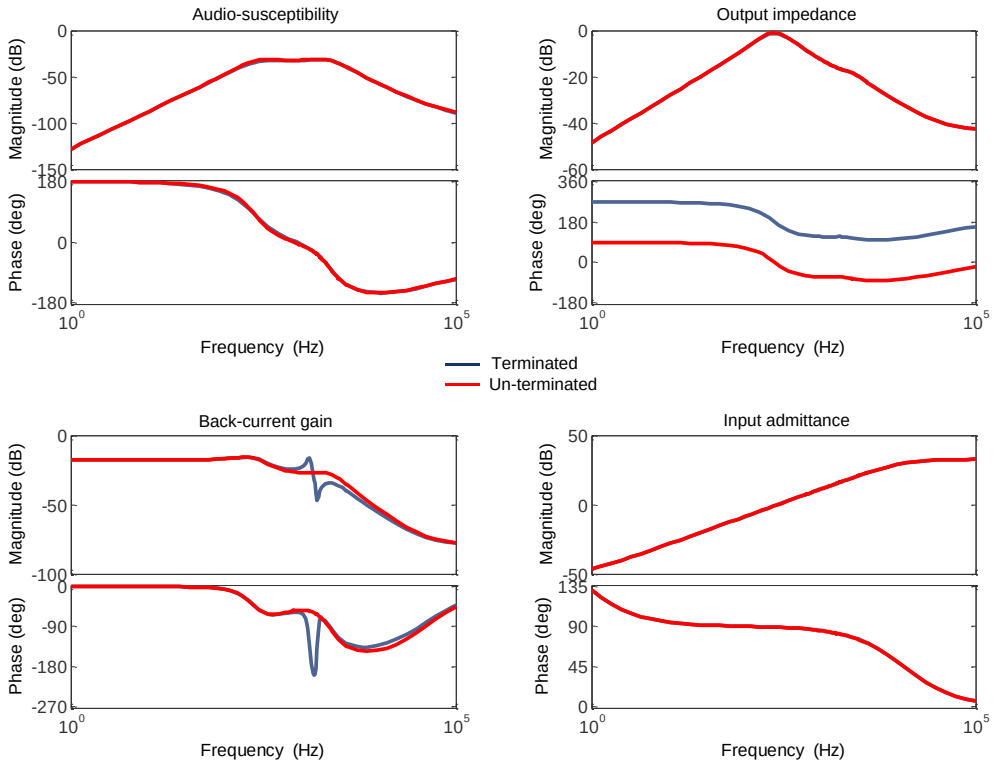

Figure 5.12: **Terminated** and **un-terminated** transfer functions of the converter from Figure 5.11

Now, from the time domain simulation of the system from Figure 5.11, when the load current changes as shown in the same figure, four waveforms are captured. Input voltage, output voltage, input current and output current of the converter. By looking in the Figure 5.4, it can be seen that a two port network behavioral model has two inputs in the system (v_1 and i_2) and two outputs (v_2 and i_1), meaning that when the waveforms captured from the scope v_1 and i_2, are brought into the system, the produced output must, with some degree of accuracy, match with the captured waveforms v_2 and i_1.
As seen in the Figure 5.13, a very good matching of the converter dynamics was achieved.

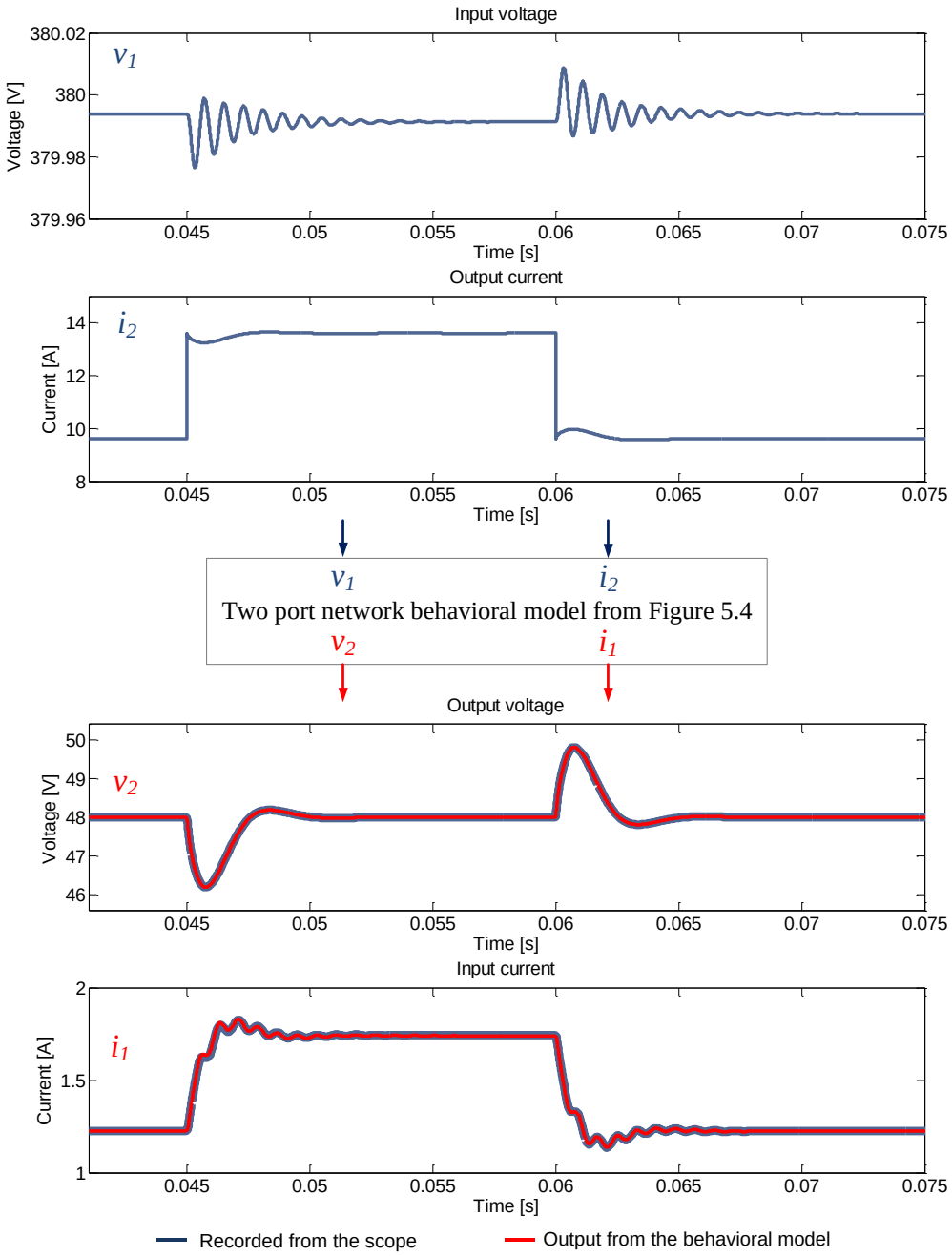

Figure 5.13: Comparison of the time domain responses from the two-port network behavioral model (**red**) and captured waveforms (**blue**)

The next verification of the terminal behavioral model will be performed over the regulated boost converter with the voltage loop closed. The circuit and PI regulator parameters are all given in the Figure 5.14, followed by the un-terminated transfer functions shown along with the measured, terminated ones on the Figure 5.15.

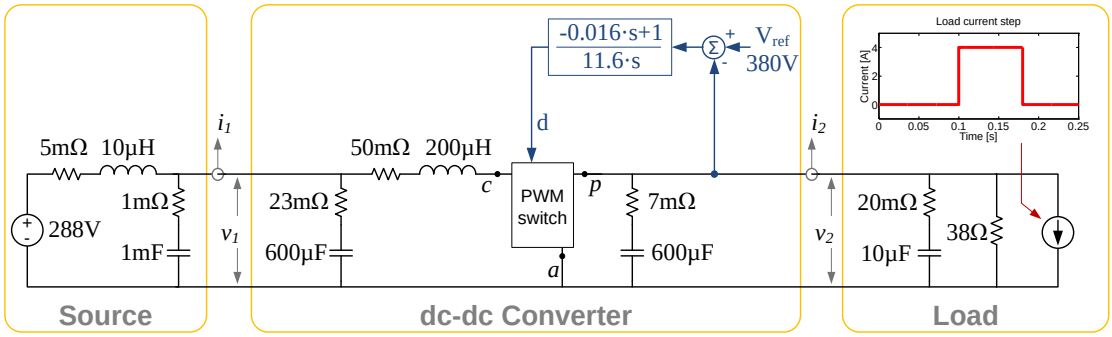

Figure 5.14: Regulated boost converter

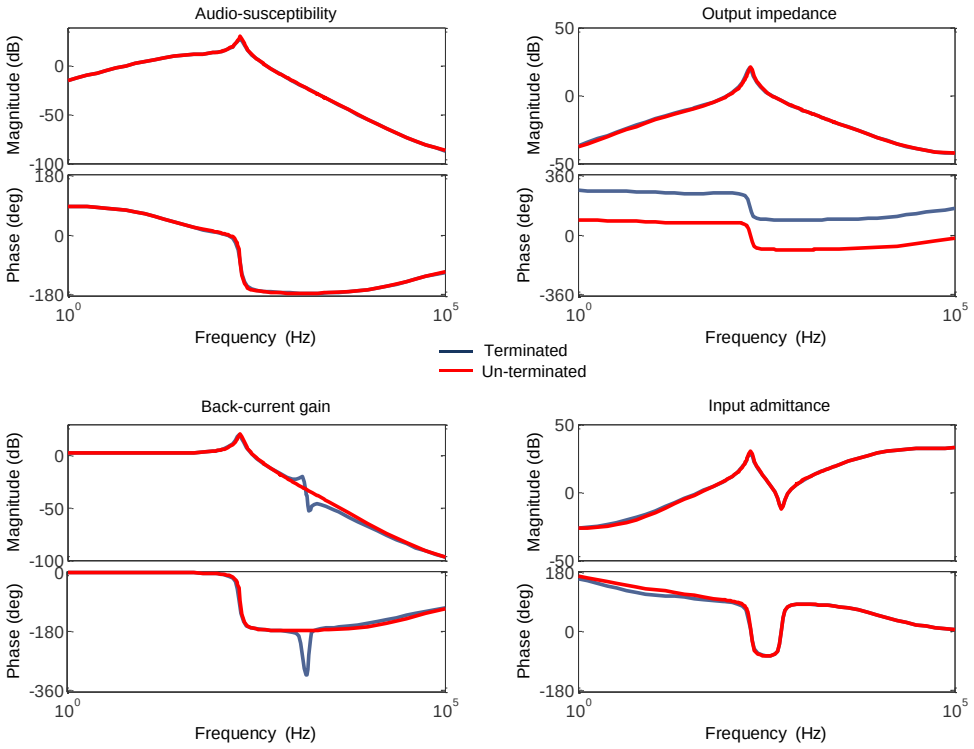

Figure 5.15: **Terminated** and **un-terminated** transfer functions of the converter from Figure 5.14

AC sweep was performed at the desired operating point which was here chosen to be:

$$\begin{bmatrix} V_1\ [\mathrm{V}] \\ V_2\ [\mathrm{V}] \\ I_1\ [\mathrm{A}] \\ I_2\ [\mathrm{A}] \end{bmatrix} = \begin{bmatrix} 287.93 \\ 380 \\ 13.23 \\ 10 \end{bmatrix} \tag{5.28}$$

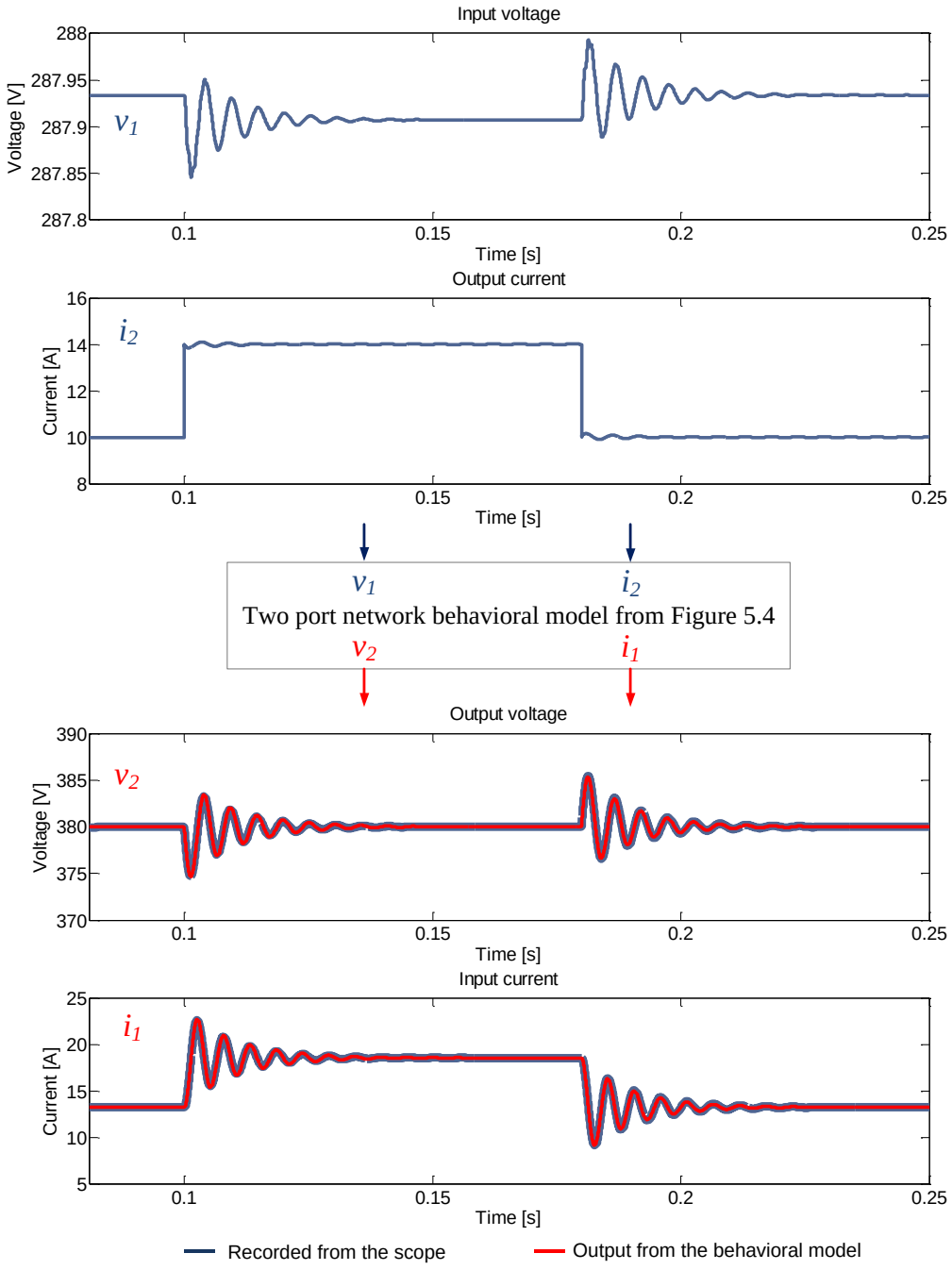

Figure 5.16: Comparison of the time domain responses from the two-port network behavioral model (**red**) and captured waveforms (**blue**)

It is evidently that very good matching is achieved in comparing the recorded time domain response and behavioral model output, despite the fact that regulated boost is a non-linear converter. The reason for good matching lies in a small change of a duty cycle around an operating point (at which ac-sweep was performed), during the load change as shown in the Figure 5.16.

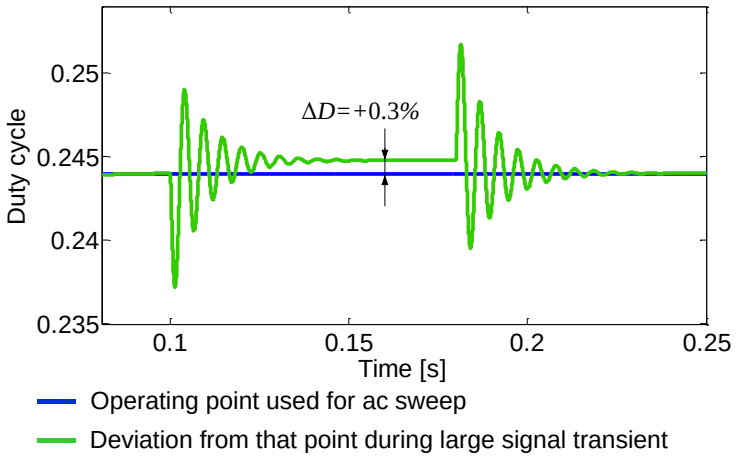

Figure 5.17: Duty cycle change during large signal transients shown in the Figure 5.16

In the previous case an ac-sweep was performed over the converter while working at 50% of the nominal power, and the load change did not significantly influence dynamics for the load change from 50% to 70% of the nominal power. To examine the behavioral model possibilities further with the boost converter, a new ac sweep will be performed at 5% of the nominal power while this converter still works in the continuous conduction mode. Then, the step to the full current (100% of power) and back will be made.

After the system from Figure 5.14 has reached steady state, a new operating point was obtained:

$$\begin{bmatrix} V_1\ [\mathrm{V}] \\ V_2\ [\mathrm{V}] \\ I_1\ [\mathrm{A}] \\ I_2\ [\mathrm{A}] \end{bmatrix} = \begin{bmatrix} 287.99 \\ 380 \\ 1.32 \\ 1 \end{bmatrix} \tag{5.29}$$

The result is shown in the Figure 5.18, where is evident that a slight mismatch is present when low to full power step was introduced to the boost converter (at 0.1s). Full to low power step however shows better performances, what is expected.

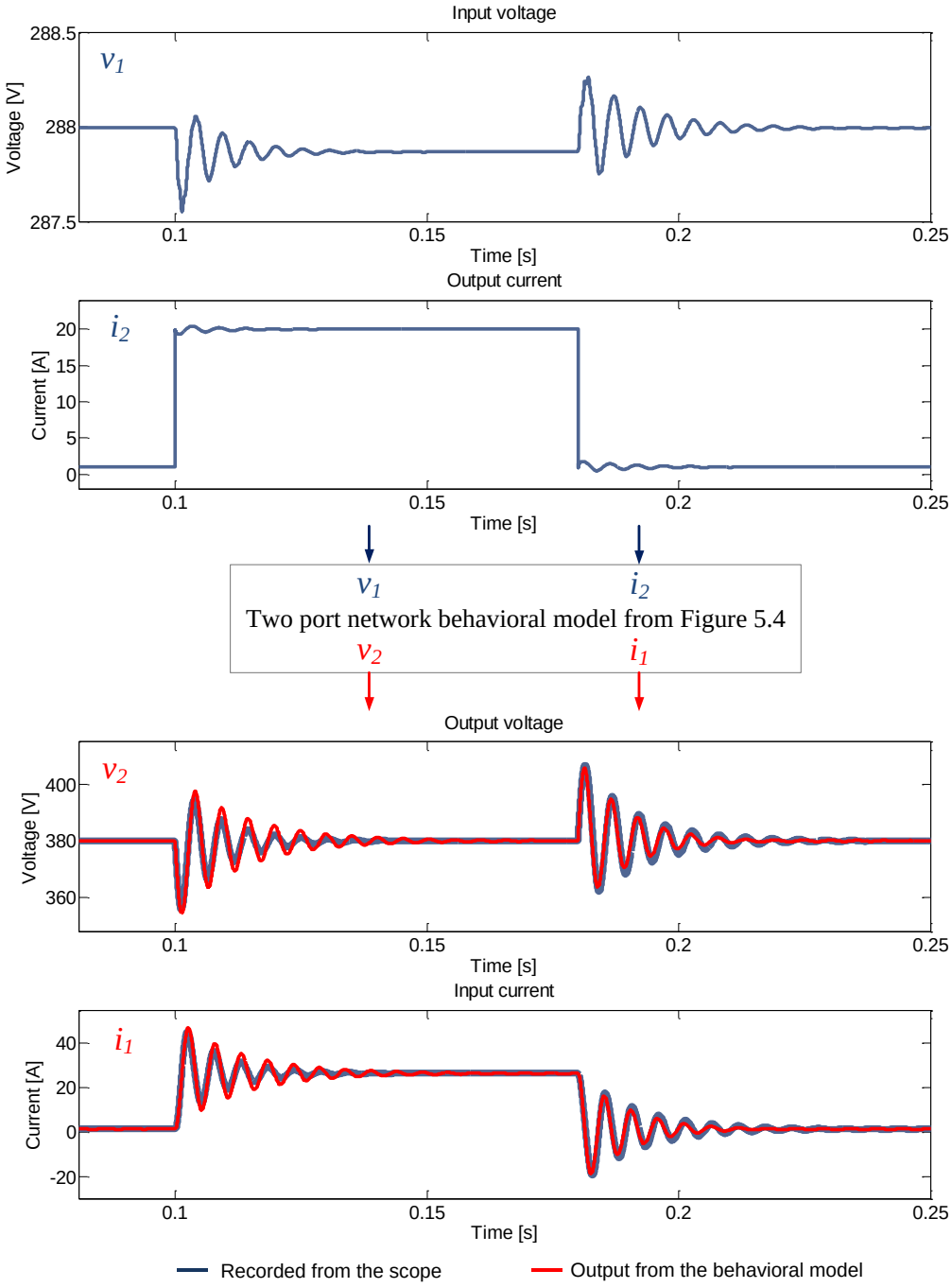

Figure 5.18: Comparison of the time domain responses from the two-port network behavioral model (**red**) and captured waveforms (**blue**)

Previous analysis shows that even when the non-linear converter as boost is concerned, the terminal behavioral modeling may be considered accurate enough for the system level simulations, as well as for the large and small-signal stability analysis.

5.4. Experimental Validation of the Terminal Behavioral Modeling

In this section, validation of the terminal behavioral model performed over the two 380/48 V commercially available converters will be shown. Converters will be brought to a desired operating point, and procedure described in the section 5.2 will be repeated with the difference of the tools for extracting the frequency response functions. Previously, in the simulation, that tool was as sweep on the input and output side of the dc-dc converter model, while here real experimental setup has to be used. This setup is shown in the figure 5.19.

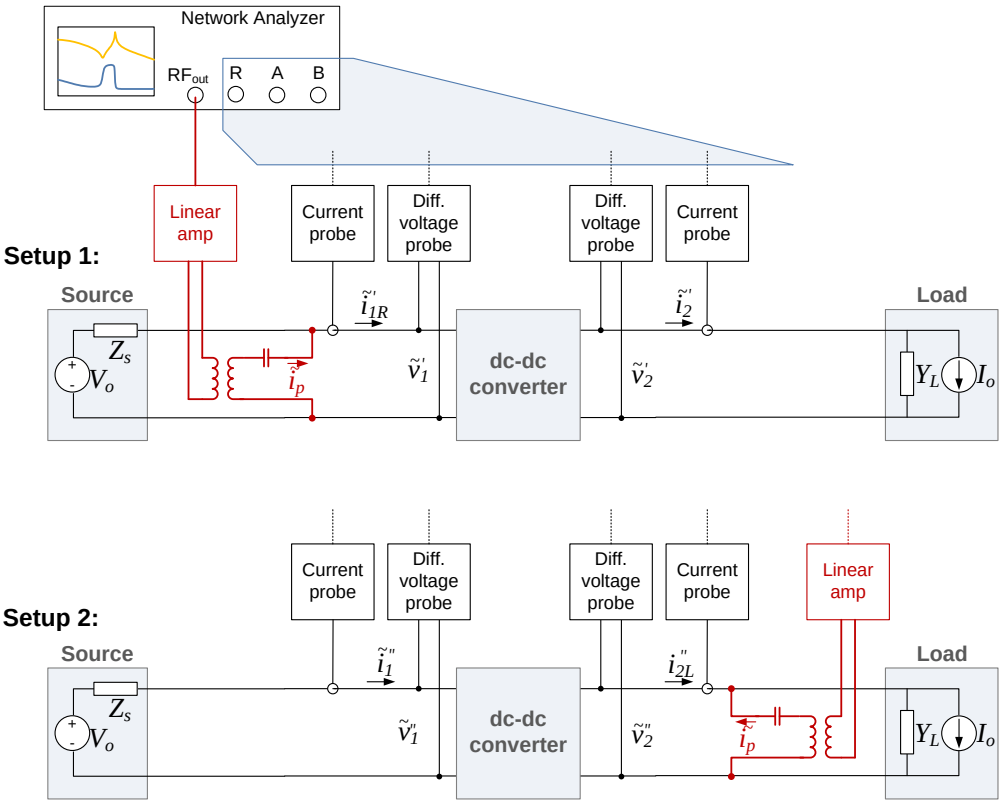

Figure 5.19: Experimental setup for the frequency response characteristics measurement

As explained in the [47], a network analyzer is used together with the linear amplifier to amplify the output of a sinusoidal perturbation signal, since a network analyzer itself is commonly used to analyze the properties of low power electrical networks, especially those properties associated with the reflection and transmission of electrical signals. Unless built as a special category network analyzers that measure frequency responses in the low frequency range, they cover frequencies from a few kHz

to a couple of thousands of GHz. The model 4395A (Agilent) used in this work is a network analyzer with the frequency range from 10 Hz to a 500 MHz, although, the best accuracy guaranteed by the manufacturer can be achieved above 100Hz. On the other hand, when measuring frequency responses of a closed-loop converters, low frequency disturbances injected in the system are being compensated by the feedback network, and thus, the response received by the network analyzer are very small that it actually cannot accurately compute a desired frequency response characteristics [47]. A possible solution to this problem is a good identification procedure that by fitting the higher frequency range of the measured response, could as well estimate the lowest frequency part below the 100 Hz. However, accurately measuring frequency response characteristics in a very low frequency range remains a challenging task and needs more research effort to be put in.

As previously mentioned, terminal behavioral models are low frequency models of dc-dc converters representing their behavior up to the half of a switching frequency, since according to the sample theorem, aliasing phenomena arise above this point [81].

Figure 5.20 shows generalized algorithm that describes steps of building the terminal behavioral model of dc-dc converters from the measured frequency characteristics, and as it can be seen, differs from the procedure explained in the section 5.2 only for a step No.5 which deals with an identification procedure.

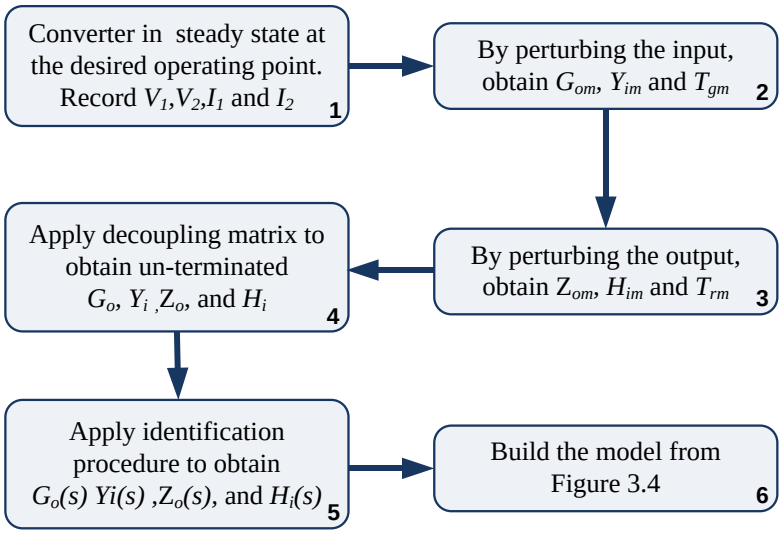

Figure 5.20: Behavioral model step-by-step flowchart

As it will be shown later, an identification procedure is important step of actually obtaining the transfer functions from the measured frequency characteristics. Also, as

the final goal is the use of behavioral models in system level simulations, the order of the system (each dc-dc converter) is expected to be low and allow for a big number of converters to be simulated in the same time.

The first converter to be measured is an open loop, 325 W, 384/48 V high density, resonant ZVS/ZCS sine amplitude intermediate bus converter VIB0002TFJ [82] shown in the Figure 5.21.

Figure 5.21: ZVS/ZCS sine amplitude converter VIB0002TFJ (source: www.vicr.com, 2010)

This converter was powered from the regulated voltage source while as a load, an electronic load was used. An operating point was chosen arbitrarily to be around one third of the rated power, and electronic load current was hence set to 2A working in the constant current mode.

$$\begin{bmatrix} V_1\ [\mathrm{V}] \\ V_2\ [\mathrm{V}] \\ I_1\ [\mathrm{A}] \\ I_2\ [\mathrm{A}] \end{bmatrix} = \begin{bmatrix} 381.2 \\ 47.24 \\ 0.252 \\ 2 \end{bmatrix} \tag{5.30}$$

Following the steps from Figure 5.20, and using the setup shown in the Figure 5.19, the set of frequency response characteristics (G_{om}, Y_{im}, T_{gm}, Z_{om}, H_{im} and T_{rm}) was obtained. Immediately after, the source and load decoupling procedure was performed by using matrix 5.25.

After decoupling, the set of four un-terminated frequency response characteristics (G_o, Y_i, Z_o and H_i) is ready for an identification procedure and to become un-terminated transfer functions of the converter under test.

Figure 5.22 shows un-terminated frequency response characteristics of the converter from Figure 5.21 along with an identified transfer functions plotted over

them. The switching frequency of the particular converter is estimated to be up to 2MHz, so the frequency response was obtained up to 1MHz.

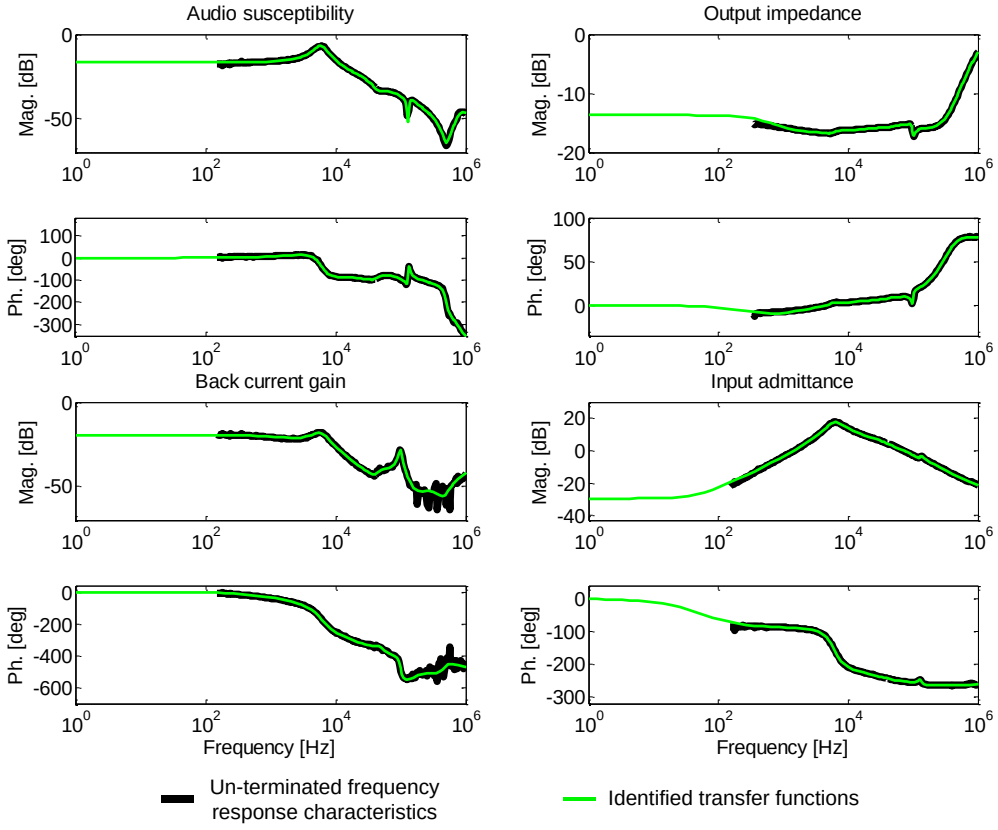

Figure 5.22: **black**: un-terminated frequency response characteristics and **green:** identified transfer functions

An identification procedure is performed in MATLAB, by using code shown in the Appendix of this thesis. By using identified transfer functions and operating point 5.30, the two-port terminal behavioral model of the converter from Figure 5.21 has been built. In order to validate the model, a load current step was introduced to the converter (1.5A to 4.5A with a frequency of 100Hz), and the time domain responses were captured (from the oscilloscope) of the input voltage, output voltage, input current and output current. Later, as done before in the section 5.2, input voltage and output current were introduced to the terminal behavioral model just built as input variables. The output variables, output voltage and input current of the converter were obtained and compared with the ones obtained from the oscilloscope. The result is shown in the Figure 5.23.

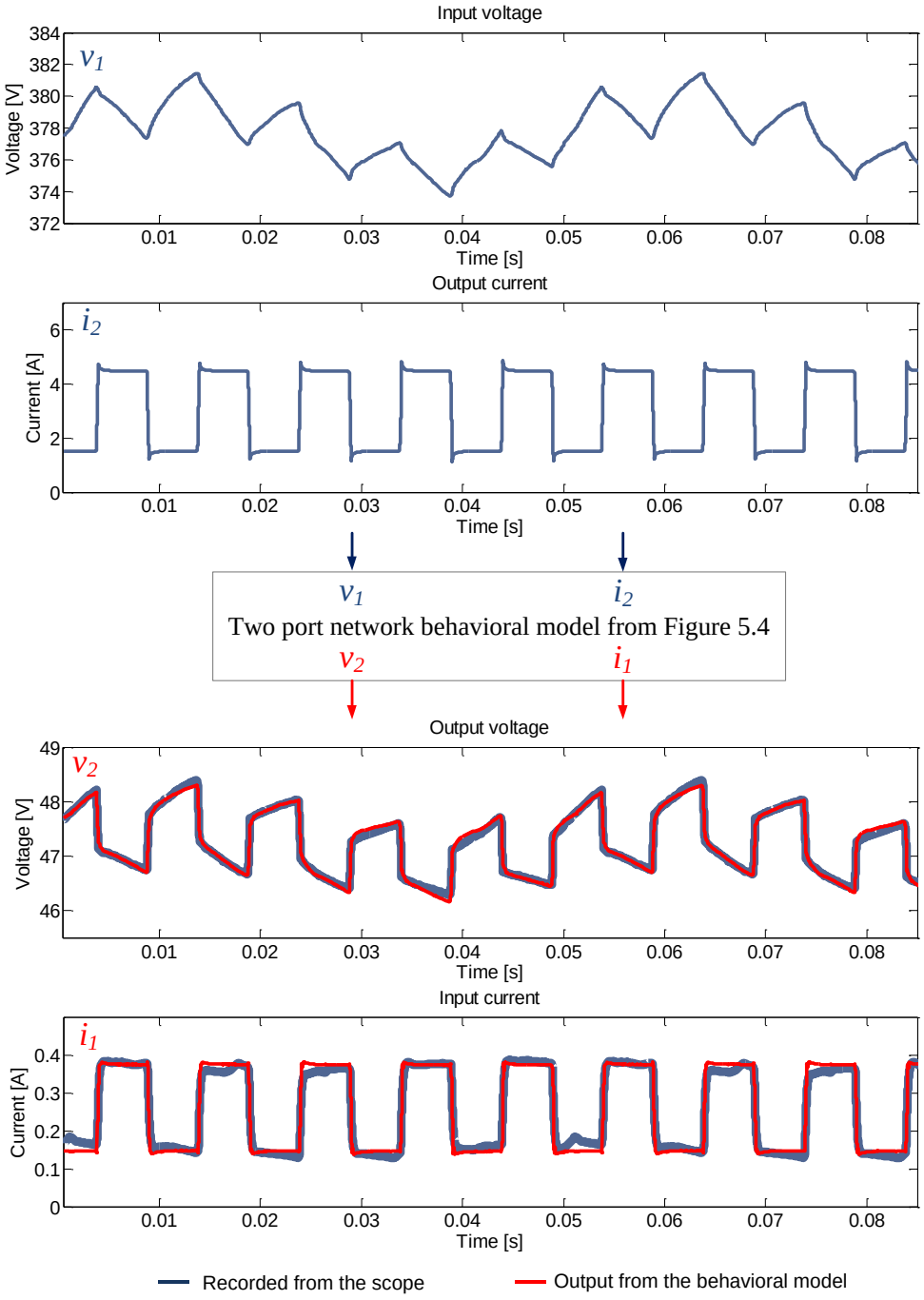

Figure 5.23: Comparison of the time domain responses from the two-port network behavioral model (**red**) and captured waveforms (**blue**)

By observing the figure above, it can be seen that a very good matching was obtained, and the model was even able to follow the sub-harmonic oscillation that non-ideal voltage source was producing. On the other side, not really ideal matching of the input current is obtained, but having in mind that the behavioral model is a low frequency model that should be used in the system level simulations, this results may be

consider good enough.

Although satisfies the "by-eye" criteria, obtained behavioral model is rather of a high order. To be more precise, in order to fit the frequency response characteristics shown in the Figure 5.22, the four transfer functions have orders as shown in the Table 5.1.

Table 5.1: Order of the un-terminated transfer functions from Figure 5.22.

Transfer function	**Order**	**Transfer function**	**Order**
G_{om} – audio susceptibility	18	H_{im} – back current gain	12
Z_{om} – output impedance	18	Y_{im} – input admittance	14

As an attempt to reduce the order of a system above, a reduction technique based on the Hankel singular values of a system [83,84] was used. Hankel singular values are known in the control theory as parameters that define the energy of each state in the system. When reducing the system's order, it is important to preserve states with the larger energy in order to keep the main system characteristics as stability, frequency and time responses.

For a given stable-state space system

$$\begin{aligned} \dot{x}(t) &= \mathbf{A}x(t) + \mathbf{B}u(t) \\ y(t) &= \mathbf{C}x(t) + \mathbf{D}u(t) \end{aligned} \tag{5.31}$$

with eigenvalues $\lambda_i = \{\lambda_1, \lambda_2, \lambda_3, ..., \lambda_n\}$, its Hankel singular values are defined as:

$$\sigma_H = \sqrt{\lambda_i(\mathbf{PQ})} \tag{5.32}$$

Where P and Q are controllability and observability grammians that are solutions to Lyapunov equation:

$$\begin{aligned} \mathbf{AP} + \mathbf{PA}^T &= -\mathbf{BB}^T \\ \mathbf{A}^T\mathbf{Q} + \mathbf{QA} &= -\mathbf{C}^T\mathbf{C} \end{aligned} \tag{5.33}$$

Hankel singular values of, for example, audio-susceptibility are plotted and shown in the Figure 5.24 (in MATLAB, command *hsvd* plots the Hankel singular values).

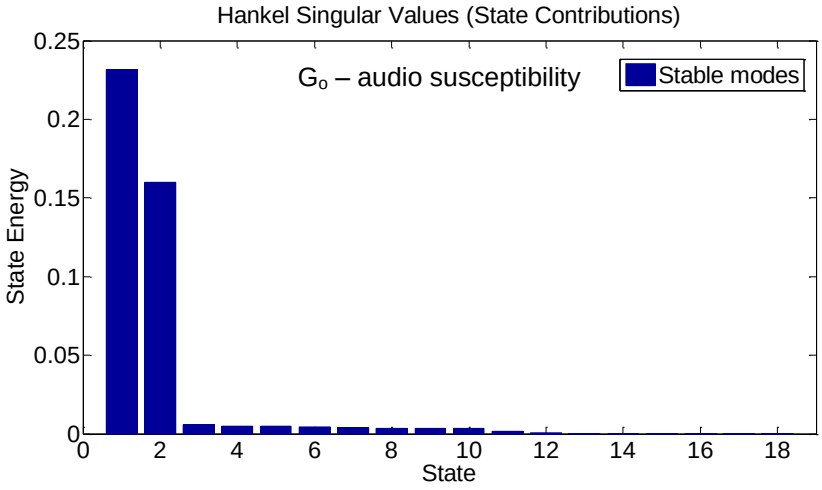

Figure 5.24: ZVS/ZCS sine amplitude converter VIB0002TFJ

As it can be seen from the Figure above, only 2 out of 18 states contribute with the high system energy. This practically means that the audio susceptibility can be actually defined as a second order system by keeping almost the same dynamics and properties. By following the same procedure for the other transfer functions, obtained are and plotted in the Figure 5.25 reduced order transfer functions. (In MATLAB, commands like *reduce*, *modreal* or similar can be used for the order reduction [85]).

Table 5.2: Order of the un-terminated transfer functions after reduction

Transfer function	**Order**	**Transfer function**	**Order**
G_{om} – audio susceptibility	2	H_{im} – back current gain	2
Z_{om} – output impedance	2	Y_{im} – input admittance	2

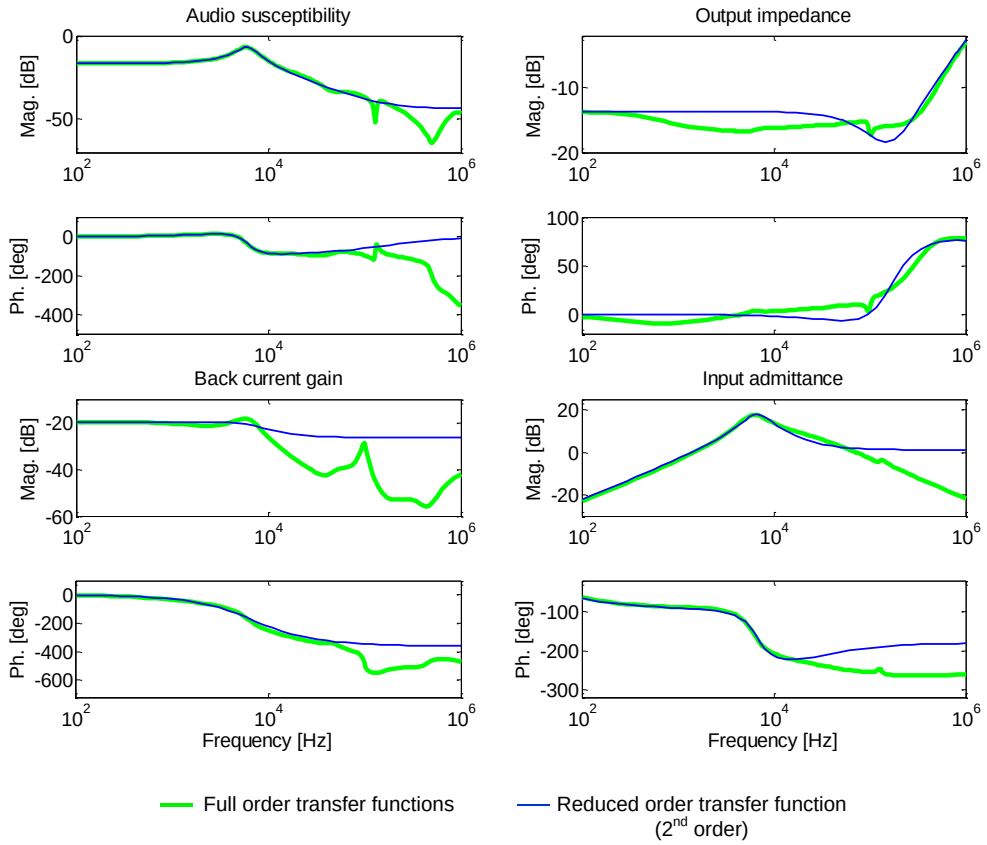

Figure 5.25: Full and reduced order un-terminated transfer functions of the converter from Figure 5.21.

As seen in the Figure above, transfer function's orders are significantly reduced, and the new dynamics of the behavioral model has to be checked now. As inputs to the system, the same signals shown in the Figure 5.23 are brought into the behavioral model built with the full order transfer functions and reduced order. The resulting outputs, an output voltages and input currents in the two cases are plotted on the top of each other for comparison. The result is shown in the Figure 5.26, and it is evident that just a slight difference exists between the two responses which proves that the reduced order system can now be used for analysis and system level simulations by significantly increasing their execution time and allowing more component to be included.

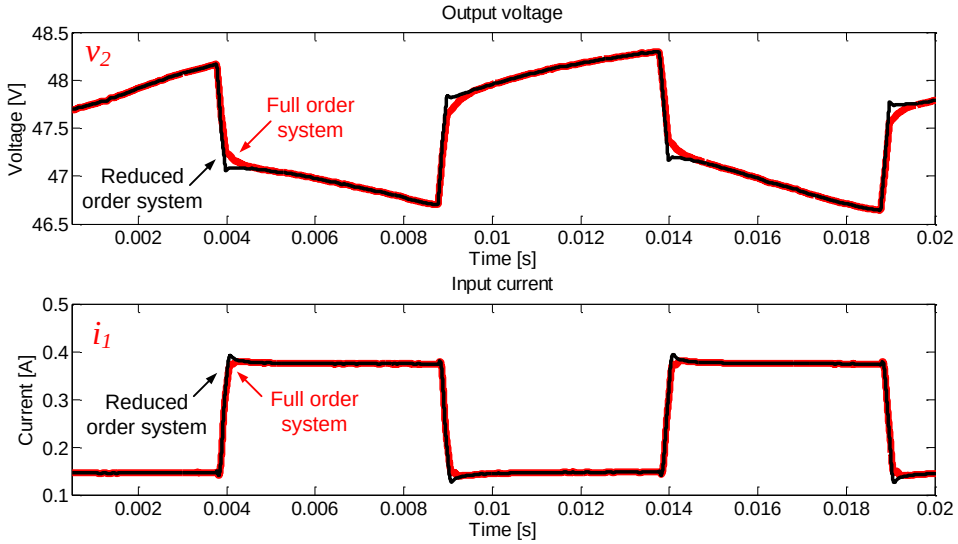

Figure 5.26: Output of the terminal behavioral model when built with **full-order** and **reduced** order transfer functions

5.5. Terminal Behavioral Model of Sources and Loads

The same procedure used above for obtaining the terminal behavioral model of dc-dc converter is used for obtaining terminal behavioral model of sources and loads. Figure 5.27 shows small-signal models of the general source and load respectively.

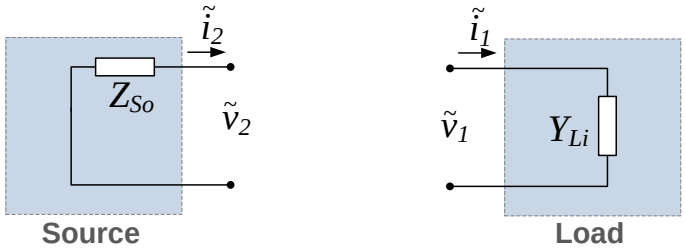

Figure 5.27: Small-signal models of source and the load

Small-signal equations can be written (for the given direction of currents) as:

$$\tilde{v}_2 = -Z_{So}\tilde{i}_2 \tag{5.34}$$

$$\tilde{i}_1 = Y_{Li}\tilde{v}_1 \tag{5.35}$$

Now, to expand the systems (5.34) and (5.35) to a models where input and output variables consist of *ac* small-signal variation and *dc* operating point, which are, in practice, more meaningful models since these quantities can be directly measured in the time domain (for example on the oscilloscope), it can be written:

$$v_2 = \tilde{v}_2 + V_2 = -Z_{So}\tilde{i}_2 + V_2 \tag{5.36}$$

$$i_1 = \tilde{i}_1 + I_1 = Y_{Li}\tilde{v}_1 + I_1 \tag{5.37}$$

Or expressed only with the quantities and the operating point around which the source and the load are linearized:

$$v_2 = V_2 - Z_{So}(i_2 - I_2) \tag{5.38}$$

$$i_1 = I_1 + Y_{Li}(v_1 - V_1) \tag{5.39}$$

Finally, generic terminal behavioral models of the source and load are shown in the Figure 5.28.

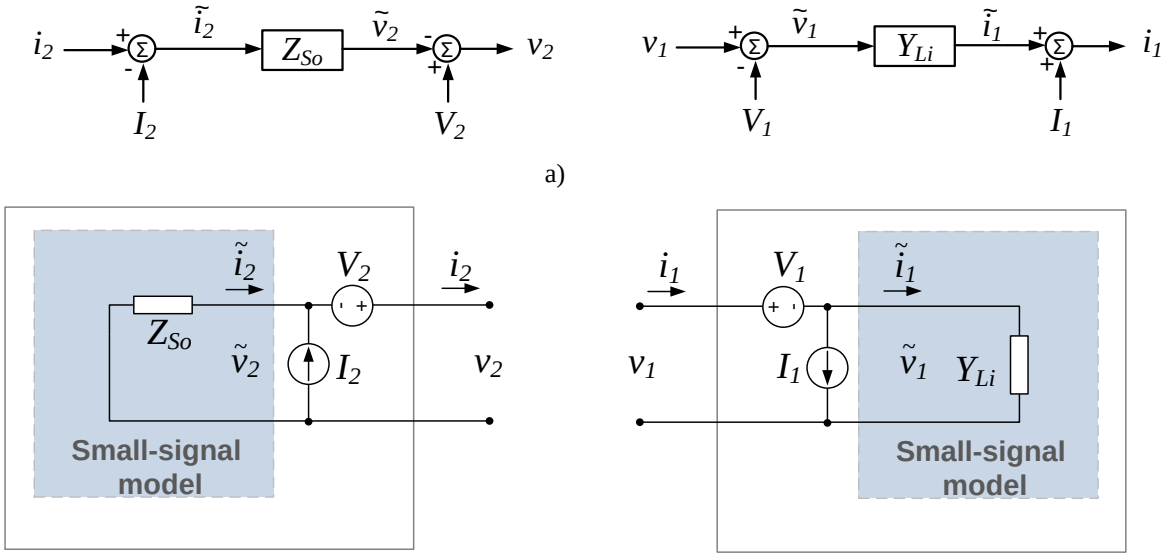

Figure 5.28: a) Block diagram of a two-port network behavioral model of a source (left) and the load (right) b) Their equivalent circuits: source (left) and the load (right)

5.6. System Level Terminal Behavioral Models

The whole procedure for terminal behavioral identification described above can be, exactly in the same way, applied to the much more complex systems. For instance, system illustrated in the Figure 5.29 presents an example of complex Electronic Power Distribution System (EPDS), with a variety of dc-dc converters, and also its complete

two-port terminal behavioral model.

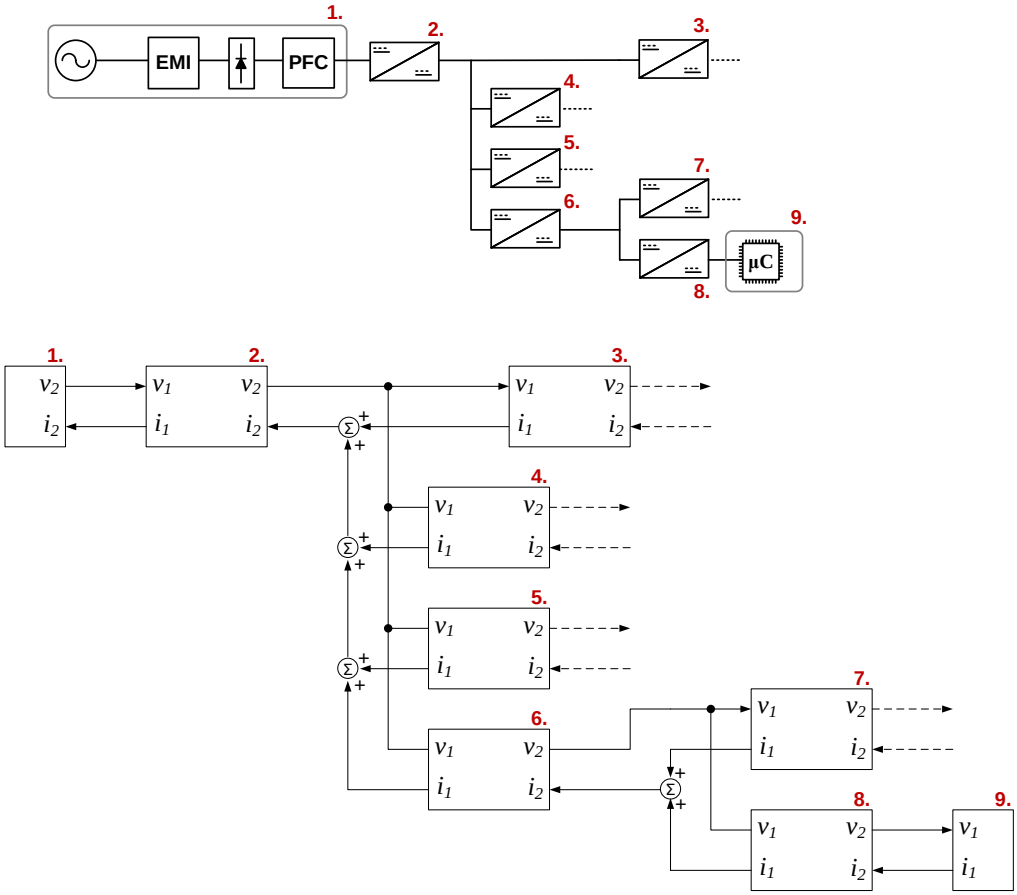

Figure 5.29: An example of a Electronic Power Distribution System and its complete terminal behavioral model

Arbitrarily converter from the system above can be identified on-line, without a need to be taken out and characterized by being connected to the "known" source and the load. The only constrain that system has to satisfy when obtaining the frequency response functions is that steady-state operating conditions and temperature should not change, which is not practically impossible, knowing the fact that the time required to complete ac-sweep (all six frequency response characteristics) of the converter is only a few minutes. Following the same procedure, behavior of the whole EPDS shown in the figure below can be obtained. If the system can be considered linear or mildly non-linear, then even the system operating point and/or temperature can change between characterizations of individual system components.

Another big advantage of terminal behavioral identification is that not only sources, loads and dc-dc converters can be identified and simple terminal behavioral models built, but also EMI, common and differential mode filters, cables and everything that can be represented as a SISO or two-input/output MIMO system.

Chapter 6. NON-LINEAR, HYBRID TERMINAL BEHAVIORAL MODELS

The procedure to obtain terminal behavioral models explained in the previous chapter assumes linearity or mild non-linearity of the system components. But, to extend the models capability, more realistic cases will be considered where system components could be highly non-linear as, for example, solar and wind converter characteristics designed for dc-nanogrid system in the Chapter 3 of this thesis. The goal here is to develop a procedure for the terminal identification, so-called black box modeling approach when engineers do not have an access to the internal structure, control and dynamics of the converters, but through an appropriate measurements can extract needed information useful later for the system level simulations, stability analysis etc.

In order to address non-linear system modeling, a Hammerstein's [86] generic model shown in the Figure 6.1 was used as a basis in this work, by representing non-linear SISO systems dividing their static (steady-state) from dynamic (transient) behavior. The non-linear static model is then used as an input into the dynamic model.

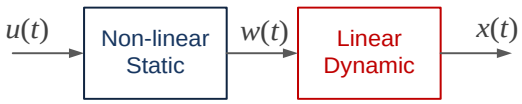

Figure 6.1: Hammerstein's nonlinear model

Figure 6.2 provides a simplified illustration of the methodology that will be used in the sections below. Shown system consists of the source, dc-dc converter and the load. The non-linear static model of the complete system is run simultaneously in the simulation with the linear dynamic model comprised of the four un-terminated transfer functions.

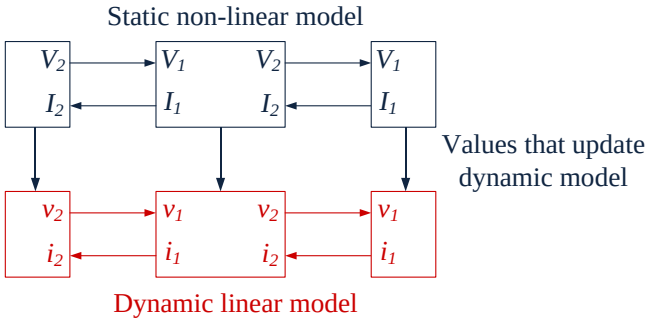

Figure 6.2: Hybrid behavioral model of the source – dc-dc converter – load system

As it will be shown below, the static model has information about the system and system component's operating points, and when some disturbance (input voltage or load change) occurs, it feeds back the new operating point to the dynamic system and no steady state error occurs as a result of simulation even for the highly non-linear loads. However, dynamic change of non-linear systems is still an issue that requires research focus and is left as a future work on this matter, thus has not been included in this thesis.

6.1. Hybrid model of dc-dc converters

6.1.1. Static Model

Despite the fact that "from the shelf" converters are black boxes for the end user, there is a way to extract their static characteristics very precisely from a set of measurements by capturing steady state values of the input voltage, output voltage, input current and output current from the precise volt- and ampere-meters. The temperature should be kept constant in the whole range of the converter load, from 0% to 100% of the nominal power. Such measurements are performed over the converters chosen as good candidates for the nanogrid system to serve as an interface between the bus (360 V – 400 V) and the low voltage (48 V) local distribution. These converters are 250 V ÷ 425 V / 48 V, ZVS / ZCS, 600 W V375A48E600BN and 300W V375B48E300BN [82]. In order to obtain precise measurements without a big temperature variation, the higher temperature points were located at the converter bases with the thermal camera. Figure 6.3 shows thermal images of the converters' base when working, loaded with 50% of the nominal power.

Once the point with the highest temperature was discovered, a small, shallow notch was made in the converter's base as shown in the Figure 6.4, able to accommodate the thermocouple.

After the thermocouple was "built-in", the converters were put on the appropriate heat-sinks with the thermal pads and screwed in. In order to maintain the temperature during the static identification procedure, a control and data acquisition unit 34970A (Agilent) was used. Unit was measuring the temperature through the embedded thermocouple, and the hysteresis temperature controller was, by turning the fan on and off, maintaining the temperature of the converter under test as shown in the Figure 6.5.

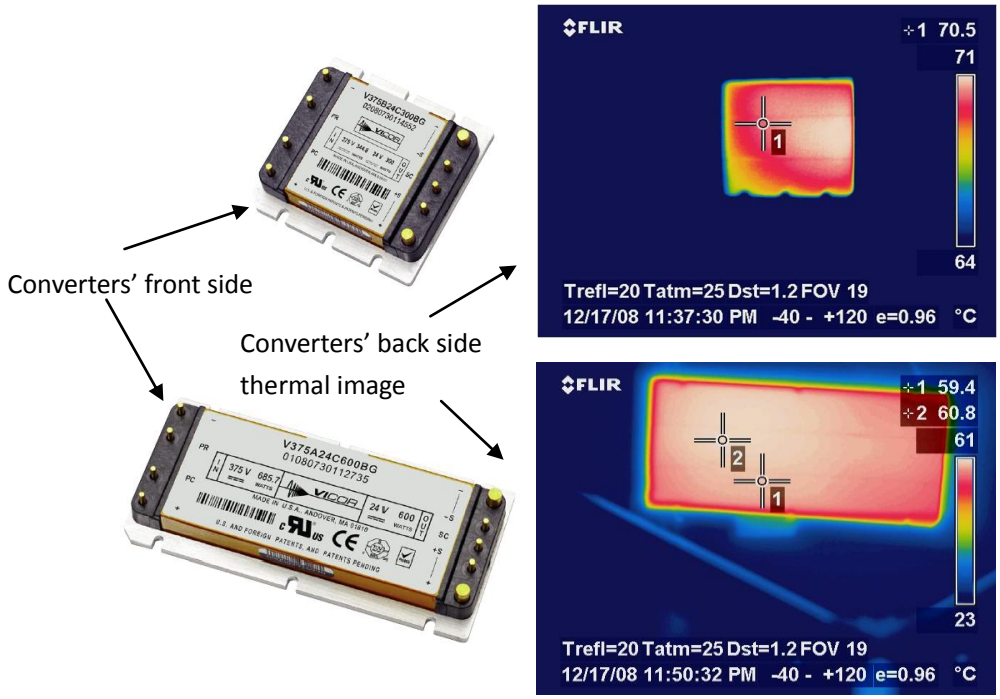

Figure 6.3: Thermal pictures of the converters' bases

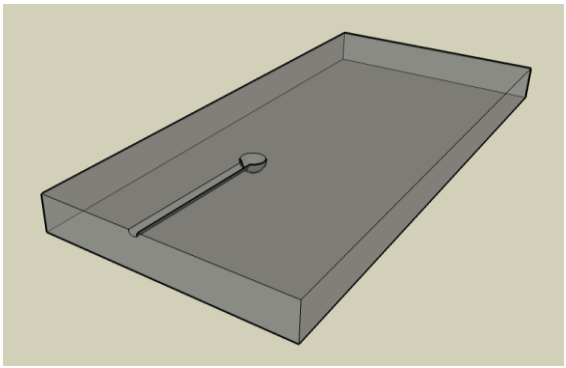

Figure 6.4: Notch in the converter base as a place for embedding the thermocouple wire

To obtain the measurements at the particular, fixed temperature, in the whole operating range from light to full load of the converter, the problem were measurements of the light load operating points at high temperatures. The converter losses were simply not high enough to heat-up the converter to, for instance 85 °C working with the 5-10% of the nominal load.

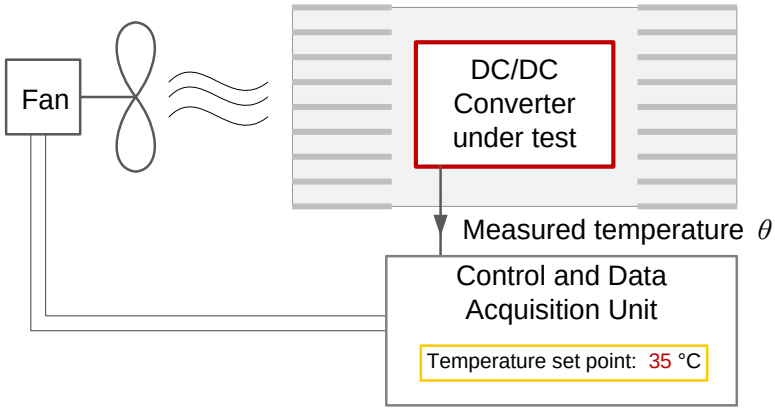

Figure 6.5: Setup used to maintain the temperature constant during the measurement

This was solved by loading the converter more than 50% and waiting for the temperature rise to reach slightly higher temperature than desired, and readings were captured in the cooling cycle close around the desired temperature point. The following set of measurements, shown in the Figure 6.6 is obtained for the two previously mentioned converters. Roughly 15-20 operating points were captured in the one set of measurements, for the fixed temperature from light to full load. The process can then be repeated desired number of times for the different temperatures. Static measurements shown in the Figure 6.6 were performed for the three arbitrary chosen temperature points, and were originally obtained as data pairs (x,y) that were interpolated with the higher order polynomial functions

$$f(x) = a_n x^n + a_{n-1} x^{n-1} + \ldots + a_2 x^2 + a_1 x + a_0 \tag{6.1}$$

for the better readability and for building the static terminal behavioral model.

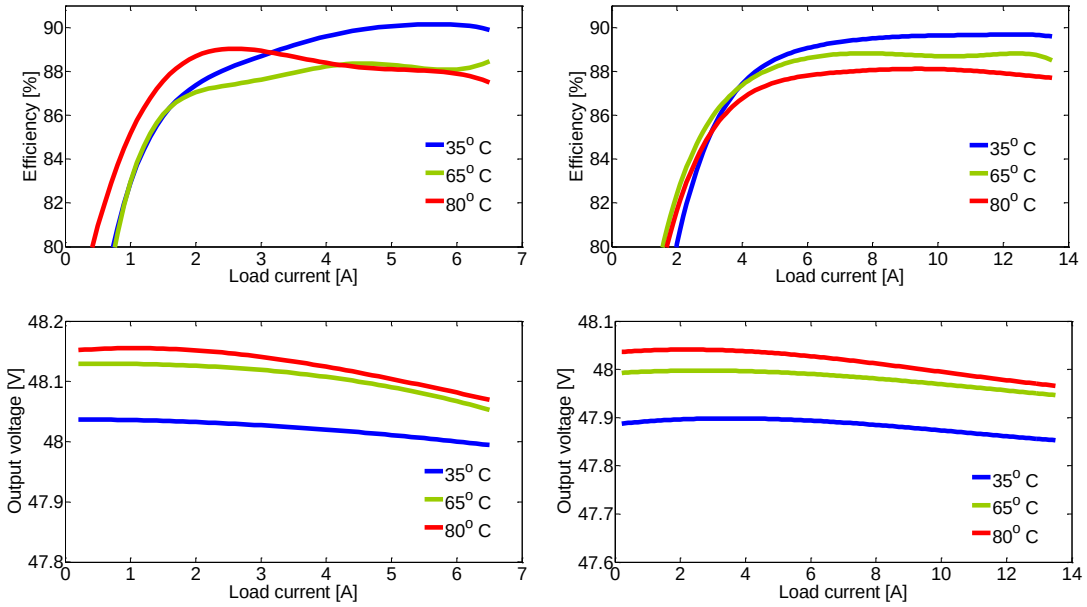

a) b)

Figure 6.6: Static characteristics of two converters a) 300W and b) 600W

As seen, in the Figure above, only two sets of measurements are taken, and as will be shown in the following section, that is enough to build the complete static terminal behavioral model of dc-dc converter.

Static terminal model has a structure as represented in the Figure 6.7. Input signals to the system are input voltage and output current with addition of the converter temperature, while the outputs (or response signals) are input current and output voltage.

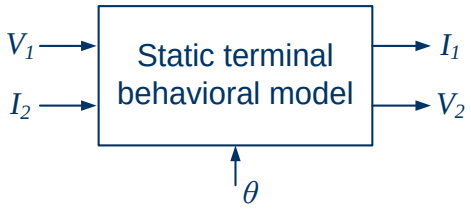

Figure 6.7: Static terminal behavioral model of the dc-dc converter

According to the Figure 6.6, and 6.7, proposed static terminal behavioral model is shown in the Figure 6.8.

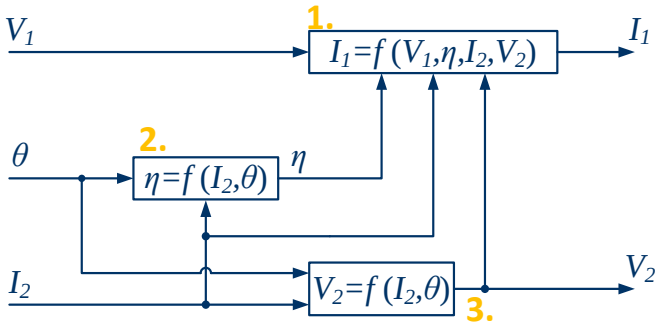

Figure 6.8: Static terminal behavioral model of the dc-dc converter

As seen in the Figure above, the static model is built with a three functions, where only two (No.2 and No.3) are independent and have to be measured separately while No.1 is dependent and can be calculated in a way shown in (below):

$$V_1 = \frac{V_2 I_2}{\eta I_1} \tag{6.2}$$

In order to validate the model, polynomial functions

$$\eta = f(I_2, \theta) \tag{6.3}$$

$$V_2 = f(I_2, \theta) \tag{6.4}$$

obtained from the measurements shown in the Figure 6.6 will be used to build the model shown in the Figure 6.8, and as an output, function

$$V_1 = f(I_1, \theta) \tag{6.5}$$

will be evaluated and compared with the real measurement results performed on the 300W, V375B48E300BN converter. The result of this validation is shown in the Figure 6.9, and as seen, almost perfect matching was achieved between the model and real measurement results.

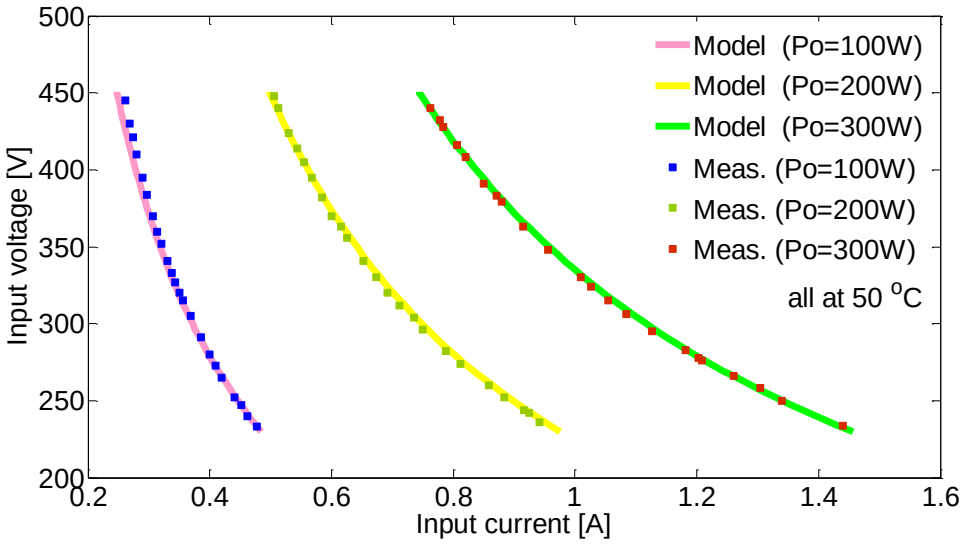

Figure 6.9: Validation of the static terminal behavioral model

For the purpose of verification with an average model, the system from the Figure 6.10 was used. Evident is addition of the non-linear part providing voltage reference according to inductor current, done for the purpose of addressing the non-linear terminal behavioral modeling.

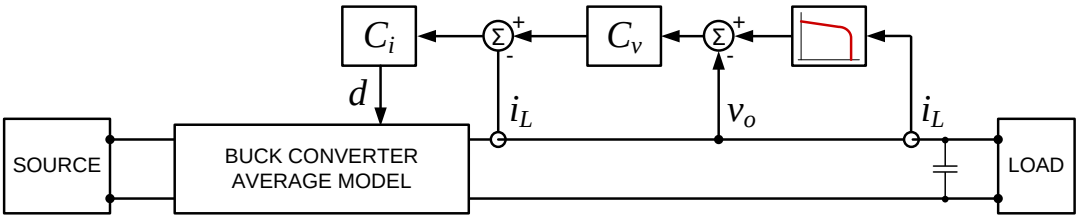

Figure 6.10: Model used for verification of the hybrid non-linear terminal behavioral modeling

The static model was obtained first, by changing the load in steps from zero to full converter power, and obtained are pairs (I_o,V_o). The Figure 6.11 shows these points along with identified, fitted curve which expression is given in (6.6).

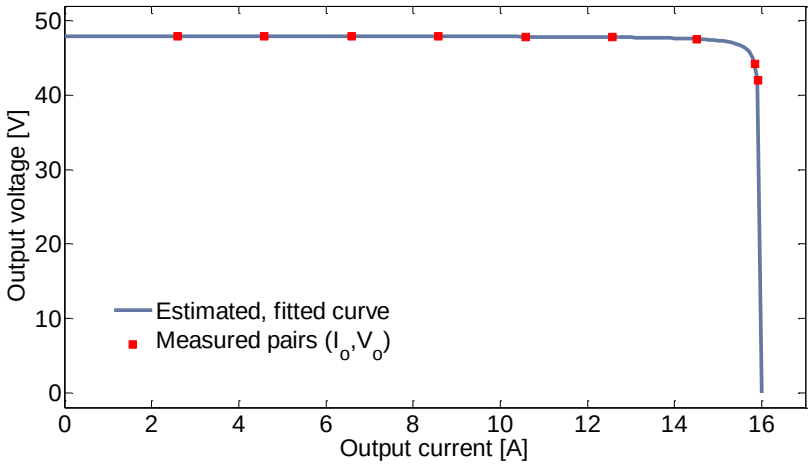

Figure 6.11: Output current vs output voltage relationship

In order to slightly simplify the procedure, it will be assumed that converter operates at the fixed temperature with efficiency of the converter constant in all operating points and equal to 99%, so the model from Figure 6.8 becomes:

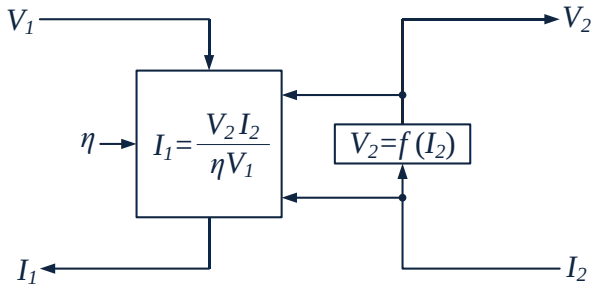

Figure 6.12: Simplified static terminal behavioral model

As seen, the output current can be obtained from:

$$V_1 = \frac{V_2 I_2}{\eta I_1} \tag{6.6}$$

Once the non-linear static terminal behavioral model is defined, dynamic model has to be built.

As mentioned before, for dynamic identification, converter does not need to be taken out from the original system, and frequency characterization can be done on-line.

6.1.2. Dynamic Model

The ac-sweep was performed over the converter shown in the 6.10, loaded with 15% of the nominal power, where the converter is still in the voltage regulation mode and features more linearity than in voltage-to-current transitional mode as shown in the Figure 6.11. The desired operating point is thus:

$$\begin{bmatrix} V_1\ [\mathrm{V}] \\ V_2\ [\mathrm{V}] \\ I_1\ [\mathrm{A}] \\ I_2\ [\mathrm{A}] \end{bmatrix} = \begin{bmatrix} 379.99 \\ 47.95 \\ 0.3278 \\ 2.59 \end{bmatrix} \tag{6.7}$$

Following the procedure from Chapter 5, un-terminated transfer functions were obtained and shown in the Figure 6.13 along with the measured, terminated ones.

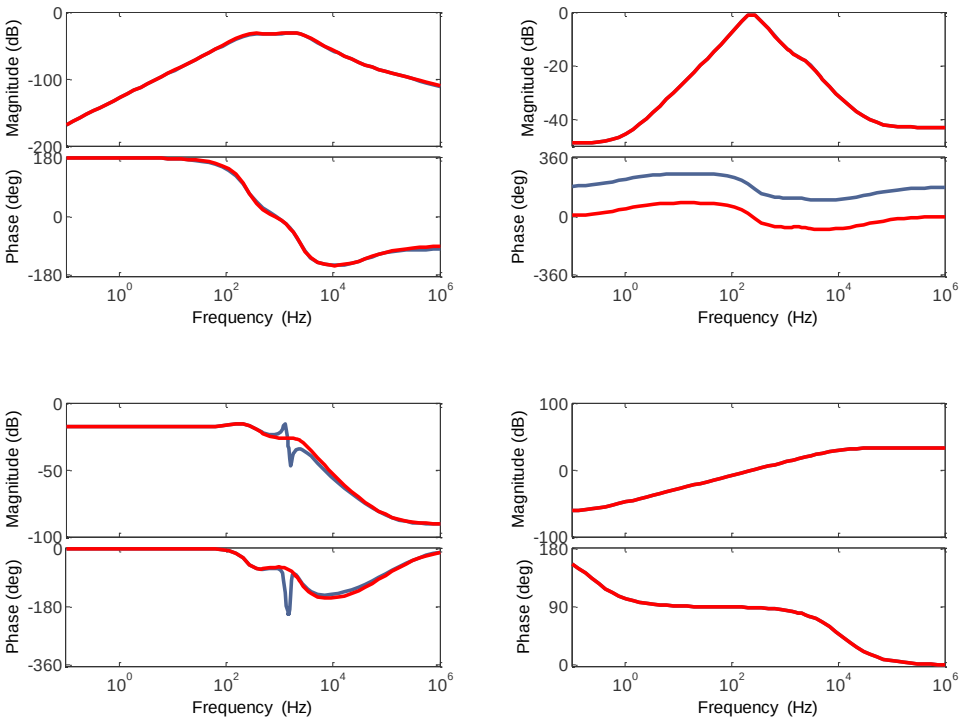

Figure 6.13: **Terminated** and **un-terminated** transfer functions of the converter from Figure 6.8

Figure 6.14 shows dynamic model of dc-dc converter already seen in the Chapter 5.

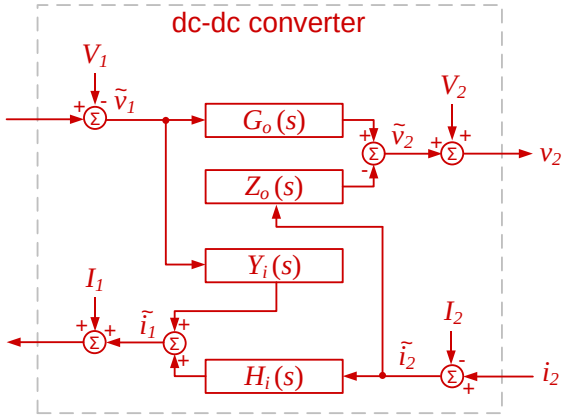

Figure 6.14: Dynamic two-port network terminal behavioral model

6.1.3. Hybrid Model

According to the previously defined non-linear static and linear dynamic model, the hybrid, nonlinear terminal behavioral model of dc-dc converter from 6.10 is built and shown in the Figure 6.15.

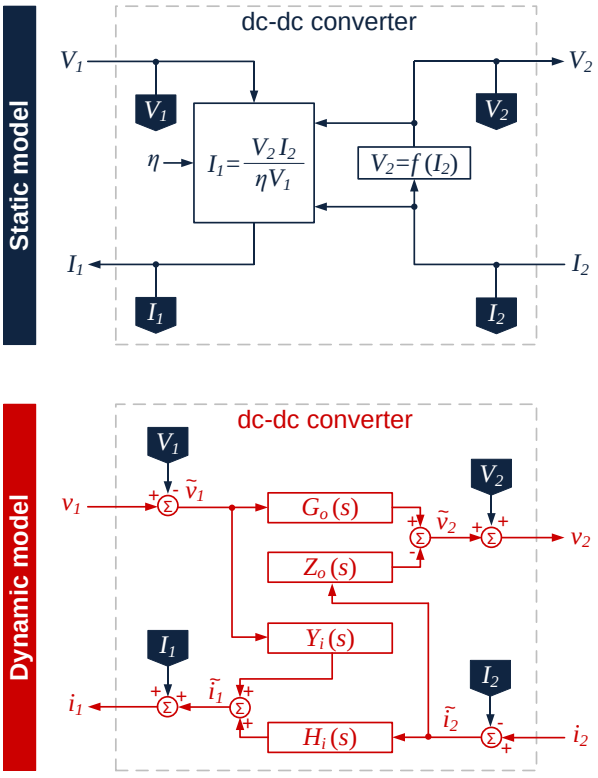

Figure 6.15: Hybrid, nonlinear terminal behavioral model of dc-dc converter from 6.10

It can be seen that the static non-linear model is run simultaneously with dynamic model, by updating it with the operating point corresponding to the static non-linear characteristic. The Figure 6.17 shows the case when non-linear static model and dynamic model are both run independently for the imposed large signal transient that moves point "A" from the Figure 6.16 to the point "B", and then compared with the average model of the system shown in the Figure 6.10.

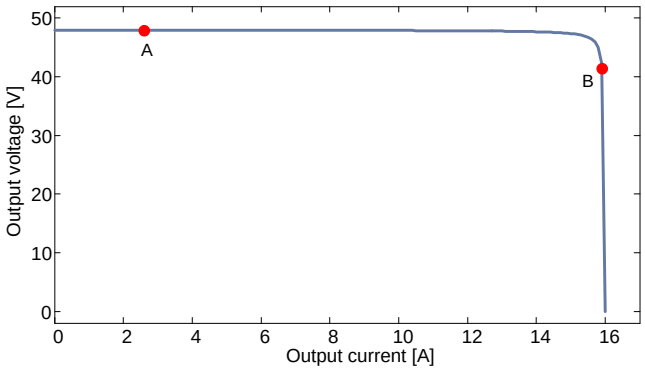

Figure 6.16: Output characteristics of the dc-dc converter from 6.10, and two dc operating points

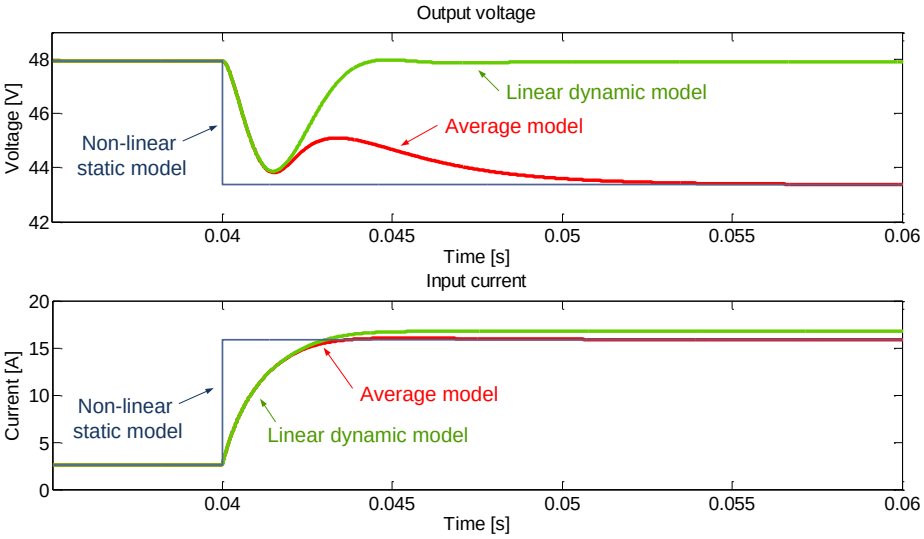

Figure 6.17: Comparison of the average, non-linear static and linear dynamic model response

There is an evident mismatch in the figure above between the average model and linear dynamic model which tend to behave according to the frequency response functions measured in the point A, and is not "aware" about the different dynamic behavior in the point B. On the other hand, non-linear static model obviously has no steady-state error.

The Figure 6.18 shows a comparison between the average and the hybrid model from Figure 6.15. It can be seen that combination of non-linear static and linear dynamic can give zero steady-state error, but still not dynamically accurate transition. The last one is, as mentioned before, left for the further investigation and research effort, therefore will not be addressed in this thesis.

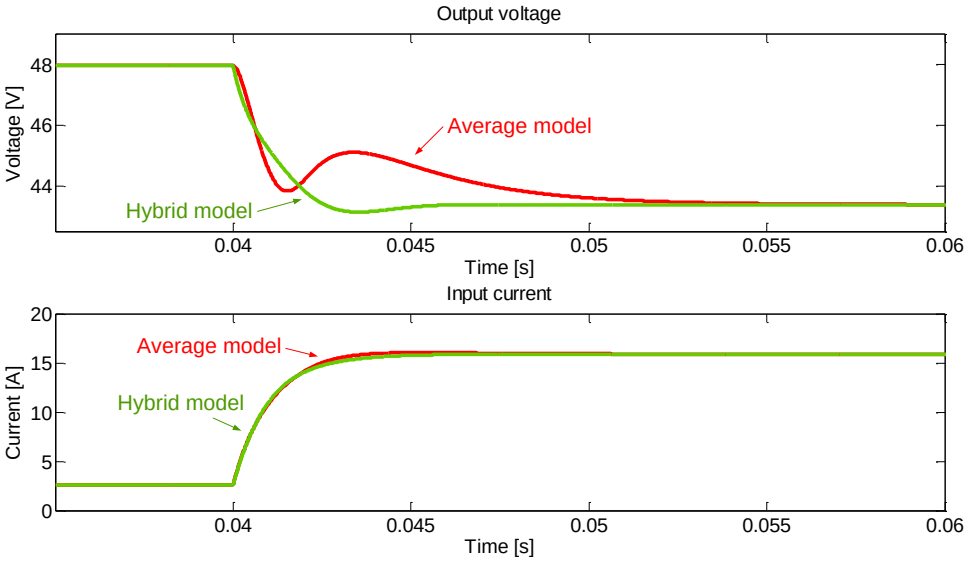

Figure 6.18: Comparison of the average and hybrid model

6.2. Generic Hybrid Model of the Source and Load

6.2.1. Generic static model of the source and load

As seen in the Chapter 3, source converters for the dc-nanogrid system feature static and dynamic non-linearity. In general, this can be the case with any other "from the shelf" power supply, and engineers may have some or none information regarding static behavior of the particular converter, and thus have to obtain them through the static characterization similar to one shown in the section 6.1. Source has to be disconnected from the original system and connected to the controllable load (electronic) in order to obtain as many pairs (output current, input voltage) as possible. The load range should go from zero to full rated power, and if possible cover the current limit range (if any) with the use of variable resistance that the majority of laboratory electronic load feature. Once that is done, static model can be built in the form of analytical expression or look-up table. The procedure for the load that needs to be

characterized is completely the same, and everything that was said for the source holds for the load too.

The generic static non-linear models for the source and load are shown in the Figure 6.19.

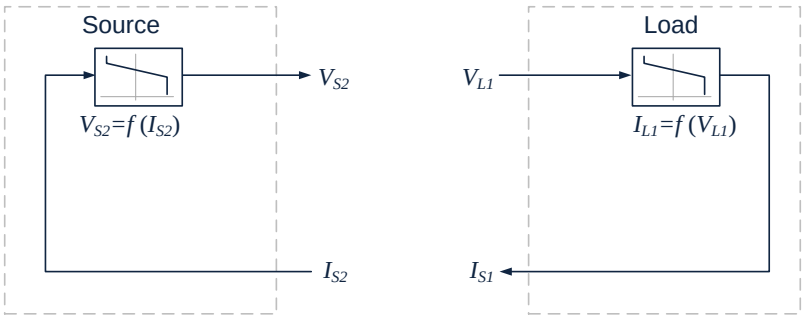

Figure 6.19: Output characteristics of the dc-dc converter from 6.10, and two dc operating points

6.2.2. Generic Dynamic Model of the Source and Load

Single output sources and single input loads are, in general, SISO systems dynamically described by only one transfer function: output impedance for source and input admittance for the load. Dynamic model is represented as a small-signal model with addition of the operating point at which the particular transfer function was obtained. Models are shown in the Figure 6.20.

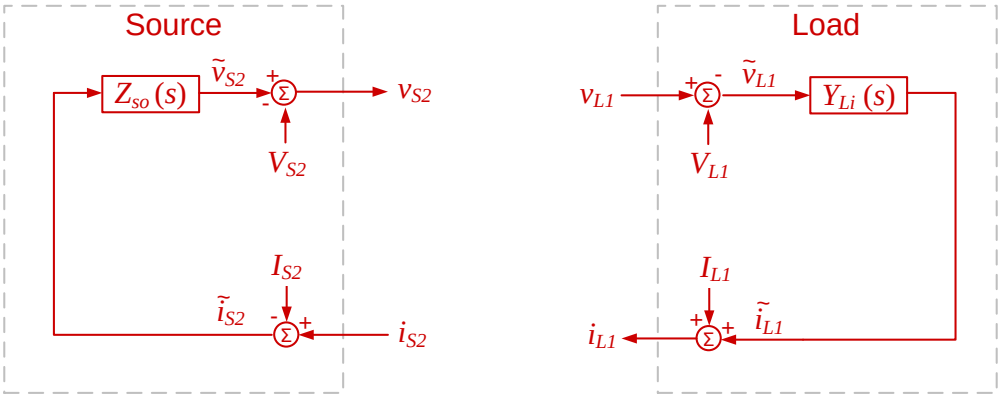

Figure 6.20: Linear dynamic model of the source and the load

6.2.3. Generic Hybrid Model of the Source and Load

Finally, by combining the non-linear static and linear dynamic model described above, the hybrid model is developed and shown in the Figure 6.21. Again, idea is that

non-linear static model provides the dynamic model with information about the operating point.

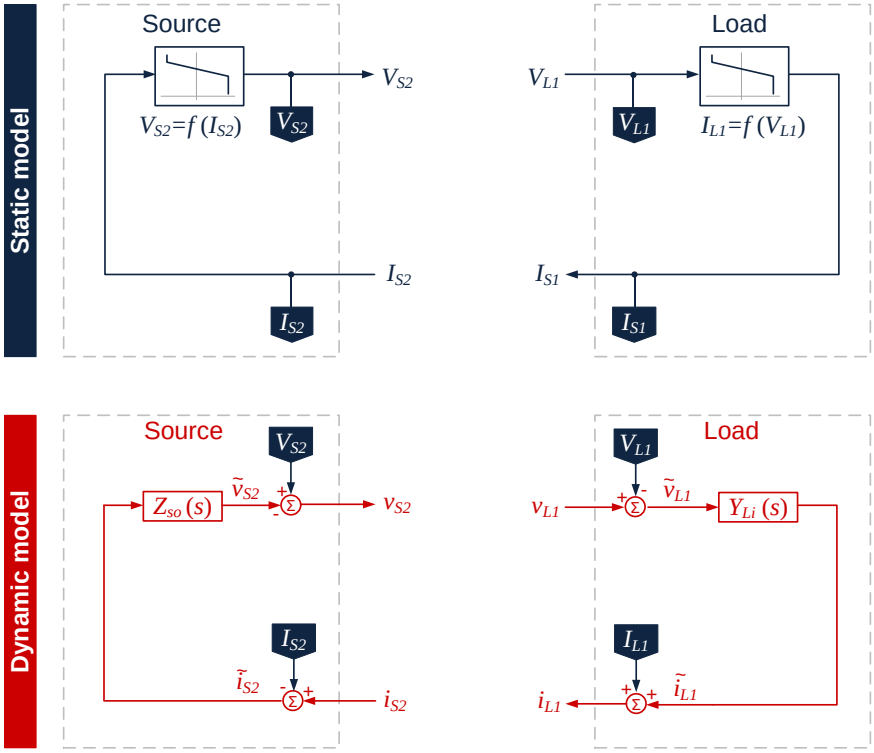

Figure 6.21: Generic hybrid model of the source and load

6.3. Verification of Hybrid Models in the System Level Simulation

The minimum relevant system comprised of the grid interface converter, solar converter and two load converters shown in the Figure 6.22 will be used for verification purpose. Hybrid terminal behavioral models will be used to represent components from that system, and the results will be compared with an average model shown in the 6.23.

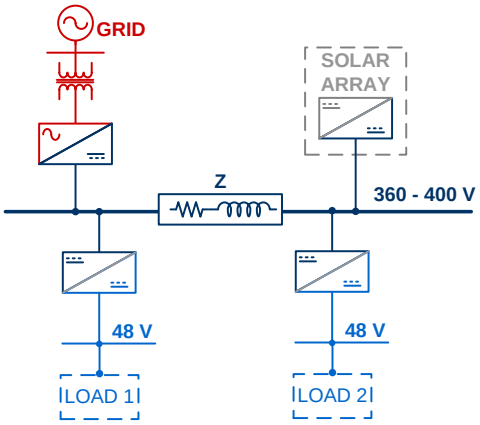

Figure 6.22: Minimum relevant nanogrid system structure

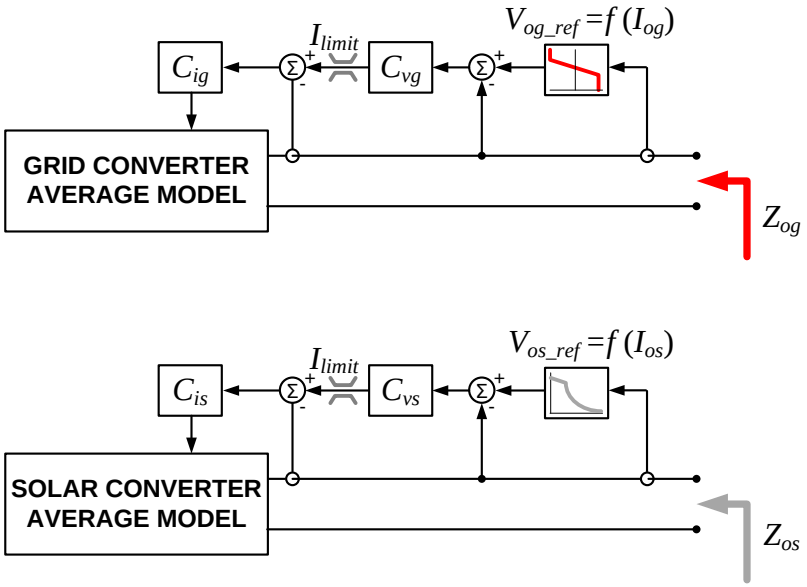

Figure 6.23: Grid interface and solar converter used in the verification procedure of the hybrid terminal behavioral model

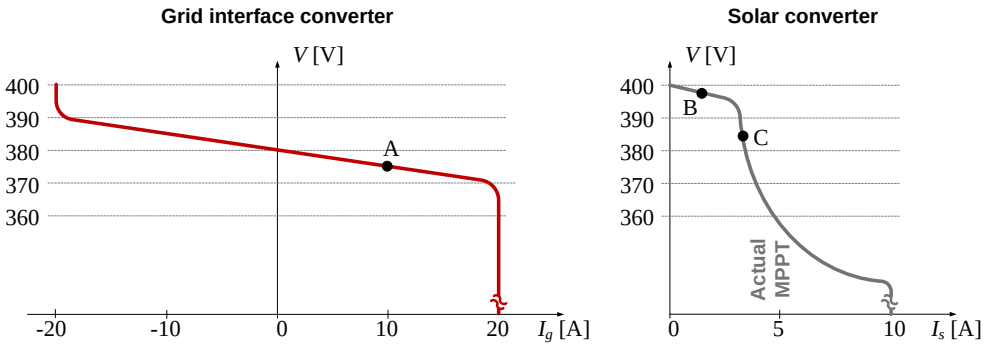

Figure 6.24: V-I characteristics of two nanogrid sources

Output impedances were obtained at the operating point “A” for the grid interface converter, and in the points “B” and “C” for the solar converter as shown in the Figure 6.24. These output impedances are shown in the Figure 6.25.

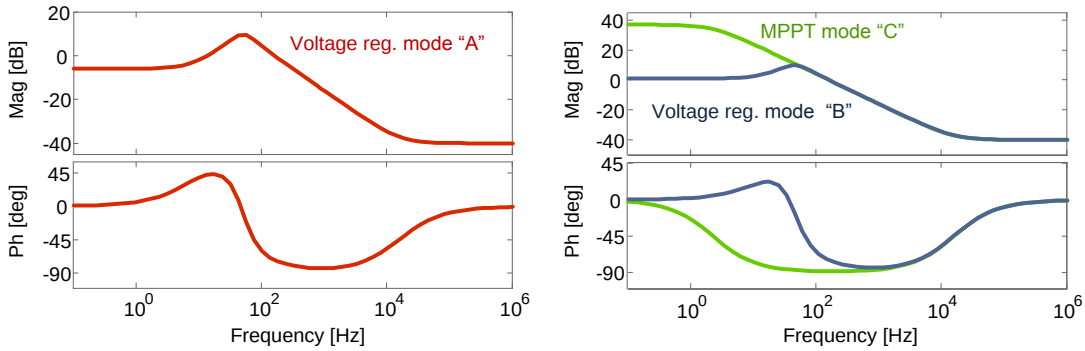

a) b)

Figure 6.25: Output impedances of the a) grid interface converter, b) solar converter

The difference in the output impedances obtained in “B” and “C” point is obvious and expected. The MPPT mode of the solar converter is actually current regulation mode featuring high output impedance at the 0Hz (dc gain) what is clearly seen in the Figure 6.25 b. Hybrid terminal behavioral model however can only use one transfer function for each of the system sources, and assuming that solar converter majority of time works in the MPPT mode, chosen is transfer function obtained in the point “C”.

The first verification is done for the grid interface converter which static V-I characteristic is known (Figure 6.24) and the parameters for the dynamic model obtained from the measured output impedance as shown in the Figure 6.25a. The load step was imposed and dynamics captured for both average and hybrid model are compared and shown in the Figure 6.26.

As seen, pretty good matching of the average and hybrid model transient response was achieved. This is the case for all large signal transients that happen within the line with the constant droop slope in the V-I characteristic shown in the Figure 6.24.

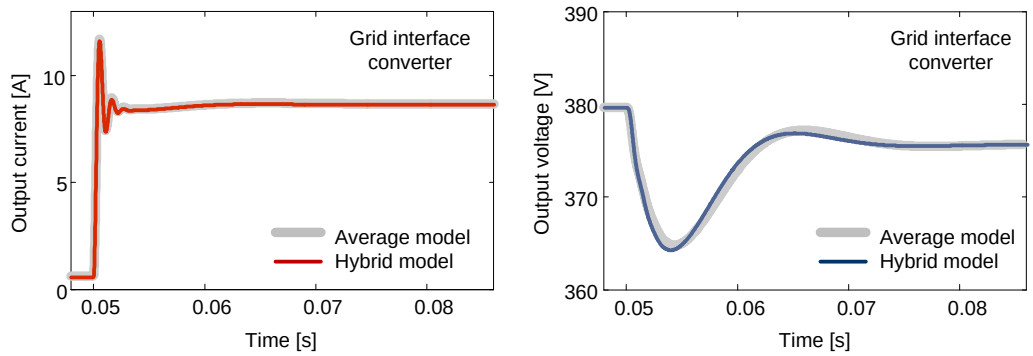

Figure 6.26: Transient response of the grid interface converter hybrid model and its comparison with average model

When large signal transient forces the mode of operation change, situation is different. For example, Figure 6.27 shows the case when load step leads the grid interface converter into the current limit. Statically model absolutely matches, while dynamically is very different. Hybrid model fails to track the dynamics of the current limit since it still works with the dynamics modeled for the voltage regulation mode (point "A" in the Figure 6.24). The attempt to model this is challenging and as mentioned, has been left as a future work.

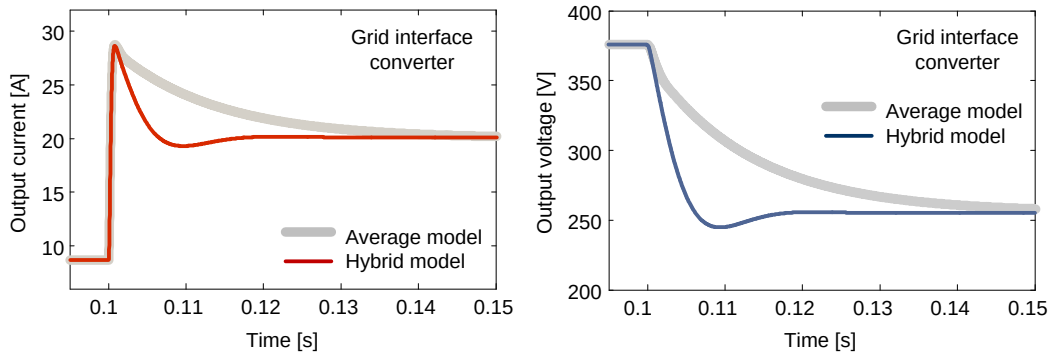

Figure 6.27: Transient response comparison when grid interface converter was forced to the current limit

The same verification procedure performed on the grid interface converter modeling was done for the solar converter model as well.

This converter is mostly working in the MPPT mode and the dynamics is modeled according to the output impedance measured in the operating point "C" as shown in the Figure 6.24. The load step was imposed and dynamics captured for both average and hybrid model are compared and shown in the Figure 6.28.

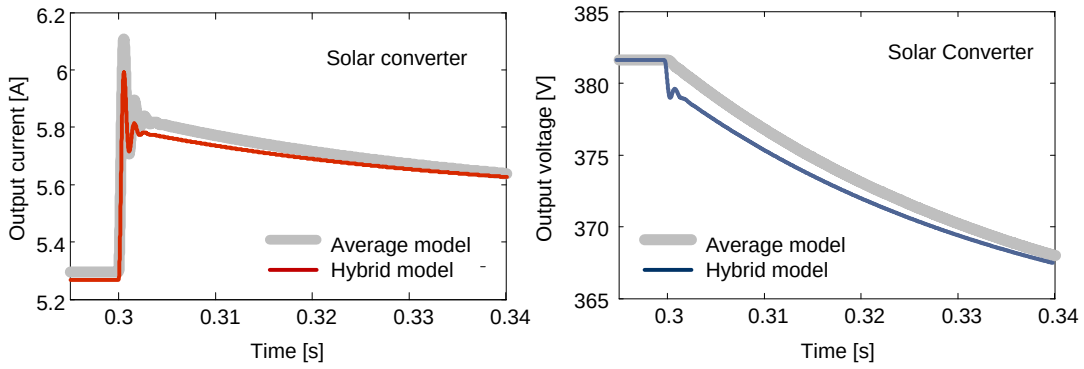

Figure 6.28: Transient response of the solar converter hybrid modeland its comparison with average model

Load step imposed was moving an operating point within the MPPT mode, and not perfect matching is observed because the output impedance is not a linear function in the MPPT mode as it is in the voltage regulation mode with the constant droop slope (Figure 6.24). However, the transient is probably acceptable for some of the system level analysis. Another issue is large signal transient that drastically changes mode of operation. The Figure 6.29 compares dynamic of the average and hybrid model for high load to low load change that suddenly brings solar converter back to the voltage regulation mode.

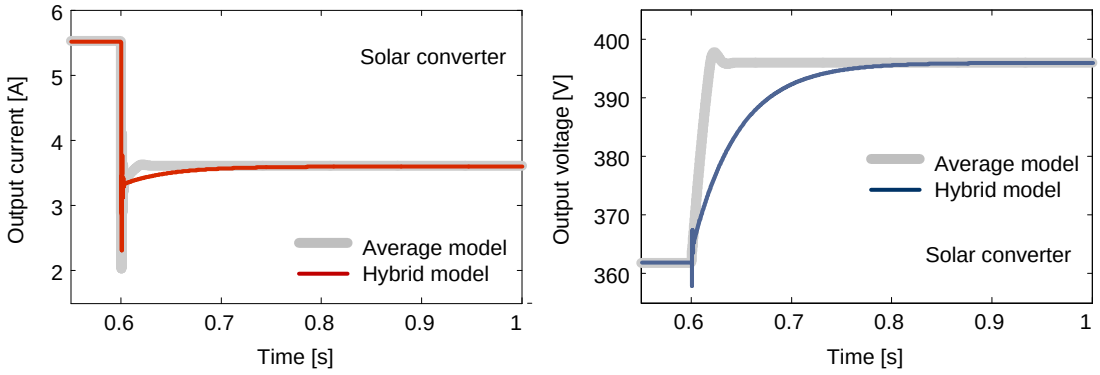

Figure 6.29: Transient responses of the solar converter when load significantly decreases

Finally, an attempt to model the sample system from Figure 6.22 can be performed. L-R impedance is added between the two source-load systems so they can interact. Figure 6.30 shows the sample or minimal relevant system presented with hybrid two-port network terminal behavioral models used above. Bus converters are modeled as open loop converters for the simpler analysis.

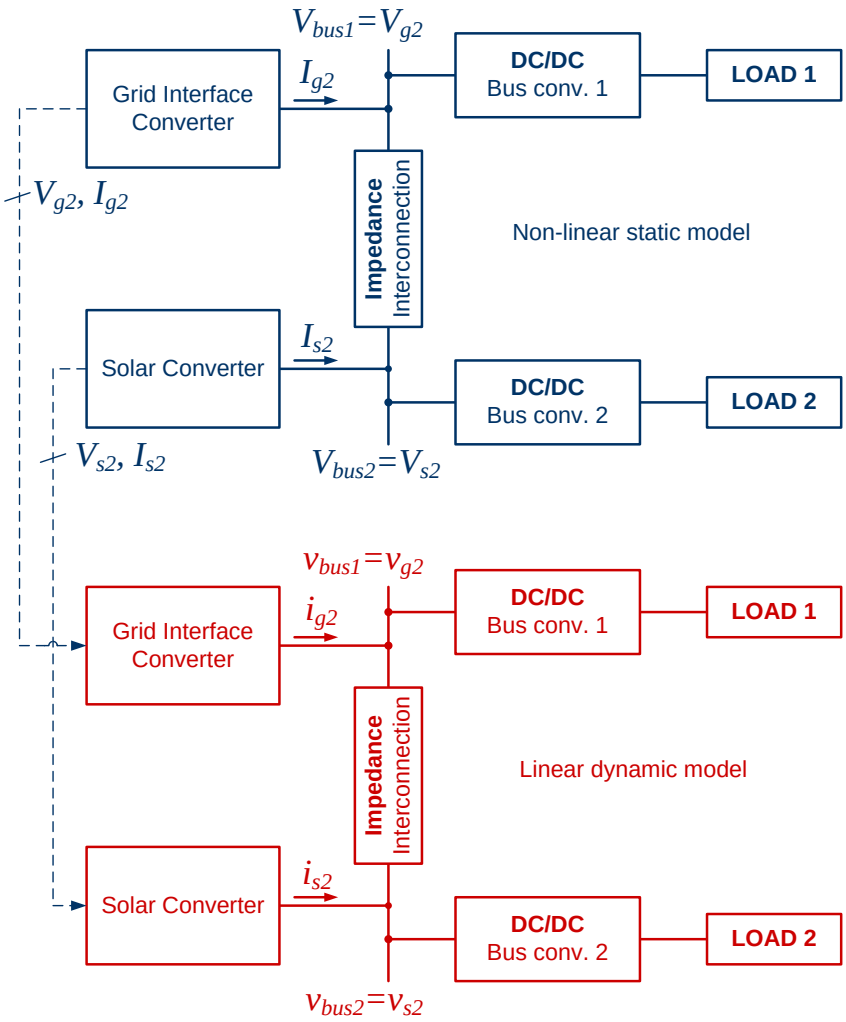

Figure 6.30: Sample system hybrid model used in simulation

It can be seen that static non-linear model was instantaneously updating the operating point values of the dynamic model, while the load was changing in steps. The results are shown in the Figure 6.31.

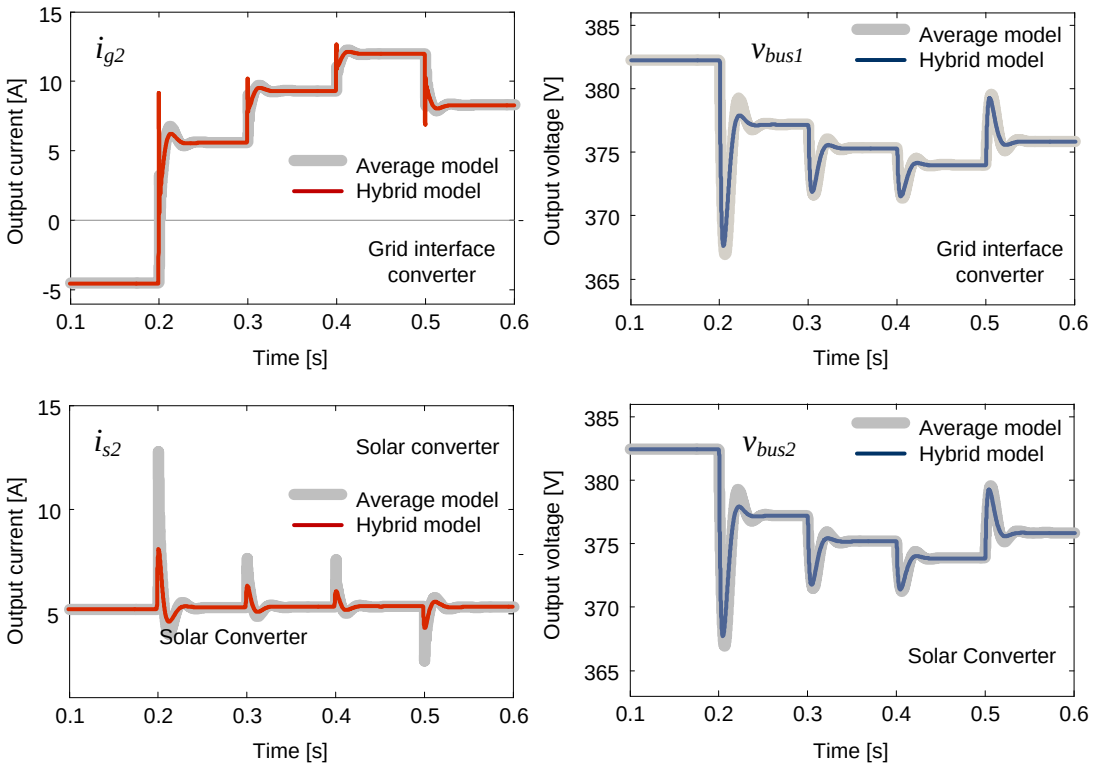

Figure 6.31: Simulation results of the sample system shown in the Figure 6.30.

It can be seen in the figure above that grid interface converter output current significantly changes when load step is applied, while solar converter output current just slightly changes. This is due to the fact that solar converter has very high output impedance in the MPPT mode (Figure 6.24) and for the wide output voltage range an output current changes are very small. The grid interface converter output current graph shows operation in the second quadrant of the V-I plane (Figure 6.24) when it actually delivers energy back to the utility grid.

Modeling approach of the source converters that combines non-linear statics and linear dynamics based on the Hammerstein approach have been shown and verified with the average models. Models nicely represent dynamics within one mode of operation where the behavior is more linear, while failed to handle mode of operation change caused by the large signal transients. Future work will be more focused on addressing these issues.

Chapter 7. CONCLUSIONS AND FUTURE WORK

The thesis' objectives are dc-nanogrid system concept and operation of the future, sustainable home. As shown, dc-nanogrid is an electrical system backbone of the power electronics - based contemporary homes envisioned to be energy sustainable and powered by different types of renewable energy sources, together with utility grid.

Although dc systems for residential applications are not mature enough, and standards have still been under development, this thesis offers conceptual, engineering-based approach as a possible solution to address this topic.

As seen in the previous chapters, dc-nanogrid system was first presented, supported with the static, predefined operation schemes. After that, some analysis over the average models has been performed emphasizing some of the important aspects and issues. However, thesis has a goal to address the "black-box", or terminal behavioral modeling approach of the system that is dynamically and statically unknown to engineers. These linear terminal behavioral models satisfactorily identify the behavior of the linear or "mildly" non-linear systems around an operating point, but fail when highly non-linear systems are concerned. Thus, in addition, thesis addresses the hybrid, non-linear behavioral modeling as a possible way to represent dynamic of such systems, assuming non-linear static, but linear dynamic behavior.

Future work will be focused on deeper understanding and comprehensive analysis of the dc-nanogrid systems in a sense of design, dynamic/static characteristics, stability and protection on the one side, and on the other - modeling approach that could offer a "black-box" system level identification procedure when a very little is known about the system that feature some degree of non-linearity.

APPENDIX. MATLAB CODES USED FOR IDENTIFICATION IN THE FREQUENCY DOMAIN

Identification of the frequency response characteristics obtained from the Network Analyzer 4395A (Agilent) is done in Matlab. Codes shown below assumes that these characteristics are captured and saved in the *.txt format somewhere on the PC before the identification process can start.

The frequency response characteristics are then loaded (imported) one by one into the Matlab's workspace by assigning them names as follows:

Audio-Susceptibility (gain) = = gg
Audio-Susceptibility (phase) = = pg
Output Impedance (gain) = = gz
Output Impedance (phase) = = pz
Input Admittance (gain) = = gy
Input Admittance (phase) = = py
Back-current Gain (gain) = = gh
Back-current Gain (phase) = = ph
Transconductance (gain) = = gtg
Transconductance (phase) = = ptg
Transresistance (gain) = = gtr
Transresistance (phase) = = ptr

The first code shown below can now be run.

```
%----------------------The first code converts *.txt to frequency-response data models
------------------------- %
%--------- START
wo=2*pi*f; % --- Frequency rad/sec
i = sqrt(-1);

% --- G merasured
Ag=gg;          % Magnitude in dB
phidg=pg;      % angle in deg
rog=(10.^(Ag./20));
phig=pi.*phidg./180;
qg = rog.*exp(i*(phig));    %Create a complex variable (magnitude and phase)

% --- Z measured
Az=gz;          % Magnitude in dB
phidz=pz;      % angle in deg
```

```
roz=(10.^(Az./20));
phiz=pi.*phidz./180;
qz = roz.*exp(i*(phiz)); %Create a complex variable (magnitude and phase

% --- Y measured
Ay=gy;          % Magnitude in dB
phidy=py;      % angle in deg
roy=(10.^(Ay./20));
phiy=pi.*phidy./180;
qy = roy.*exp(i*(phiy)); %Create a complex variable (magnitude and phase)

% --- H measured
Ah=gh;          % Magnitude in dB
phidh=ph;      % angle in deg
roh=(10.^(Ah./20));
phih=pi.*phidh./180;
qh = roh.*exp(i*(phih)); %Create a complex variable (magnitude and phase)

% --- Tg measured
Atg=gtg;          % Magnitude in dB
phidtg=ptg;      % angle in deg
rotg=(10.^(Atg./20));
phitg=pi.*phidtg./180;
qtg = rotg.*exp(i*(phitg)); %Create a complex variable (magnitude and phase)

% --- Tr mereno
Atr=gtr;          % Magnitude in dB
phidtr=ptr;      % angle in deg
rotr=(10.^(Atr./20));
phitr=pi.*phidtr./180;
qtr = rotr.*exp(i*(phitr)); %Create a complex variable (magnitude and phase)

% ------ Creating FRFs
GoM=frd(qg,wo);
ZoM=frd(qz,wo);
YiM=frd(qy,wo);
HiM=frd(qh,wo);
TgM=frd(qtg,wo);
TrM=frd(qtr,wo);
%---------END
```

The second short code will be decoupling source/load impedance/admittance from the measured frequency responces (matrix 5.25 in the thesis)

```
%----------------------The second code decouples system responses from the source and load ------------- %
%--------- START
TT=[1 0 -TgM 0; 0 1 0 TgM; TrM 0 -1 0; 0 TrM 0 1];
Tmeas=[GoM; YiM; ZoM; HiM];
solut=TT\Tmeas;
Gom=solut(1);
Yim=solut(2);
Zom=solut(3);
Him=solut(4);
Tgm=TgM;
Trm=TrM;
%--------- END
```

The final, third code will be performing curve fitting in frequency domain. Three different function are used for this purpose (pem, invfreqs and fitfrd [85]). Resultes are tuned in a few iterations until desired matching is achieved compared with the measured curves.

```
%----------------------The third code is frequency domain identification ------------- %
%--------- START

% --- G:
[mmg,ppg,ww]=bode(Gom);

[resg,freg]=frdata(Gom);

Frg=idfrd(Gom,wo,0);
Sfrg=spafdr(Frg,100);

SSg=pem(Sfrg,6,'Foc','Stability');          % HERE tune for G
fprintf('H_red:')
H1g=tf(SSg);
Hg=H1g(1:1)

[nyyg,dyyg]=invfreqs(resg(:),wo,6,6);      % HERE tune for G
fprintf('H_purple:')
Hbg=tf(nyyg,dyyg)
[magbg,phbg,wbg]=bode(Hbg);

jfg=fitfrd(Gom,6);                                % HERE tune for G
Hjg=tf(jfg);
```

```
[magjg,phjg,wjg]=bode(Hjg);

%bode(Hg)
[magg,phg,wg]=bode(Hg);

figure(11)

subplot(2,1,1);semilogx(wo,mmg(:),'k','linewidth',5);
hold on;subplot(2,1,1);semilogx(wg,magg(:),'r','linewidth',2);
hold on;subplot(2,1,1);semilogx(wbg,magbg(:),'m','linewidth',2);
hold on;subplot(2,1,1);semilogx(wjg,magjg(:),'g','linewidth',2);
ylabel('Magnitude');grid on;title(' G ')
subplot(2,1,2);semilogx(wo,ppg(:),'k','linewidth',5);hold
on;subplot(2,1,2);semilogx(wg,(phg(:)),'r','linewidth',2);
hold on;subplot(2,1,2);semilogx(wbg,phbg(:),'m','linewidth',2);
hold on;subplot(2,1,2);semilogx(wjg,phjg(:),'g','linewidth',2);
ylabel('Phase (deg)');xlabel('Frequency [rad/sec]');grid on;
%------------------------------------------------------------------------


% --- Z:
[mmz,ppz,ww]=bode(Zom);

[resz,frez]=frdata(Zom);

Frz=idfrd(Zom,wo,0);
Sfrz=spafdr(Frz,100);

SSz=pem(Sfrz,6,'Foc','Stability');          % HERE tune for Z
fprintf('H_red:')
H1z=tf(SSz)
Hz=H1z(1:1)

[nyyz,dyyz]=invfreqs(resz(:),wo,6,6);      % HERE tune for Z
fprintf('H_purple:')
Hbz=tf(nyyz,dyyz)
[magbz,phbz,wbz]=bode(Hbz);

jfz=fitfrd(Zom,6);                                % HERE tune for Z
Hjz=tf(jfz);
[magjz,phjz,wjz]=bode(Hjz);

%bode(Hz)
[magz,phz,wz]=bode(Hz);
```

```
figure(12);

subplot(2,1,1);semilogx(wo,mmz(:),'k','linewidth',5);hold
on;subplot(2,1,1);semilogx(wz,magz(:),'r','linewidth',2);
hold on; subplot(2,1,1);semilogx(wbz,magbz(:),'m','linewidth',2);
hold on; subplot(2,1,1);semilogx(wjz,magjz(:),'g','linewidth',2);
ylabel('Magnitude');grid on;title(' Z ')
subplot(2,1,2);semilogx(wo,ppz(:),'k','linewidth',5);hold
on;subplot(2,1,2);semilogx(wz,(phz(:)),'r','linewidth',2);
hold on; subplot(2,1,2);semilogx(wbz,phbz(:),'m','linewidth',2);
hold on; subplot(2,1,2);semilogx(wjz,phjz(:),'g','linewidth',2);
ylabel('Phase (deg)');xlabel('Frequency [rad/sec]');grid on;
%-----------------------------------------------------------------------


% --- Y:
[mmy,ppy,ww]=bode(Yim);

[resy,frey]=frdata(Yim);

Fry=idfrd(Yim,wo,0);
Sfry=spafdr(Fry,100);

SSy=pem(Sfry,4,'Foc','Stability');          % HERE tune for Y
fprintf('H_red:')
H1y=tf(SSy);
Hy=H1y(1:1)

[nyyy,dyyy]=invfreqs(resy(:),wo,4,4);      % HERE tune for Y
fprintf('H_purple:')
Hby=tf(nyyy,dyyy)
[magby,phby,wby]=bode(Hby);

jfy=fitfrd(Yim,4);                                % HERE tune for Y
Hjy=tf(jfy);
[magjy,phjy,wjy]=bode(Hjy);

%bode(Hy)
[magy,phy,wy]=bode(Hy);

figure(13)
```

```
subplot(2,1,1);semilogx(wo,mmy(:),'k','linewidth',5);hold
on;subplot(2,1,1);semilogx(wy,magy(:),'r','linewidth',2);
hold on;subplot(2,1,1);semilogx(wby,magby(:),'m','linewidth',2);
hold on;subplot(2,1,1);semilogx(wjy,magjy(:),'g','linewidth',2);
ylabel('Magnitude');grid on;title(' Y ')
subplot(2,1,2);semilogx(wo,ppy(:),'k','linewidth',5);hold
on;subplot(2,1,2);semilogx(wy,(phy(:)),'r','linewidth',2);
hold on;subplot(2,1,2);semilogx(wby,phby(:),'m','linewidth',2);
hold on;subplot(2,1,2);semilogx(wjy,phjy(:),'g','linewidth',2);
ylabel('Phase (deg)');xlabel('Frequency [rad/sec]');grid on;
%----------------------------------------------------------------------


% --- H:
[mmh,pph,ww]=bode(Him);

[resh,freh]=frdata(Him);

Frh=idfrd(Him,wo,0);
Sfrh=spafdr(Frh,100);

SSh=pem(Sfrh,8,'Foc','Stability');          % HERE tune for H
fprintf('H_red:')
H1h=tf(SSh);
Hh=H1h(1:1)

[nyyh,dyyh]=invfreqs(resh(:),wo,8,8);      % HERE tune for H
fprintf('H_purple:')
Hbh=tf(nyyh,dyyh)
[magbh,phbh,wbh]=bode(Hbh);

jfh=fitfrd(Him,8);                                % HERE tune for H
Hjh=tf(jfh);
[magjh,phjh,wjh]=bode(Hjh);

%bode(Hh)
[magh,phh,wh]=bode(Hh);

figure(14)

subplot(2,1,1);semilogx(wo,mmh(:),'k','linewidth',5);hold
on;subplot(2,1,1);semilogx(wh,magh(:),'r','linewidth',2);
hold on;subplot(2,1,1);semilogx(wbh,magbh(:),'m','linewidth',2);
hold on;subplot(2,1,1);semilogx(wjh,magjh(:),'g','linewidth',2);
```

```
ylabel('Magnitude');grid on;title(' H ')
subplot(2,1,2);semilogx(wo,pph(:),'k','linewidth',5);hold
on;subplot(2,1,2);semilogx(wh,(phh(:)),'r','linewidth',2);
hold on;subplot(2,1,2);semilogx(wbh,phbh(:),'m','linewidth',2);
hold on;subplot(2,1,2);semilogx(wjh,phjh(:),'g','linewidth',2);
ylabel('Phase (deg)');xlabel('Frequency [rad/sec]');grid on;
%------------------------------------------------------------------------


% --- Tg:
[mmtg,pptg,ww]=bode(Tgm);

[restg,fretg]=frdata(Tgm);

Frtg=idfrd(Tgm,wo,0);
Sfrtg=spafdr(Frtg,100);

SStg=pem(Sfrtg,6,'Foc','Stability');          % HERE tune for Tg
fprintf('H_red:')
H1tg=tf(SStg);
Htg=H1tg(1:1)

[nyytg,dyytg]=invfreqs(restg(:),wo,6,6);    % HERE tune for Tg
fprintf('H_purple:')
Hbtg=tf(nyytg,dyytg)
[magbtg,phbtg,wbtg]=bode(Hbtg);

jftg=fitfrd(Tgm,6);                                % HERE tune for Tg
Hjtg=tf(jftg);
[magjtg,phjtg,wjtg]=bode(Hjtg);

%bode(Hzs)
[magtg,phtg,wtg]=bode(Htg);

figure(17)

subplot(2,1,1);semilogx(wo,mmtg(:),'k','linewidth',5);hold
on;subplot(2,1,1);semilogx(wtg,magtg(:),'r','linewidth',2);
hold on;subplot(2,1,1);semilogx(wbtg,magbtg(:),'m','linewidth',2);
hold on;subplot(2,1,1);semilogx(wjtg,magjtg(:),'g','linewidth',2);
ylabel('Magnitude');grid on;title(' Tg ')
subplot(2,1,2);semilogx(wo,pptg(:),'k','linewidth',5);hold
on;subplot(2,1,2);semilogx(wtg,(phtg(:)),'r','linewidth',2);
hold on;subplot(2,1,2);semilogx(wbtg,phbtg(:),'m','linewidth',2);
```

```
hold on;subplot(2,1,2);semilogx(wjtg,phjtg(:),'g','linewidth',2);
ylabel('Phase (deg)');xlabel('Frequency [rad/sec]');grid on;
%------------------------------------------------------------------------


% --- Tr:
[mmtr,pptr,ww]=bode(Trm);

[restr,fretr]=frdata(Trm);

Frtr=idfrd(Trm,wo,0);
Sfrtr=spafdr(Frtr,100);

SStr=pem(Sfrtr,6,'Foc','Stability');          % HERE tune for Tr
fprintf('H_red:')
H1tr=tf(SStr);
Htr=H1tr(1:1)

[nyytr,dyytr]=invfreqs(restr(:),wo,6,6);    % HERE tune for Tr
fprintf('H_purple:')
Hbtr=tf(nyytr,dyytr)
[magbtr,phbtr,wbtr]=bode(Hbtr);

jftr=fitfrd(Trm,6);                                % HERE tune for Tr
Hjtr=tf(jftr);
[magjtr,phjtr,wjtr]=bode(Hjtr);

%bode(Htr)
[magtr,phtr,wtr]=bode(Htr);


figure(18)

subplot(2,1,1);semilogx(wo,mmtr(:),'k','linewidth',5);hold
on;subplot(2,1,1);semilogx(wtr,magtr(:),'r','linewidth',2);
hold on;subplot(2,1,1);semilogx(wbtr,magbtr(:),'m','linewidth',2);
hold on;subplot(2,1,1);semilogx(wjtr,magjtr(:),'g','linewidth',2);
ylabel('Magnitude');grid on;title(' Tr ')
subplot(2,1,2);semilogx(wo,pptr(:),'k','linewidth',5);hold
on;subplot(2,1,2);semilogx(wtr,(phtr(:)),'r','linewidth',2);
hold on;subplot(2,1,2);semilogx(wbtr,phbtr(:),'m','linewidth',2);
hold on;subplot(2,1,2);semilogx(wjtr,phjtr(:),'g','linewidth',2);
ylabel('Phase (deg)');xlabel('Frequency [rad/sec]');grid on;
%------------------------------------------------------------------------
```

```
Go=Hg; %---------- Here choose transfer function that fits the best
Zo=Hjz; %---------- Here choose transfer function that fits the best
Yi=Hjy; %---------- Here choose transfer function that fits the best
Hi=Hjh; %---------- Here choose transfer function that fits the best
Tg=Hjtg; %---------- Here choose transfer function that fits the best
Tr=Hjtr; %---------- Here choose transfer function that fits the best

figure(19);hsvd(Go);title('G');    %------ Here check Hankel singular values and stable/unstable states
figure(20);hsvd(Zo);title('Z');    %------ Here check Hankel singular values and stable/unstable states
figure(21);hsvd(Yi);title('Y');    %------ Here check Hankel singular values and stable/unstable states
figure(22);hsvd(Hi);title('H');    %------ Here check Hankel singular values and stable/unstable states
figure(25);hsvd(Tg);title('Tg');    %------ Here check Hankel singular values and stable/unstable states
figure(26);hsvd(Tr);title('Tr');    %------ Here check Hankel singular values and stable/unstable states
```

REFERENCES

[1] K. Eriksson, “Operational experience of HVDC Light™,” *Seventh International Conference on AC and DC Transmission*, pp. 205-210, Nov. 2001.

[2] S. D. Wright, A. L. Rogers, J. F. Manwell, and A. Ellis, “Transmission options for offshore wind farms in the United States,” *Proc. AWEA Annual Conference*, Portland, OR, Jun. 2002.

[3] B. R. Andersen, “HVDC transmission - opportunities and challenges,” *8th IEE International Conf. on AC and DC Power Transmission (ACDC 2006)*, pp. 24-29, Mar. 2006.

[4] R. H. Lasseter and P. Paigi, "Microgrid: a conceptual solution," in *Power Electronics Specialists Conference, 2004. PESC 04. 2004 IEEE 35th Annual*, 2004, pp. 4285-4290 Vol.6.

[5] L. Xuan and S. Bin, "Microgrids - an integration of renewable energy technologies," in *Electricity Distribution, 2008. CICED 2008. China International Conference on*, 2008, pp. 1-7.

[6] Z. M. Salameh and A. J. Davis, "Case study of a residential-scale hybrid renewable energy power system in an urban setting," in *Power Engineering Society General Meeting, 2003, IEEE*, 2003, p. 2322 Vol. 4.

[7] I. Cvetkovic, T. Thacker, D. Dong, G. Francis, V. Podosinov, D. Boroyevich, F. Wang, R. Burgos, G. Skutt, and J. Lesko, "Future home uninterruptible renewable energy system with vehicle-to-grid technology," in *Energy Conversion Congress and Exposition, 2009. ECCE 2009. IEEE*, 2009, pp. 2675-2681.

[8] D. Boroyevich, I. Cvetkovic, Dong Dong, R. Burgos, Fei Wang, Fred Lee, “Future Electronic Powers Distribution Systems – A Contemplative view,” presented at the OPTIM Conference, Brasov, Romania, May 2010.

[9] T. G. Wilson Sr., “The evolution of power electronics,” *IEEE Trans. Power Elec.*, vol. 15, no. 3, pp. 439-446, May 2000.

[10] *Electricity Technology Roadmap, 2003*. Palo Alto, CA: Electric Power Research Institute (EPRI), Inc. Link: http://mydocs.epri.com/docs/CorporateDocuments/StrategicVision/Roadmap2003.pdf.

[11] H. Akagi, “Large Static Converters for Industry and Utility Applications,” *Proc. of the IEEE*, vol. 89, no. 6, pp. 976-983, Jun. 2001.

[12] H. Akagi, “Active harmonic filters,” *Proc. of the IEEE*, vol. 93, no. 12, pp. 2128-2141, Dec. 2005.

[13] F. Blaabjerg, Z. Chen, and S. B. Kjaer, “Power electronics as efficient interface in dispersed power generation systems,” *IEEE Trans. Power Electron.*, vol. 19, no. 5, pp. 1184-1194, Sep. 2004.

[14] A. Yazdani and R. Iravani, “A neutral-point clamped converter system for direct-drive variable-speed wind power unit,” *IEEE Trans. on Energy Conv.*, vol. 21, no. 2, pp. 596-607, Jun. 2006.

[15] R. Strzelecki, G. Benysek (editors), *Power electronics in smart electrical energy networks*, London: Springer-Verlag Ltd., 2008.

[16] N. Osifchin, “A telecommunications buildings: power infrastructure in a new era of public networking,” *IEEE INTELEC 2000*, pp. 1-7.

[17] A. Emadi, Y. J. Lee, K. Rajashekara, “Power electronics and motor drives in electric, hybrid electric, and plug-in hybrid electric vehicles,” *IEEE Trans. Industrial Electron.*, vol. 55, no. 6, pp. 2237-2245, Sep. 2008.

[18] J. A. Rosero, J. A. Ortega, E. Aldabas, and L. Romeral, “Moving towards a more electric aircraft,” *IEEE Aerosp. Electron. Syst. Mag.*, vol. 22, no. 3, pp. 3–9, Mar. 2007.

[19] T. Ericsen, Y. Khersonsky, and P. K. Steimer, “PEBB concept applications in high power electronics converters,” *Proc. IEEE PESC*, pp. 2284- 2289, Sep. 2005.

[20] T. J. McCoy and J. V. Amy, “The state-of-the-art of integrated electric power and propulsion systems and technologies on ships,” *Proc. IEEE ESTS*, pp. 340-344, Apr. 2009.

[21] D. Salomonsson and A. Sannino, "Low-Voltage DC Distribution System for Commercial Power Systems With Sensitive Electronic Loads," *Power Delivery, IEEE Transactions on,* vol. 22, pp. 1620-1627, 2007.

[22] J.Jonnes, “*Empires of Light: Edison, Tesla, Westinghouse and the Race to Electrify the World”*. New York: Random House 2003.

[23] T.Gruzs and J.Hall,”Ac, dc or hybrid power solution for today’s telecommunication facilities,”in Proc. IEEE INTELEC, Phoenix, AZ, Sep. 10-14, 2000, pp. 361-368.

[24] C.Chan,”An overview of electric vehicle technology,” Proc. IEEE, vol.81, no.9, pp. 1202-1213, Sep.993.

[25] J. G. Ciezki and R. W. Ashton, “Selection and stability issues associated with a navy shipboard DC zonal electric distribution system,” *IEEE Trans. on Pow. Del.,* vol.15, no. 2, pp. 665-669, Apr. 2000.

[26] Z. Weidong, S. Pekarek, J. Jatskevich, O. Wasynczuk, D. Delisle, “A model-in-the-loop interface to emulate source dynamics in a zonal DC distribution system,” *IEEE Trans. on Pow. Elec.*, vol. 20, no. 2, pp. 438-445, Mar. 2000.

[27] R.Hill, “Electric Railway Traction. Part 3. Traction Power Supplies,” *Power Eng. J.*, vol 8, pp. 275-286, Dec. 1994.

[28] K. Eriksson, “Operational experience of HVDC Light™,” *Seventh International Conference on AC and DC Transmission,* pp. 205-210, Nov. 2001.

[29] S. D. Wright, A. L. Rogers, J. F. Manwell, and A. Ellis, “Transmission options for offshore wind farms in the United States,” *Proc. AWEA Annual Conference,* Portland, OR, Jun. 2002.

[30] B. R. Andersen, “HVDC transmission - opportunities and challenges,” *8th IEE International Conf. on AC and DC Power Transmission (ACDC 2006),* pp. 24-29, Mar. 2006.

[31] D. Salomonsson and A. Sannino, "Low-Voltage DC Distribution System for Commercial Power Systems With Sensitive Electronic Loads," *Power Delivery, IEEE Transactions on,* vol. 22, pp. 1620-1627, 2007.

[32] D. Nilsson and A. Sannino, "Efficiency analysis of low- and medium- voltage DC distribution systems," in *Power Engineering Society General Meeting, 2004. IEEE*, 2004, pp. 2315-2321 Vol.2.

[33] P. Karlsson and J. Svensson, "DC bus voltage control for a distributed power system," *Power Electronics, IEEE Transactions on*, vol. 18, pp. 1405-1412, 2003.

[34] H. Kakigano, Y. Miura, T. Ise, and R. Uchida, "DC Micro-grid for Super High Quality Distribution - System Configuration and Control of Distributed Generations and Energy Storage Devices," in *Power Electronics Specialists Conference, 2006. PESC '06. 37th IEEE*, 2006, pp. 1-7.

[35] G. C. Hua, W. A. Tabisz, C. S. Leu, N. Dai, R. Watson, and F. C. Lee, "Development of a DC distributed power system," in *Applied Power Electronics Conference and Exposition, 1994. APEC '94. Conference Proceedings 1994., Ninth Annual*, 1994, pp. 763-769 vol.2.

[36] M. Brenna, G. C. Lazaroiu, and E. Tironi, "High power quality and DG integrated low voltage dc distribution system," in *Power Engineering Society General Meeting, 2006. IEEE*, 2006, p. 6 pp.

[37] W. Schulz, "ETSI standards and guides for efficient powering of telecommunication and datacom," in *Telecommunications Energy Conference, 2007. INTELEC 2007. 29th International*, 2007, pp. 168-173.

[38] T. Aoki, M. Yamasaki, T. Takeda, T. Tanaka, H. Harada, and K. Nakamura, "Guidelines for power-supply systems for datacom equipment in NTT," in *Telecommunications Energy Conference, 2002. INTELEC. 24th Annual International*, 2002, pp. 134-139.

[39] Y. Liu, A. Pratt, P. Kumar, M. Xu, and F. C. Lee, "390V Input VRM for High Efficiency Server Power Architecture," in *Applied Power Electronics Conference, APEC 2007 - Twenty Second Annual IEEE*, 2007, pp. 1619-1624.

[40] D. Yu, Z. Xiaohu, B. Sanzhong, S. Lukic, and A. Huang, "Review of non-isolated bi-directional DC-DC converters for plug-in hybrid electric vehicle charge station application at municipal parking decks," in *Applied Power Electronics Conference and Exposition (APEC), 2010 Twenty-Fifth Annual IEEE*, 2010, pp. 1145-1151.

[41] D. Izquierdo, R. Azcona, F. del Cerro, C. Fernandez, and B. Delicado, "Electrical power distribution system (HV270DC), for application in more electric aircraft," in *Applied Power Electronics Conference and Exposition (APEC), 2010 Twenty-Fifth Annual IEEE*, 2010, pp. 1300-1305.

[42] R. D. Middlebrook, "Input filter considerations in design and application of switching regulators," *IEEE IAS '76*, pp. 366-382, 1976.

[43] X. Feng and F. C. Lee, "On-line measurement of stability margin of dc distributed power system," *IEEE APEC '00*, vol. 2, pp. 1190-1196, Mar. 2000.

[44] J. Liu, X. Feng, F. C. Lee, and D. Boroyevich, "Stability margin monitoring for dc distributed power systems via perturbation approaches," *IEEE Trans. Power Elec.*, vol. 18, no. 6, pp. 1254-1261, Nov. 2003.

[45] A. D. Graham, "Non-characteristic line harmonics of PWM ac-dc converters," *Proc. Harmonics and Quality of Power.*, vol. 3, pp. 955-960, Oct. 2000.

[46] H. Zhu, R. Burgos, F. Wang, D. Boroyevich, and D. K. Lindner, "Modeling and prediction of dc-bus harmonic resonance for ac-to-ac motor drive systems," *Conf. AIAA IECEC '06*, Jun. 2006.

[47] L. Arnedo, R. Burgos, F. Wang, and D. Boroyevich, "Black-box terminal characterization modeling of dc-to-dc converters," *IEEE APEC '07*, pp. 457-463, Feb. 2007

[48] J. A. Oliver, R. Prieto, V. Romero, and J. A. Cobos, "Behavioral modeling of dc-dc converters for large-signal simulation of distributed power systems," in *Applied Power Electronics Conference and Exposition, 2006. APEC '06. Twenty-First Annual IEEE*, 2006, p. 6 pp.

[49] V. Valdivia, A. Barrado, A. Lazaro, C. Fernandez, and P. Zumel, "Black-box modeling of DC-DC converters based on transient response analysis and parametric identification methods," in *Applied Power Electronics Conference and Exposition (APEC), 2010 Twenty-Fifth Annual IEEE*, 2010, pp. 1131-1138.

[50] A. C. Baisden, D. Boroyevich, and F. Wang, "EMI Terminal Modeling," in *Industry Applications Society Annual Meeting, 2008. IAS '08. IEEE*, 2008, pp. 1-8.

[51] Q. Liu, F. Wang, and D. Boroyevich, "Modular-terminal-behavioral (MTB) model for characterizing switching module conducted EMI generation in converter systems," *IEEE Trans. on Power Electronics*, vol. 21, no. 6, pp. 1804-1814, Nov. 2006.

[52] J. A. Oliver, R. Prieto, J. A. Cobos, O. Garcia, and P. Alou, "Hybrid Wiener-Hammerstein Structure for Grey-Box Modeling of DC-DC Converters," in *Applied Power Electronics Conference and Exposition, 2009. APEC 2009. Twenty-Fourth Annual IEEE*, 2009, pp. 280-285.

[53] B. H. Cho and F. C. Y. Lee, "Modeling and analysis of spacecraft power systems," *Power Electronics, IEEE Transactions on*, vol. 3, pp. 44-54, 1988.

[54] J. R. Lee, *et al.*, "Modeling and simulation of spacecraft power systems," *Aerospace and Electronic Systems, IEEE Transactions on*, vol. 24, pp. 295-304, 1988.

[55] P. G. Maranesi, *et al.*, "Two-part characterization of PWM voltage regulators at low frequencies," *Industrial Electronics, IEEE Transactions on*, vol. 35, pp. 444-450, 1988.

[56] R.H. Lasseter, A. Akhil, C. Marnay, J. Stephens, J. Dagle, R. Guttromson, A. Meliopoulous, R. Yinger, and J. Eto . "Integration of Distributed Energy Resources: The CERTS MicroGrid Concept," April 2002 [Online]. Available: http://certs.lbl.gov/CERTS_P_DER.html

[57] W. Kempton, J. Tomić, "Vehicle-to-Grid Power Fundamentals: Calculating Capacity and Net Revenue," *Journal of Power Sources*, vol. 144, pp. 268-279, 2005.

[58] A. N. Brooks, "Vehicle-to-grid Demonstration Project: Grid Regulation Ancillary Service with a Battery Electric Vehicle," Final report, Contract number 01-313, Prepared for the California Air Resources Board and the California Environmental Protection Agency, December, 2002.

[59] S.G. Wirasingha, N.Schofield and A. Emadi, "Plug-in hybrid electric vehicle developments in the US: Trends, barriers and economic feasibility," in *Vehicle Power and Propulsion Conference, 2008. VPPC '08. IEEE*, 2008, pp. 1-8.

[60] T. Thacker, R. Wang, D. Dong, R. Burgos and D. Boroveyich, "Phase-Locked Loops using State Variable Feedback for Single-Phase Converter Systems," in *Applied Power Electronics Conference and Exposition, 2009. APEC 2009. Twenty-Fourth Annual IEEE*, 2009, pp. 864-870.

[61] D. Dong, T. Thacker, R. Burgos, D. Boroyevich, F. Wang and B. Giewont, “Controls Design and Experimental Verification of a Multi-Function Single-Phase Bidirectional PWM Converter for Renewable Energy Systems,” presented at the CPES Conference, Blacksburg, April 2009.

[62] R. Tirumala, N. Mohan and C. Henze, “Seamless transfer of grid-connected PMW inverters between utility-interactive and stand-alone modes,” in *Applied Power Electronics Conference and Exposition, 2002. APEC 2002. Seventeenth Annual IEEE*, 2002, pp. 1081-1086 vol.2.

[63] T. Thacker, R. Burgos, F. Wang, and D. Boroyevich, "Single-phase islanding detection based on phase-locked loop stability," in *Energy Conversion Congress and Exposition, 2009. ECCE 2009. IEEE*, 2009, pp. 3371-3377.

[64] *IEEE Standard for Interconnecting Distributed Resources with Electric Power Systems*, IEEE Standard 1547-3003, pp. 0_1-16, 2003.

[65] CompactRIO system. See details at www.ni.com

[66] D. Dong, T. Thacker, R. Burgos, D. Boroyevich, and F. Wang, "On zero steady-state error of single-phase PWM inverters voltage control and phase-locked loop system," in *Energy Conversion Congress and Exposition, 2009. ECCE 2009. IEEE*, 2009, pp. 892-899.

[67] T. Sakurai, "Perspectives on power-aware electronics," in *Solid-State Circuits Conference, 2003. Digest of Technical Papers. ISSCC. 2003 IEEE International*, 2003, pp. 26-29 vol.1.

[68] Dong Dong, Ruxi Wang, Dushan Boroyevich, Igor Cvetkovic, “A Two-stage High Power Density Single-phase ac-dc Bi-directional PWM Converter for Renewable Energy System,” submitted to the ECCE 2010.

[69] J. Bryan, R. Duke and S. Round, ”Decentralised control of a nanogrid,” presented at *Australasian Universities Power Engineering Conference*, Christchurch, New Zealand, Sep., 2003.

[70] J. Bryan, R. Duke, and S. Round, “Distributed generation – nanogrid transmission and control options,” *International Power Engineering Conference*, vol. 1, pp. 341–346, Nov., 2003.

[71] J. Bryan, R. Duke, and S. Round, "Decentralized generator scheduling in a nanogrid using DC bus signaling," in *Power Engineering Society General Meeting, 2004. IEEE*, 2004, pp. 977-982 Vol.1.

[72] J. Schonberger, R. Duke, and S. D. Round, "DC-Bus Signaling: A Distributed Control Strategy for a Hybrid Renewable Nanogrid," *Industrial Electronics, IEEE Transactions on*, vol. 53, pp. 1453-1460, 2006.

[73] J. Schonberger, *et al.*, "Autonomous Load Shedding in a Nanogrid using DC Bus Signalling," in *IEEE Industrial Electronics, IECON 2006 - 32nd Annual Conference on*, 2006, pp. 5155-5160.

[74] "IEEE Recommended Practice for the Design of DC Auxiliary Power Systems for Generating Stations," *IEEE Std 946-2004 (Revision of IEEE Std 946-1992)*, pp. 0_1-32, 2005.

[75] "IEEE Guide for Batteries for Uninterruptible Power Supply Systems," *IEEE Std 1184-2006 (Revision of IEEE 1184-1994)*, pp. 0_1-63, 2006.

[76] "IEEE Recommended Practice for Grounding of Industrial and Commercial Power Systems," *IEEE Std 142-2007 (Revision of IEEE Std 142-1991)*, pp. c1-215, 2007.

[77] B. T. Irving and M. M. Jovanovic, "Analysis, design, and performance evaluation of droop current-sharing method," in Applied Power Electronics Conference and Exposition, 2000. APEC 2000. Fifteenth Annual IEEE, 2000, pp. 235-241 vol.1.

[78] L. Arnedo, *et al.*, "Black-Box Terminal Characterization Models for the Analysis and Simulation of Distributed Power Electronic Systems," in *Power Electronics Specialists Conference, 2007. PESC 2007. IEEE*, 2007, pp. 1968-1973.

[79] L. Arnedo, *et al.*, "Un-terminated frequency response measurements and model order reduction for black-box terminal characterization models," in *Applied Power Electronics Conference and Exposition, 2008. APEC 2008. Twenty-Third Annual IEEE*, 2008, pp. 1054-1060.

[80] L. Arnedo, *et al.*, "System-Level Black-Box Dc-to-Dc Converter Models," in *Applied Power Electronics Conference and Exposition, 2009. APEC 2009. Twenty-Fourth Annual IEEE*, 2009, pp. 1476-1481.

[81] G. C. Verghese and V. J. Thottuvelil, "Aliasing effects in PWM power converters," in Proc. IEEE PESC'99, 1999, pp. 1043-1049.

[82] www.vicr.com

[83] C. Kenney and G. Hewer, "Necessary and sufficient conditions for balancing unstable systems," *Automatic Control, IEEE Transactions on*, vol. 32, pp. 157-160, 1987.

[84] P. Kokotovic and P. Sannuti, "Singular perturbation method for reducing the model order in optimal control design," *Automatic Control, IEEE Transactions on*, vol. 13, pp. 377-384, 1968.

[85] www.mathworks.com

[86] F. Alonge, F. D'Ippolito, F. M. Raimondi, and S. Tumminaro, "Nonlinear Modeling of DC/DC Converters Using the Hammerstein's Approach," *Power Electronics, IEEE Transactions on*, vol. 22, pp. 1210-1221, 2007.